

**Picosecond Optical Modulation of Vanadium Dioxide  
Incorporated into Silicon Photonics**

By

Kent Anson Hallman

Dissertation

Submitted to the Faculty of the  
Graduate School of Vanderbilt University  
in partial fulfillment of the requirements

for the degree of

DOCTOR OF PHILOSOPHY

in

Physics

15 December 2018

Nashville, Tennessee

Approved:

Richard F. Haglund, Jr., Ph.D.

Bridget R. Rogers, Ph.D.

Norman H. Tolk, Ph.D.

Kalman Varga, Ph.D.

Sharon M. Weiss, Ph.D.

*To Judah,*

*May angels carry you to your destination*

*and laugh as you inevitably make fun of this dedication*

## ACKNOWLEDGEMENTS

I would like to begin by thanking my family; their encouragement has been vital to my ability to write this dissertation. I thank my mother for the moral support she provided and my sister, Rebekah, for asking about my day and then distracting me by telling me about her own. In addition to their support, I owe a great debt of gratitude to my father and Deb as well as my sister Erica and her family (Aaron, Autumn, and Alexa) for sharing their homes when I misplaced mine. Their generosity was a boon to me. I also thank those whose friendships allowed me to escape from Vanderbilt now and then: JB, Laura, Bryson, Austin, Will, and numerous others.

I would like to thank all the people I have worked with throughout my graduate career. The mentorship of Judson Ryckman, Bob Marvel, and Jed Ziegler was invaluable in the first few years of research and I am grateful to Sergey Avanesyan for sharing his knowledge of lasers. In addition, I would like to that I thank Sami Halimi, Christina McGahan, Sam White, Petr Markov, Claire Marvinney, Rod Davidson, and especially Kevin Miller because it is always a welcome relief to have someone beside you in the fog that is research. I appreciate the patience of those high school students and undergraduates who allowed me to attempt to lead them through that same fog, including Yujie Cai, Grant Steelman, Michael Saavedra, Grant Varnau, Vamsi Subraveti, Joshua Robinson, and especially Alexander Link. For discussions providing a fresh view on old topics or just some distraction, I thank David Curie, Jason Bonacum, Daniel Mayo, Francis Afzal, Chanse Hungerford, Hiram Conley, and Zhihua Zhu. I would also like to thank the VINSE staff, both past and present, for all their help; the efforts of Kurt Heinrich, Anthony Hmelo, Alice Leech,

Dmitry Koktysh, Bo Choi, and Ben Schmidt were crucial to the success of the films and devices used in this dissertation. I am also grateful to the staff of the Vanderbilt Physics and Astronomy Department, including Don Pickert, Peggy McGowan, Libby Johnson, and Barbara Amann, for always being willing to help.

Finally, I would like to express my gratitude to my Ph.D. committee, Professors Bridget Rogers, Norman Tolk, Kalman Varga, Sharon Weiss, and Richard Haglund for challenging me to be a better scientist and make sure my work made an impact. A special thanks is due to Professor Weiss, who has been a pleasure to work with on two different grants. But without my advisor, Professor Richard Haglund, this would never have been possible; because of his guidance and patience that I was able to perform this work and compose this dissertation. Aside from the grammar lessons I should have learned much earlier in life, he has taught me a great deal about compassion.

*This dissertation is a result of work funded partly by the United States National Science Foundation (ECCS-1509740), the Air Force Office of Scientific Research (FA9550-10-1-0366), and the Vanderbilt Institute of Nanoscale Science and Engineering. I would also like to thank the McMinn Endowment for my fellowship.*

## TABLE OF CONTENTS

	Page
DEDICATION .....	ii
ACKNOWLEDGEMENTS .....	iii
LIST OF TABLES .....	viii
LIST OF FIGURES .....	ix
Chapter	
1. INTRODUCTION .....	1
1.1. Optical Modulators .....	1
1.2. Vanadium Dioxide.....	3
2. EXPERIMENTAL TOOLS AND TECHNIQUES .....	10
2.1. Introduction.....	10
2.2. Characterization Techniques .....	10
2.2.1. Atomic Force Microscopy .....	10
2.2.2. Scanning Electron Microscopy .....	10
2.2.3. Confocal Raman Spectroscopy .....	11
2.2.4. Ultrafast Pulse Generation and Wavelength Conversion.....	11
2.3. Fabrication Techniques.....	13
2.3.1. Pulsed Laser Deposition .....	13
2.3.2. Radio-Frequency Magnetron Sputtering.....	14
2.3.3. Electron-Beam Lithography.....	14
2.3.4. Reactive-Ion Etching .....	15
3. DESCRIPTION OF VO <sub>2</sub> PHASES BY DENSITY FUNCTIONAL THEORY .....	16
3.1. Introduction.....	16
3.2. History of Theoretical Descriptions of VO <sub>2</sub> .....	16

3.3. Details of the Density Functional Theory Calculations.....	18
3.4. Computation Results.....	20
3.5. Discussion and Impact of Results.....	29
4. NANOSCALE HOLOGRAPHIC IMAGING OF VANADIUM DIOXIDE THIN FILMS WITH X-RAYS .....	33
4.1. Introduction.....	33
4.2. Overview of X-Ray Holography .....	34
4.3. Sample Fabrication and Characterization.....	36
4.4. X-Ray Absorption Spectroscopy and Band Diagram of the VO <sub>2</sub> Film.....	38
4.5. Comparison of Electron Microscopy and X-Ray Holography .....	41
4.6. Spectroscopic X-Ray Holographic Response and Local Phase Determination.....	42
4.7. The Potential for Similar Measurements with Femtosecond Resolution .....	47
5. NANOSECOND MODULATION OF VO <sub>2</sub> -ON-SILICON HYBRID DEVICES .....	49
5.1. Introduction.....	49
5.2. Fabrication and Description of VO <sub>2</sub> -On-Silicon Hybrid Devices .....	49
5.3. Nanosecond All-Optical Modulation Setup Description.....	52
5.4. Nanosecond Characterization of All-Optical Absorption Modulator.....	54
5.5. Nanosecond Characterization of All-Optical Phase Modulator .....	56
5.6. All-Optical Phase Modulation After Femtosecond Excitation.....	62
6. ULTRAFAST MODULATION OF EMBEDDED VO <sub>2</sub> -SILICON HYBRID WAVEGUIDE DEVICES .....	71
6.1. Introduction.....	71
6.2. Description of Embedded VO <sub>2</sub> -Silicon Hybrid Devices .....	73
6.2.1. Design and Simulations .....	73
6.2.2. Device Fabrication .....	74
6.2.3. Static Characterization .....	76
6.3. Ultrafast Response of Embedded VO <sub>2</sub> -Silicon Hybrid Devices.....	82
6.3.1. Out-of-Plane Pump, In-Waveguide Probe Configuration.....	82
6.3.2. Femtosecond Excitation of the Embedded-VO <sub>2</sub> Waveguide Device .....	87

7. CONCLUSIONS .....	98
7.1.1. Summary and Contributions .....	98
7.1.2. Outlook and Future Work .....	100
APPENDICES .....	103
A. Alignment Procedure for Out-Of-Plane, In-Waveguide Pump-Probe Optical Setup .....	103
B. Labview Program for Out-Of-Plane, In-Waveguide Pump-Probe Optical Setup...	123
BIBLIOGRAPHY .....	127

## LIST OF TABLES

Table	Page
3.1 Crystal structures parameters for various VO <sub>2</sub> phases predicted with density functional theory and compared to values from literature .....	22
3.2 Magnetic ground state and band gap energy predicted by density functional theory calculations with a tuned hybrid functional compared with experimental observations and the results of other theoretical approaches.....	26
6.1 Threshold absorbed energy densities from literature compared to femtosecond excitation of VO <sub>2</sub> -embedded devices .....	93

## LIST OF FIGURES

Figure	Page
1.1 Ultrafast dynamics and geometry of a graphene-based all-optical modulator ...	2
1.2 Attempts to incorporate graphene into CMOS-compatible all-optical modulators.....	3
1.3 Crystal structures for the R and M1 phases of VO <sub>2</sub> .....	4
1.4 Conductivity change across the phase transition for a VO <sub>2</sub> single crystal .....	5
1.5 Change in optical constants over the phase transition for a VO <sub>2</sub> thin film.....	5
1.6 Phase diagram for aluminum-doped VO <sub>2</sub> and a generic phase diagram for doped VO <sub>2</sub> .....	7
1.7 Ultrafast phase diagram for the photo-induced phase transition of VO <sub>2</sub> .....	8
1.8 Ultrafast electron diffraction and ultrafast infrared transmissivity measurements demonstrating the existence of a monoclinic metallic phase at low fluences .....	9
2.1 Schematic representation of the process of optical parametric amplification ..	13
3.1 Crystal structures for various VO <sub>2</sub> phases predicted with density functional theory .....	20
3.2 Simulated density of states for the M1 and R phases compared to experimental photoelectron spectra .....	23
3.3 Three possible antiferromagnetic configurations for the M2 phase .....	28
4.1 Experimental configuration for x-ray holography experiment from Eisebitt <i>et al</i> and measured hologram .....	34
4.2 Raman spectrum of the VO <sub>2</sub> film used for x-ray holography experiments .....	36

4.3	Temperature-dependent transmission of the VO <sub>2</sub> film used for x-ray holography experiments.....	37
4.4	Band structure schematic of M1 and R phases of VO <sub>2</sub> along with x-ray transmission spectra.....	39
4.5	A scanning electron micrograph compared to reconstructed x-ray holographic images taken at three different temperatures.....	42
4.6	Spectrally resolved images at the vanadium and oxygen edges.....	43
4.7	Estimation of the fraction of each phase across the transition for a single VO <sub>2</sub> grain using by defining spectroscopic thresholds and areal integration.....	45
5.1	Schematics and scanning electron micrographs for silicon-VO <sub>2</sub> hybrid absorption modulators and phase modulator waveguide devices.....	50
5.2	Schematic of optical experiment used to measure nanosecond modulation of silicon-VO <sub>2</sub> hybrid waveguide devices.....	52
5.3	Measured time-response of absorption modulators.....	53
5.4	Effect of pump fluence on modulation contrast and relaxation time for both absorption and phase modulator devices after nanosecond excitation.....	55
5.5	Device spectrum and temporal response as a function of pump fluence for a phase modulator device at the resonant wavelength.....	56
5.6	Time-dependent spectra of a hybrid silicon-VO <sub>2</sub> device compared to a silicon-only control device.....	57
5.7	Relationship of the phase modulation to resonance shift for ring resonator devices of different radii.....	59
5.8	Diagram of out-of-plane pump, in-waveguide cw-probe optical setup.....	63
5.9	Scanning electron micrographs of ring resonator device measured and signal extraction scheme for out-of-plane pump, in-waveguide cw-probe setup.....	64

5.10	Time-dependent spectra for the VO <sub>2</sub> -Si ring resonator and a similar control device .....	65
5.11	Device response as a function of fluence for the VO <sub>2</sub> -silicon ring resonator and a similar control device .....	67
5.12	Anomalous spectral feature of the VO <sub>2</sub> -silicon ring resonator and a similar control device below threshold fluence compared to the expected result found above the threshold fluence .....	68
6.1	Schematic and simulations of VO <sub>2</sub> embedded into a silicon waveguide .....	72
6.2	Scanning electron micrographs of the devices including integrated gold heaters. Insets show a silicon-only reference waveguide and an embedded-VO <sub>2</sub> devices both before and after VO <sub>2</sub> deposition .....	76
6.3	Characterizations of the VO <sub>2</sub> -embedded silicon waveguides including tilted scanning electron micrographs, atomic force microscopy, and temperature-dependent transmission of a witness film .....	77
6.4	Temperature-dependent transmission of the VO <sub>2</sub> -embedded devices measured by passing current through the integrated gold heaters .....	78
6.5	Experimental transmission, insertion loss, and modulation depth compared to simulations based on partial filling of the VO <sub>2</sub> trenches .....	80
6.6	Comparison of modulation depth for VO <sub>2</sub> -on-waveguide devices and VO <sub>2</sub> -embedded devices for different patch lengths .....	81
6.7	Out-of-plane pump, in-waveguide probe optical setup .....	83
6.8	Signal and idler spectra .....	86
6.9	Time-response of VO <sub>2</sub> -embedded devices at a variety of fluences .....	88
6.10	Time-response of VO <sub>2</sub> -embedded devices with a smaller delay stage acceleration .....	89

6.11	Fluence-dependence of VO <sub>2</sub> -embedded device transmission.....	95
6.12	Effect of time-zero position when with pump fluence.....	97
A.1	Out-of-plane pump, in-waveguide probe optical setup diagram with label for every optic to aid in alignment description.....	105
B.1	Front Panel for the Labview program used to run the pump-probe setup .....	124
B.2	Left half of the Block Diagram for the Labview program used to run the pump-probe setup .....	125
B.3	Right half of the Block Diagram for the Labview program used to run the pump-probe setup.....	126

# CHAPTER 1

## INTRODUCTION

### 1.1. Optical Modulators

Light signals have been used to transmit information for centuries, but it was not until the 1980s that photons were used to transport massive amounts of data through optical fibers. The advantages of optical fibers over conventional metal wires include increased bandwidth and decreased signal losses. However, there is still a major disadvantage of optical fibers: cost. Despite the lower price of the raw material, glass rather than copper, the complex manufacturing process makes optical fibers cost significantly more than copper wire. According to Gauss's law and the Drude model for good conductors, electrical signals carried by copper wires are limited to propagating near the surface of the metal, but optical signals can be transmitted in the bulk of multi-core fibers [1]. Combined with the ability to encode separate streams of data into a single core using separate optical wavelengths, called wavelength-division multiplexing, optical fibers can easily make up the cost difference, on a per bit basis. However, as more information is packed into a single fiber, the ability to separate the different optical channels to be sent to individual users will become vital. The current method of performing this task in optical switchyards involves converting the optical signal to an electrical signal before re-emitting the data stream as a new optical signal into another fiber. This is not only slow, but it also wastes energy. All-optical modulators could enable switching streams of data with a decreased loss of energy and time [2], a crucial task as it becomes more common to transmit data in optical fibers the entire way to the consumer.

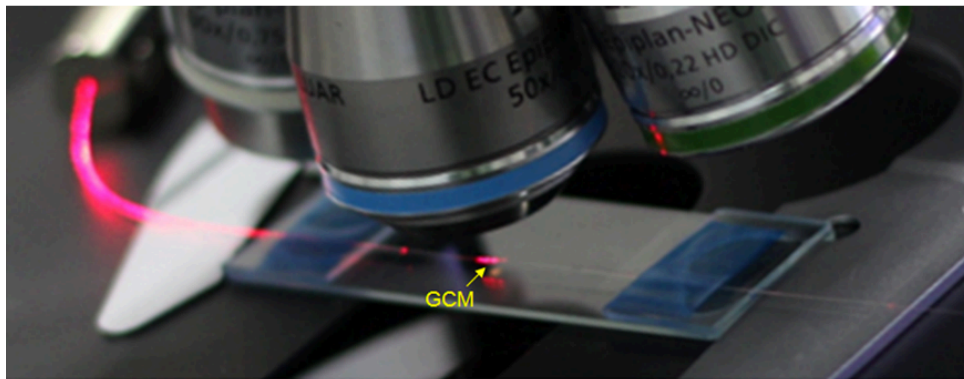
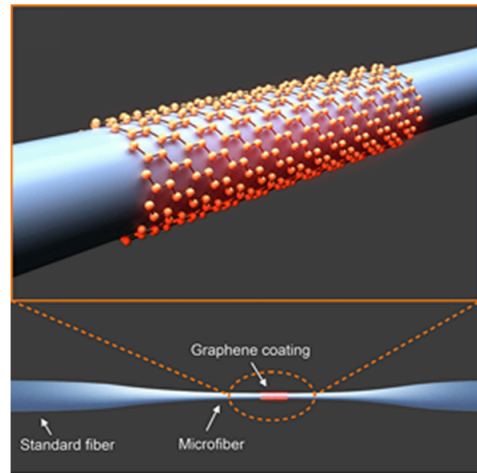
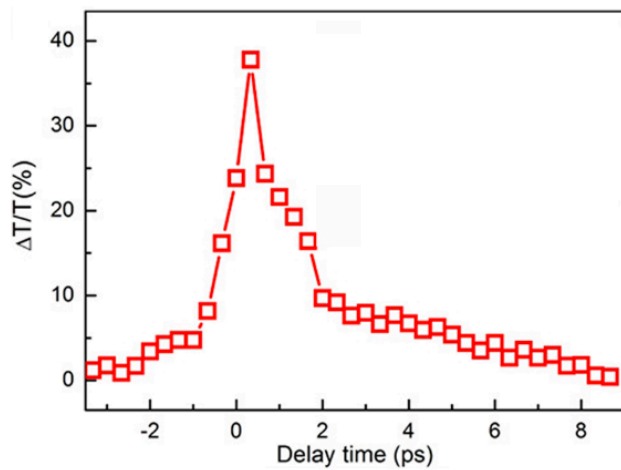


Figure 1.1. Time response of a graphene-based device, a schematic of the device, and a photograph of the device. Images adapted with permission from reference [3].

Because the nonlinear optical properties of silicon that facilitate optical switching are small, one of the most promising approaches to realizing ultrafast all-optical modulation compatible with current complementary metal-oxide semiconductor (CMOS) fabrication techniques and technologies is to incorporate a material with larger nonlinearities. Numerous such all-optical modulators have been proposed based upon materials like  $WS_2$  [4], phosphorene [5], black phosphorus [6], indium tin oxide [7], and PbS quantum dots [8]. One material in particular, graphene, has been extensively explored for all-optical modulation

[3,9–12]. In fact, a graphene-wrapped optical fiber currently holds the record for fastest switching speed in a waveguide-based all-optical modulator [3]. The device shows a switching speed of about 2 ps, but the microfiber-based design cannot be easily integrated into the current wafer-based CMOS architecture as one can see in Figure 1.1. However, the exceptional temporal response have justified attempts to integrate similar devices into wafer-based devices despite the fabrication difficulties, as seen in Figure 1.2. In the last chapter of this dissertation, similar switching speeds are observed in a CMOS-compatible device based on a phase change material, vanadium dioxide.

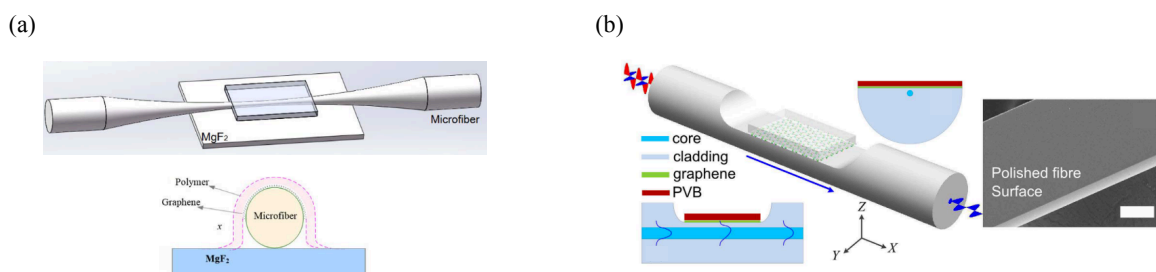


Figure 1.2. (a) Proposed graphene-based all-optical modulator on a magnesium fluoride wafer in a microfiber waveguide. (b) A device in which graphene is sandwiched between polyvinyl butyral (PVB) and a polished standard optical fiber. Images in (a) and (b) adapted with permission from references [13] and [14], respectively.

## 1.2. Vanadium Dioxide

Because of its insulator-to-metal transition, vanadium dioxide (VO<sub>2</sub>) has been studied for over a half-century and has many potential applications. The phase transition occurs at about 70°C and is associated with a transition from a monoclinic crystal structure, shown in Figure 1.3(b), to a rutile phase, Figure 1.3(a). Across the phase transition, VO<sub>2</sub> exhibits a large change in conductivity and optical constants that motivate a majority of its potential applications.

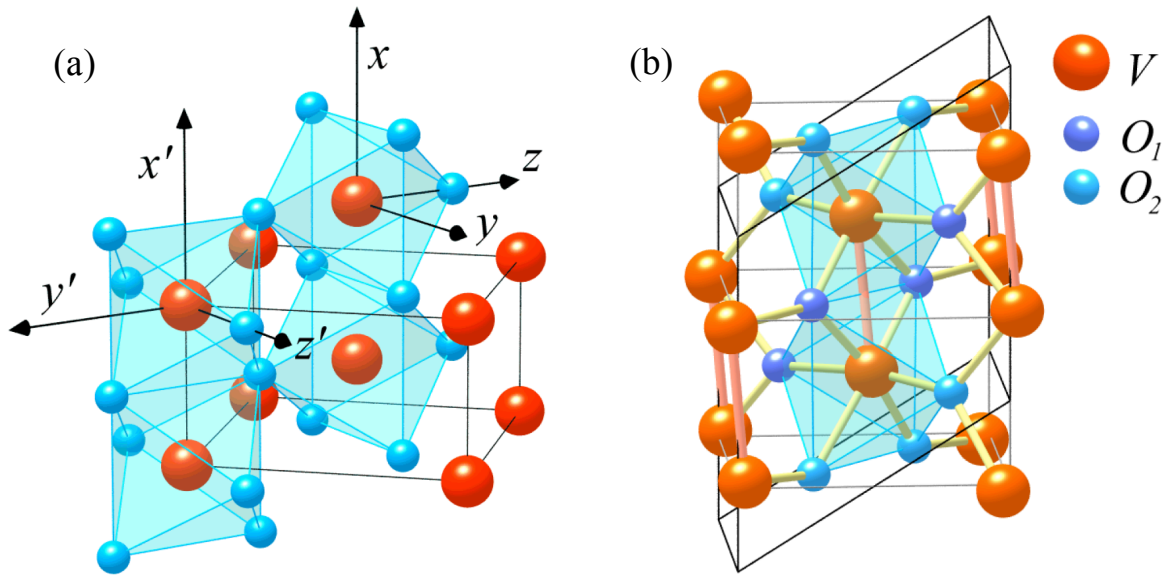


Figure 1.3. Crystal structures for (a) R and (b) M1 phases of  $\text{VO}_2$ . The larger spheres represent the metal atoms while the smaller spheres are the oxygens. Note that all oxygens are equivalent in R but not in the M1 structure reflecting the decrease in symmetry. Image adapted with permission from reference [15].

The contrast in electrical conductivity between the two phases of  $\text{VO}_2$ , like that seen in Figure 1.4 in single crystals, suggests that the material could be readily used for electrical switching and memory applications [16–19]. The large change in optical constants, shown in Figure 1.5, lends itself to applications like optical limiting [20–23], smart windows [24–28], and tunable metamaterials [29–31]. In this dissertation, incorporation of  $\text{VO}_2$  into silicon photonics enables a device capable of picosecond all-optical modulation, as discussed in Chapter 6. Such hybrid  $\text{VO}_2$ -silicon devices may pave the way for faster optical communications.

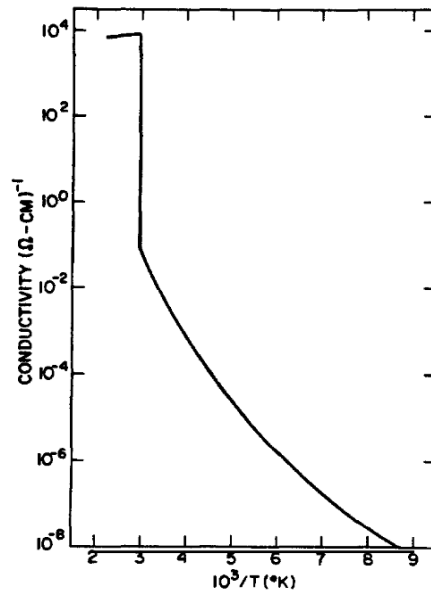


Figure 1.4. Conductivity change across the phase transition for a single crystal of  $\text{VO}_2$ . Reprinted with permission from reference [32].

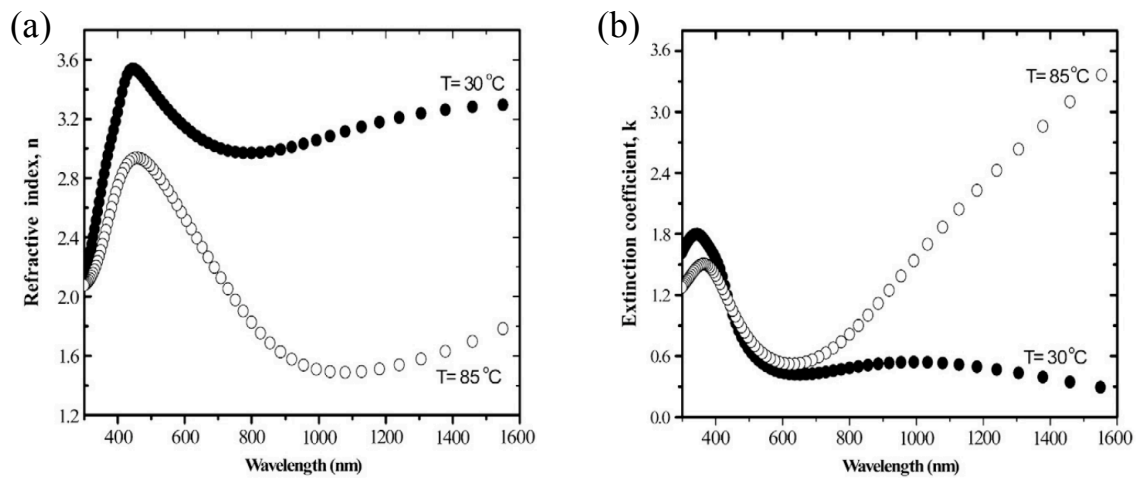


Figure 1.5. Change in optical constants across the phase transition thin film of  $\text{VO}_2$ . Image adapted with permission from reference [33].

Although the low-temperature monoclinic (M1) and the high-temperature rutile phases (R) discussed above are the most commonly discussed phases of  $\text{VO}_2$ , numerous other

phases have been observed. Figure 1.6(a) contains a phase diagram illustrating the effect of doping VO<sub>2</sub> single crystals with aluminum. At the left of the phase diagram, the M1-to-R phase transition is seen at about 70°C as expected for undoped VO<sub>2</sub>. When vanadium atoms are replaced by aluminum atoms, two other insulating phases, M2 and T, can be stabilized. The M2 is another monoclinic phase, while the T phase is triclinic. Figure 1.6(b) contains a more general phase diagram for the two different doping regimes. Doping with other trivalent ions, like chromium, iron, or gallium yields results similar to aluminum: two additional insulating phases, M2 and T, and a minor increase in the transition temperature. In contrast, doping VO<sub>2</sub> with penta- or hexavalent ions, as seen on the left of Figure 1.6(b), drastically decreases the transition temperature without creating new phases.

The three insets to Figure 1.6(b) represent the crystallographic differences between the three insulating phases more clearly than most depictions by only showing the metal (mostly vanadium) atoms in blue without showing any oxygen atoms. The M1 phase consists of metal atoms that are both paired and canted from the rutile c-axis (represented by the dashed black line). In the M2 phase, half of the metallic chains of atoms are dimerized but not canted while the other half are canted but not paired. The atomic positions of the T phase are about halfway between the positions found in the M1 and M2 phases, resulting in the triclinic crystal structure that is less symmetric than the monoclinic structures.

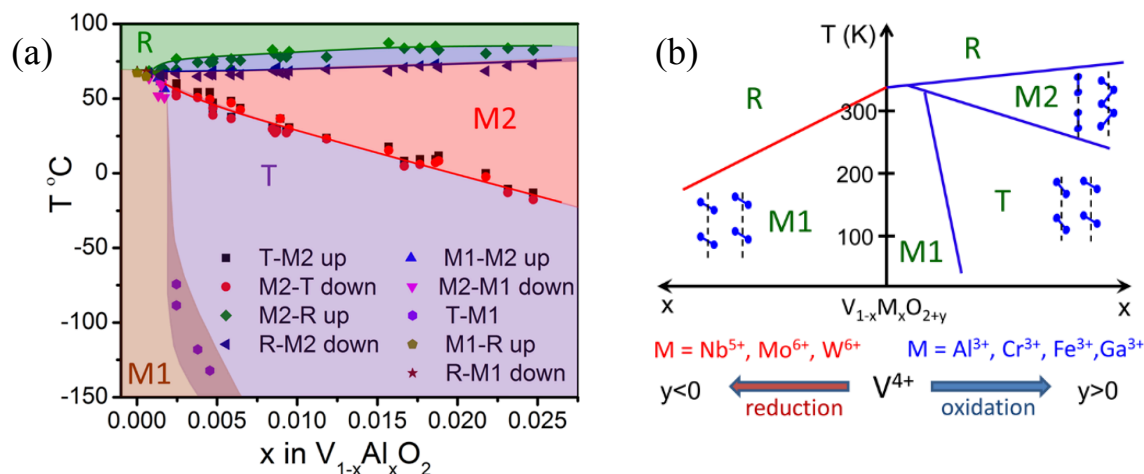


Figure 1.6. (a) Phase diagram for Al-doped single crystals of VO<sub>2</sub>. (b) Generic phase diagram for doped VO<sub>2</sub>. The insets depict simplified crystal structure for three insulating phases, each showing a pair of vanadium-atom chains and their relationship with the rutile c-axis (dashed black line). Adapted with permission from reference [34]. Copyright 2012 American Chemical Society.

In addition to the thermally-driven phase transition, VO<sub>2</sub> can be switched by laser pulses. Early experiments with nanosecond [35] and picosecond [36] pulses were unable to resolve the time required to photo-induce the phase transition of VO<sub>2</sub>. However, a more recent experiment has made it clear that the mechanism for the photo-induced phase transition from femtosecond optical pulses is athermal, since the required energy is less for the photo-induced transition than the thermally-driven transformation [37]. The combination of the heat capacity of VO<sub>2</sub> and the latent heat of the phase transition suggests an energy requirement of 2.3 eV/nm<sup>3</sup>, exceeding the energy requirement measured for a an ultrafast 800-nm pump of about 2 eV/nm<sup>3</sup> [37]. When pumped at 2000 nm instead, the energy required, about 1 eV/nm<sup>3</sup>, is even less than the latent heat alone, 1.5 eV/nm<sup>3</sup> [37].

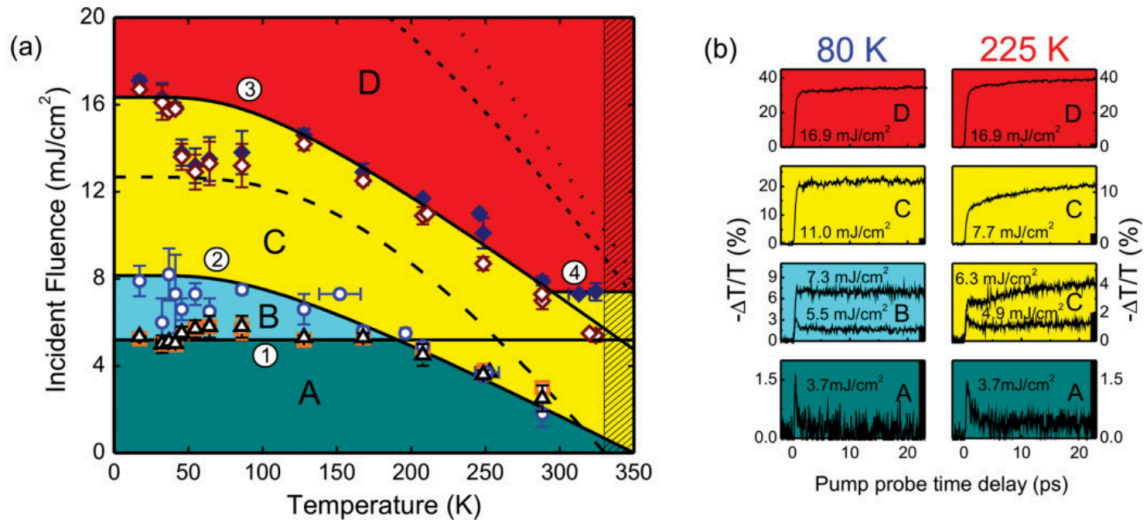


Figure 1.7. (a) Ultrafast phase diagram for the photo-induced phase transition of 130 nm thin films of  $\text{VO}_2$ . The inability of various thermal models (dotted and dashed lines) to confine the regimes of distinct dynamics suggests that simple heating from absorption is not the origin of the photo-induced phase transition. In contrast, a model based upon a critical density of 6 THz phonons and a separate critical electron density is able to define the boundaries to the dynamical regimes. (b) Time-resolved transmission of the  $\text{VO}_2$  films for a few selected fluences shows a regime with a fast off-time (bottom two panels). Reprinted with permission from reference [38].

Although the M1-to-R transition can occur in less than 100 fs [39,40], the return R-to-M1 transition is much slower, usually on the order of nanoseconds. Although this long off-time is not conducive to applications in optical modulation, consideration of the ultrafast phase diagram in Figure 1.7(a) suggests a solution. If the femtosecond laser fluence is reduced below the critical threshold to fully drive the M1-to-R transition, a transient metallization can be observed like in Figure 1.7(b) in the bottom panels.

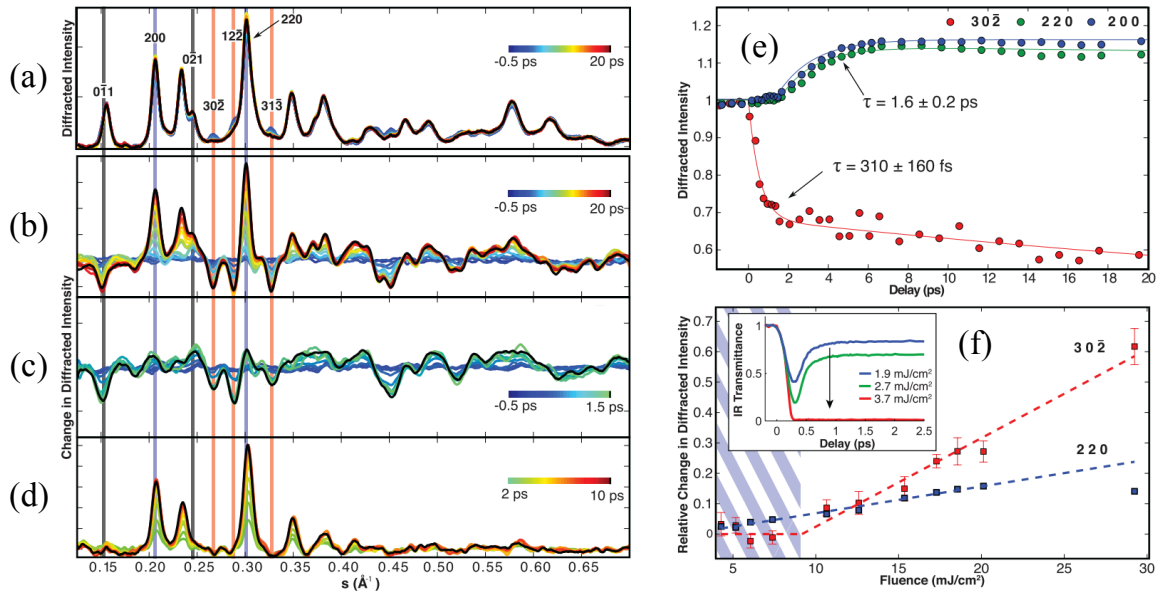


Figure 1.8. (a) Diffracted intensities of ultrafast electron beam for all time-delays show small deviations from unpumped measurement (black line) on thin film of VO<sub>2</sub>. (b) Difference between unpumped measurement and all other time delays shows a convolution of two signals: (c) short time-delays demonstrate a small adjustment in crystal structure attributed to another monoclinic phase while (d) longer time-delays yield the diffracted signal corresponding to the rutile phase. (e) Time-resolved intensities for individual diffraction peaks indicate two different decay constants. (f) Fluence-resolved measurements indicate a low-fluence regime in which the full structural transition is not completed, and the infrared transmissivity in the inset indicates the metallic nature of this transient phase. Reprinted with permission from reference [41].

The current understanding of the transient response observed in the bottom of Figure 1.7(b) is that the electronic phase transition has occurred without fully driving the structural transition, similar to observations of the thermally-driven transition [42,43]. The justification for this claim relies on ultrafast electron diffraction measurements [41] shown in Figure 1.8. This conclusion is supported by other recent measurements [44–47].

## CHAPTER 2

### EXPERIMENTAL TOOLS AND TECHNIQUES

#### 2.1. Introduction

This chapter gives an overview of the techniques used in this dissertation. An overview of these tools will help the reader to understand why each method was used and where its use fits into the fabrication recipe or protocol for device characterization. Each of the sections in this chapter can be thought of as individual building blocks of the experiments to be performed. In contrast, when the technique is developed as a part of the work, like in the case of the out-of-plane pump in-waveguide probe measurements or the x-ray holography experiments, the technique will be discussed in the relevant chapter.

#### 2.2. Characterization Techniques

##### 2.2.1. Atomic Force Microscopy

During an atomic force microscopy measurement, a cantilever with a very sharp tip is rastered across the sample. The force that the sample surface exerts on the tip is measured by detecting the laser light reflected off the back of the cantilever. The measured force corresponds to nanoscale height, so a map of the height of the sample is produced as the cantilever is moved across the sample.

##### 2.2.2. Scanning Electron Microscopy

To image the surface of a sample, an electron-beam is focused onto the sample with magnetic and electrostatic lenses. Secondary electrons, typically from  $k$ -shells of the atoms

in the sample, are emitted from the top few nanometers of the sample and detected. Atoms with higher atomic number emit more secondary electrons and the number of detected secondary electrons give the value encoded into a grayscale image called a scanning electron micrograph.

### **2.2.3. Confocal Raman Spectroscopy**

Confocal Raman spectroscopy is performed by focusing a monochromatic laser onto the surface of a sample and detecting the wavelength of the reflected light. Photons that have inelastically scattered with atoms in the sample encode information about the vibrational modes of the material by shifting the wavelength of the measured light from the original laser wavelength. Numerous material-specific vibrational modes allow for a characteristic Raman spectrum for different atomic lattices.

### **2.2.4. Ultrafast Pulse Generation and Wavelength Conversion**

Titanium-doped sapphire (Ti:sapphire) crystals are the standard laser material used to generate ultrashort pulses. However, typical Ti:sapphire oscillators produce pulses with only nanojoules of energy. When laser pulses with more energy are needed, a Ti:sapphire amplifier can be used. If the wavelength output from these laser amplifiers, about 800 nm, is unacceptable, an optical parametric amplifier can be utilized. The ultrashort pulses used in Chapters 5 and 6 of this dissertation were generated with this three-step process. Each of the three stages is outlined in more detail below.

The femtosecond laser pulses generated in a laser oscillator are generated from constructive interference of modes in a cavity containing the Ti:sapphire crystal pumped by an intense beam of green, continuous-wave (cw) light from another laser. This constructive interference is called mode-locking. The cw light is from a diode-pumped Nd:YAG laser and

provides the necessary population inversion in the crystal. As the short pulse oscillates from one end of the cavity to another, an acousto-optic or electro-optic crystal is used to select only those photons that have a phase proportional to the round-trip time in the cavity, and these are transmitted through a partial reflector and used in the experiments. Thus, the length of the cavity determines how often a pulse leaves the laser oscillator. Although the corresponding repetition rate is typically tens of MHz, any one pulse contains only nanojoules of energy.

If a larger energy per pulse is required, a laser amplifier can be used. In a laser amplifier, a small fraction of pulses from a laser oscillator, typically about one out of every 80,000, is switched out of the stream of pulses from the oscillator and amplified in another Ti:sapphire crystal to microjoules or even millijoules per pulse. This second Ti:sapphire crystal is pumped by a nanosecond Nd:YLF green laser. The pulse makes numerous passes through the crystal and this configuration is referred to as a regenerative amplifier.

If a wavelength is desired other than the 800 nm provided by a Ti:sapphire amplifier, an optical parametric amplifier (OPA) can be used. In the OPA used in Chapters 5 and 6, a nonlinear crystal, beta barium borate ( $\beta$ -BaB<sub>2</sub>O<sub>4</sub>), is used to generate near infrared signal and idler beams in a difference-frequency mixing process. The 800 nm beam from the laser amplifier is used to drive the process as seen in Figure 2.1. Although a white-light beam generated from optical rectification in an undoped sapphire plate seeds the process, the only wavelengths that will be amplified are those that satisfy the phase matching condition determined by the indices of refraction of  $\beta$ -BaB<sub>2</sub>O<sub>4</sub> at the signal and idler wavelengths:

$$(2.1) \quad \frac{n_{pump}}{\lambda_{pump}} = \frac{n_{signal}}{\lambda_{signal}} + \frac{n_{idler}}{\lambda_{idler}}$$

Since this is a nonlinear parametric process, light is not absorbed by the  $\beta$ -BaB<sub>2</sub>O<sub>4</sub>, no heat

is generated, and energy must be conserved:

$$(2.2) \quad \frac{1}{\lambda_{pump}} = \frac{1}{\lambda_{signal}} + \frac{1}{\lambda_{idler}}$$

When these two relationships are satisfied, energy will be converted from the pump beam to the signal and idler beams. In Chapters 5 and 6, the OPA is aligned so the signal beam is at 1550 nm, making the idler beam at about 1670 nm.

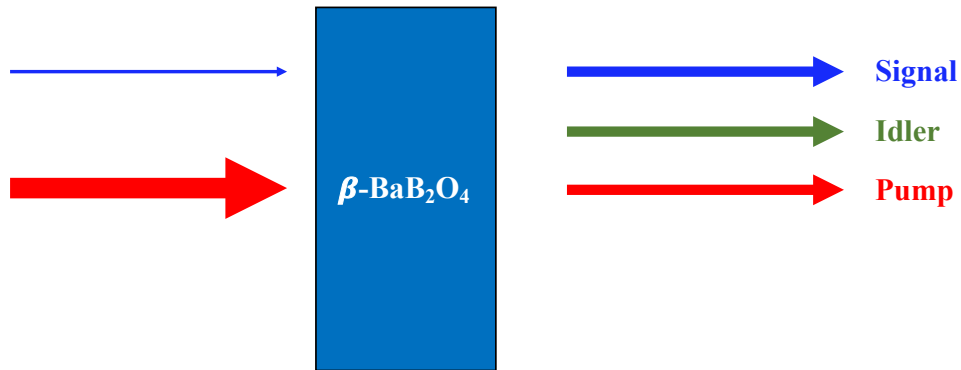


Figure 2.1. Schematic representing optical parametric amplification. From the white light, only the wavelength, represented by the thin blue line, that meets the phase-matching condition will be amplified. An idler beam will be generated according to energy conservation.

### 2.3. Fabrication Techniques

A more thorough discussion of the two  $\text{VO}_2$  deposition methods used in this dissertation can be found in reference [48], but a quick description of each is found below.

#### 2.3.1. Pulsed Laser Deposition

Pulsed laser deposition is a method for depositing thin films. An intense laser pulse is focused on a target and causes energetic species to be ejected into a vacuum chamber where substrates are placed. The ionic and atomic species deposit onto the substrates with a stoichiometry determined by the target composition and gas mixture present in the vacuum chamber. While detailed information about the  $\text{VO}_2$  deposition method can be found

elsewhere [49], small deviations from that recipe were necessary for the x-ray holography experiments due to the delicate nature of the samples (Chapter 4).

### **2.3.2. Radio-Frequency Magnetron Sputtering**

Another technique for depositing VO<sub>2</sub> films is radio-frequency (RF) magnetron sputtering. In this method, an AC potential is applied between a cathode and anode. The cathode is typically referred to as the target, as it will be at least a component of the deposited thin film. The AC potential causes an inert gas contained in the vacuum chamber to be ionized and accelerated toward the target. These energetic particles sputter material from the target and it is deposited on substrates elsewhere in the chamber. RF magnetron sputtering was used to deposit the films on all devices in Chapters 4 and 5.

### **2.3.3. Electron-Beam Lithography**

To create nano- or micro-scale devices, electron-beam lithography (EBL) was utilized. The first steps in EBL include coating the sample with a polymer resist; exposing portions of the resist to an electron beam, which breaks the polymer into smaller chemical species; and selectively removing the exposed resist using a relatively weak organic solvent. At this point, a mask of the unexposed polymer covers some of the sample and there are two methods to create nano- or micro-scale patterns from this mask. The exposed material can either be etched away leaving the inverse pattern, or a new material can be deposited into the windows. Finally, a stronger organic solvent dissolves the unexposed polymer, and if the latter method is used, any newly deposited material resting on that unexposed resist is removed. Both positive and negative EBL methods are used in this dissertation; the former is used to define the silicon photonic structures by etching away unwanted silicon, while the latter is used to deposit the VO<sub>2</sub> on only the desired locations. Note that in this dissertation

another etching method – oxygen-plasma cleaning – is used to clean the substrate before deposition but should not be confused with the former process, which involves etching through the silicon layer.

#### **2.3.4. Reactive-Ion Etching**

Reactive-ion etching is a technique for removing material from the surface of a sample, in which an intense RF electromagnetic field induces a plasma and the resulting ions are accelerated toward the sample surface. The rate at which material is removed depends upon the gases allowed into the vacuum chamber during the procedure, the chemical properties of the exposed portions of the sample, and the applied RF power.

## CHAPTER 3

### DESCRIPTION OF VO<sub>2</sub> PHASES BY DENSITY FUNCTIONAL THEORY

#### 3.1. Introduction

Although developing a firm understanding of the origin of the vanadium dioxide phase transition is of acute interest in the physics community, the knowledge could also inform and improve the next generation of modulators. The description of the mechanism driving the VO<sub>2</sub> phase transition might provide insight into the response of VO<sub>2</sub>-based devices as well as suggest other phase-change materials that might provide similar properties. In particular, an understanding of the transient metallization exploited in the VO<sub>2</sub>-based devices is crucial to their development.

My contributions to this work included leading the successive revisions of the initial draft to turn it into a publishable document. This process required numerous nuanced discussions about the interpretation of the results in light of the history of theoretical descriptions of VO<sub>2</sub>, experimental characterization of its rich phase diagram, and its importance as a test bed for the continuing development of density functional theory. The work in this chapter is published in reference [50].

#### 3.2. History of Theoretical Descriptions of VO<sub>2</sub>

The understanding of VO<sub>2</sub> phases and the complex relationships between them has been controversial for half a century. At the core of the debate lies the question of whether the insulating phases can be described by single-quasiparticle band theory or if strong

correlations must be invoked to predict the band gap from fundamental assumptions [51–54]. In 1971, Goodenough suggested that the band gap originates from the formation of V-V pairs [55], but just four years later, Zylbersztein and Mott proposed that the band gap in VO<sub>2</sub> follows largely from strong electron correlations [56]. This latter thesis gained support from experimental data that showed behavior similar to the generic, non-material-specific predictions of correlated-electron model Hamiltonians [53,57]. In 1994, density functional theory (DFT) calculations for the M1 phase favored a Peierls-like dimerization of vanadium atoms as the root of insulating behavior [58]. However, those single-quasiparticle calculations did not yield a true band gap, a failure which strengthened arguments for a Mott-Hubbard description of the band gap [57,59]. In 2005, Biermann *et al.* carried out dynamical mean-field theory calculations, effectively incorporating electron correlations into DFT calculations which previous yielded no band gap [60]. They found a nonzero gap for the M1 phase, but concluded that the M1 phase *is not a conventional Mott insulator*. Instead, the finite band gap was attributed to a *correlation-assisted Peierls transition*. The role of strong correlations in opening the VO<sub>2</sub> band gap was further corroborated in more recent calculations by Weber [61].

In the last few years, predicting experimental VO<sub>2</sub> characteristics has become a test bed for single-particle theories. In 2007, Gatti *et al.* [62] calculated VO<sub>2</sub> energy bands using the approximation of Hedin [63] for the one-electron Green's function, which substitutes the bare Coulomb potential in the Hartree-Fock approximation by an energy-dependent screened Coulomb interaction. These calculations produced an energy gap in the M1 phase and a metallic rutile phase as expected. In 2011, Eyert [64] reported energy-band calculations using hybrid exchange-correlation functionals, in which a fraction of the local exchange potential

is replaced by a Hartree-Fock exchange. He obtained satisfactory energy gaps for the insulating phases, duplicating the success of Gatti *et al.* [62], and addressed the issue of magnetic ordering. Although this initial success led to more comprehensive studies [65–67], no single exchange-correlation functional has been found that predicts both the observed energy gaps and magnetic orderings of VO<sub>2</sub> phases. As a result, the role of strong electron correlations in the phase transition of VO<sub>2</sub> and therefore the applicability of single-particle band theory to VO<sub>2</sub> remains in dispute.

### 3.3. Details of the Density Functional Theory Calculations

Hybrid density functional theory computations were performed for each VO<sub>2</sub> phase using a plane-wave basis and the projector-augmented-wave method [68] as implemented in the Vienna Ab initio Simulation Package [69]. The unique results of these calculations are assumed to follow from two unique choices of parameters for the energy-band calculations of the principal phases of VO<sub>2</sub>: (1) significantly harder pseudopotentials were used for both oxygen and vanadium and (2) an optimized mixing parameter in a hybrid functional was used for the exchange-correlation potential. For each VO<sub>2</sub> phase, several magnetic configurations were calculated to determine the lowest energy magnetic ordering. The exchange and correlation were described by a tuned PBE0 hybrid functional [70,71] that contains 7% Hartree-Fock exchange. The percentage was chosen to yield an energy gap for M1 in agreement with experiment.

These calculations provide a more accurate description of the vanadium and oxygen atoms for two reasons. First, thirteen electrons ( $3s^23p^63d^44s^1$ ) were treated as valence electrons for vanadium atoms instead of the typical eleven electrons [64,65]. For the oxygen

atoms, six electrons ( $2s^2 2p^4$ ) were treated as valence electrons, as is common practice. Second, the oxygen pseudopotential utilized in these calculations was harder (i.e., the core radius is smaller) than that which is typically used. The AFM-M1 (antiferromagnetic-M1) phase was found to be metastable using typical oxygen pseudopotentials but is unstable using a hard potential, which implies a delicate balance between competing effects. This result is consistent with the complex phase diagram of  $\text{VO}_2$  involving multiple competing phase transitions. The harder pseudopotentials have an effect on the magnetic order because it affects bond lengths and angles, which, according to the Goodenough-Kanamori rule [33,72,73], indirectly affects whether a certain magnetic order can be stabilized or not.

As required by the harder oxygen pseudopotential, the plane-wave cutoff energy was set at 700 eV, but a cutoff energy of 800 eV caused no appreciable changes. All Brillouin-zone sampling was based on  $\Gamma$ -centered k-point grids:  $3 \times 3 \times 3$  grids were used for the M1 and M0 unit cells that each contain 12 atoms, a  $4 \times 4 \times 6$  grid was chosen for the R unit cell with 6 atoms, and a  $1 \times 2 \times 2$  grid was utilized for the M2 unit cell with 24 atoms. The self-consistent electronic calculations were converged to  $10^{-4}$  eV between successive iterations and the structural relaxations were converged so that the total-energy difference between two successive ionic steps is  $10^{-3}$  eV. The initial magnetic configuration was set by assigning a moment of 0, +1, or -1 Bohr magneton on each vanadium atom, resulting in three possible initial configurations: NM (nonmagnetic, all moments set at 0), FM (ferromagnetic, all moments set at +1), and AFM (antiferromagnetic, moments alternating between +1 and -1). During self-consistent field calculations of the electronic structure, the magnetic moments on all atoms were allowed to vary.

### 3.4. Computation Results

Density functional theory calculations with hard pseudopotentials and an optimized hybrid exchange functional, as described above, correctly predict the energy gaps and magnetic orderings of both monoclinic VO<sub>2</sub> phases, the metallic nature of the high-temperature rutile phase, and are consistent with available experimental data. This result suggests that it is not necessary to invoke strong electronic correlations to accurately describe VO<sub>2</sub>. Using these calculation parameters, a potential candidate was found for the metallic monoclinic phase discussed in recent publications.

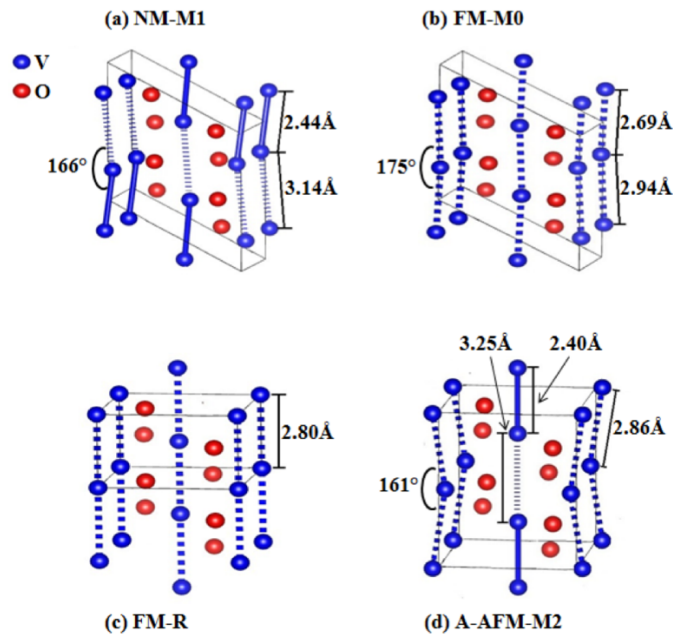


Figure 3.1. Optimized crystal structures found with density functional theory calculations. (a) Nonmagnetic-M1, (b) ferromagnetic-M0, (c) ferromagnetic-R, and (d) antiferromagnetic (A-AFM) M2. Oxygen atoms are shown in red, and vanadium atoms are blue. The strongest V-V bonds (defined as  $<2.50 \text{ \AA}$ ) are depicted as solid lines, while the weakest V-V bonds ( $>3.00 \text{ \AA}$ ) are displayed as dotted lines. Bonds between  $2.50$  and  $3.00 \text{ \AA}$  represented by dashed lines. Reprinted with permission from reference [50].

The optimized crystal structures in Figure 3.1 have all expected features of the experimentally observed crystal structures: all V-V chains of M1 and M0 are both canted and dimerized, R has only undimerized straight V-V chains, and the monoclinic M2 phase has both straight dimerized V-V chains and undimerized but canted antiferromagnetic V-V chains [52,74–77]. In addition to that qualitative agreement, the calculated lattice constants and angles as well as vanadium-vanadium (V-V) bond lengths and V-V angles are in good agreement with corresponding experimental values (see Table 3.1). Although our lattice constants and V-V bond lengths are somewhat smaller than the corresponding experimental values, density functional theory calculations simulate atoms at 0 K, not the finite temperatures available to experiments.

First, we consider the magnetic and electronic properties of the R phase. Experiments have shown that the R phase is PM above the transition temperature of 340 K [78,79]. According to the present calculations, the total energies of antiferromagnetic R (AFM-R) and NM-R are higher than ferromagnetic R (FM-R) by 125 and 140 meV per formula unit, respectively. Although the calculations predict FM-R to be the ground state of R, the temperature at which DFT calculation must be performed (0 K) is well below any hypothetical Curie temperature of R-VO<sub>2</sub>. However, the crystal structure of VO<sub>2</sub> is monoclinic at temperatures below 340 K so we cannot directly compare the calculated FM ground state to an experimentally observed phase, so we can only state that our FM-R prediction is not inconsistent with the experimental observations of PM-R [78,79]. As shown in Table 3.2, FM-R is metallic, in agreement with experiment [78,79], dynamical mean field theory (DMFT) calculations [60], and a previous hybrid-functional calculation [80], but unlike the hybrid calculations in references [65,66]. In Figure 3.2(a), the total density of

states (DOS) of FM-R is compared to the experimental x-ray photoelectron spectra [81] and with DMFT results [60]. The overall shape of the DOS agrees with the experimental data. In particular, a feature at -1.3 eV that is present in the experimental data [81], in previous DMFT results [60] (attributed to a lower Hubbard band), and in GW calculations (attributed to a plasmon) [62] is reproduced in the DOS computed in the present work.

		M1	NM-M1	mM	FM-M0	R		M2	
		Exp [77]	This work	Exp [76]	This work	Exp [74]	This work	Exp [75]	This work
a (Å)		5.75	5.53	5.69	5.59	4.55	4.42	9.07	8.98
b (Å)		4.54	4.51	4.59	4.50	4.55	4.42	5.80	5.65
c (Å)		5.38	5.28	5.29	5.29	2.85	2.80	4.53	4.48
$\alpha, \gamma$ (°)		90	90	90	90	90	90	90	90
$\beta$ (°)		122.65	121.93	122.61	122.05	90	90	91.88	91.88
V-V bond (Å)	short	2.62	2.44	2.72	2.69	2.85	2.80	2.54	2.40
	middle							2.93	2.86
	Long	3.17	3.14	2.98	2.94			3.26	3.25
V-V angle (°)		168	166		175	90	90	162	161

Table 3.1. Comparison of lattice constants, V-V bond lengths, and V-V bond angles found with these DFT calculations and in experimental work (Exp). Note that the values for the FM-M0 phase are compared to the values for the monoclinic metallic state (mM) determined from x-ray absorption fine structure experiments. Table adapted with permission from reference [50].

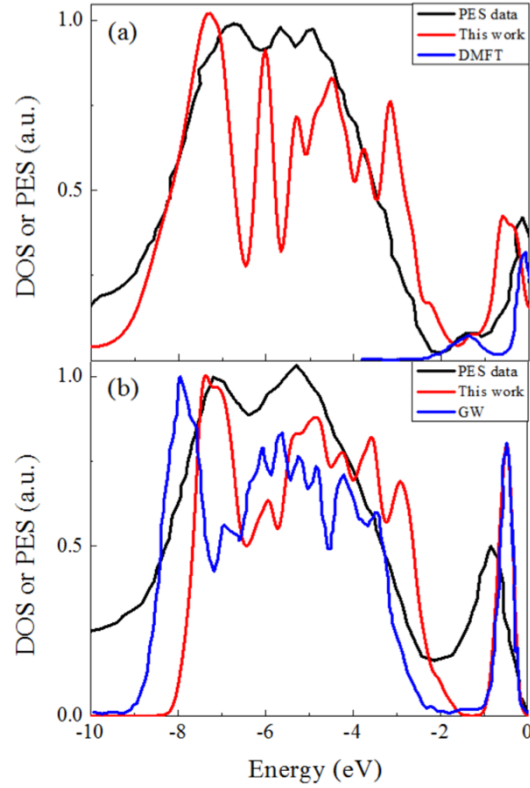


Figure 3.2. (a) The density of states (DOS) for the ferromagnetic rutile phase (FM-R) calculated in this work (red) is compared with the experimental [81] photoemission spectrum (black) and the V-3d ( $t_{2g}$ ) spectral weights (blue) from LDA+DMFT calculations [60]. The 1.3 eV satellite feature is clearly found in this work. (b) The total DOS of NM-M1 calculated in this work (red) is compared with the experimental [81] photoemission spectrum (black) of the low temperature insulating M1 and the DOS (blue) from GW calculations [62]. Each DOS from this work was convoluted with a Gaussian function. Reprinted with permission from reference [50].

We next consider the magnetic and electronic properties of the M1 phase. Conflicting reports of paramagnetic [78,79] and diamagnetic [82] susceptibilities for M1 suggest that M1 probably has a negligible magnetic susceptibility, and that experimental values are potentially affected by fabrication parameters; we therefore designate it as NM as previous authors have done [65]. The optimized AFM-M1 spin configuration relaxes to the more

stable NM-M1 in contrast to previous hybrid DFT results [64,65,67,80] but consistent with experiment [78,79,83]. As can be seen in Table 3.2, we obtain a band gap of 0.63 eV for NM-M1 in good agreement with the experimental value [79,81,84] of about 0.7 eV and the values obtained from DMFT [60,61] and GW [62] calculations. In Figure 3.2, the total DOS of NM-M1 is compared to the experimental XPS spectra [81] and the GW DOS calculated in reference [62]. The shape of the DOS and the positions of peaks from -10 to 0 eV agree well with the experimental results [81] and with the GW DOS. This comparison confirms that the electronic structure of the insulator phase NM-M1 is correctly reproduced by the present hybrid DFT calculations.

In addition to the NM-M1 and FM-R phases, the present hybrid DFT calculations predict a stable ferromagnetic state, FM-M0, with a structure intermediate between NM-M1 and FM-R. Calculations starting from the FM-M1 configuration converge to FM-M0 during geometry optimization. Since the total energy of FM-M0 is lower than the calculated energy of the commonly accepted ground state, NM-M1, by 50 meV per formula unit, we suggest that VO<sub>2</sub> may be ferromagnetic at very low temperatures. A low Curie temperature could account for the discrepancy between the predicted ferromagnetism and the finite magnetic susceptibility observed in experiments at moderately low temperatures [85,86]. Between 10 K and the insulator-to-metal transition at about 340 K the magnetic susceptibility is small [86], reinforcing the conventional wisdom that NM-M1 is the stable phase above 10 K.

It is noteworthy that initial configurations of AFM-M0 and NM-M0 both converge to NM-M1 when the initial magnetic moments are allowed to change during the calculation. Along with the fact that FM-M1 converges to FM-M0, these results hint at the complex interplay of magnetic and structural degrees of freedom, and highlight the necessity of more

magnetic measurements at low temperatures to confirm experimental results [85,86] and these predictions. In other words, the input magnetic ordering of (FM or NM) is a stronger determinant of the output crystallographic structure (M0 or M1, respectively) than the input crystallographic structure. It is also interesting that both phases of VO<sub>2</sub> simulated to be ferromagnetic, M0 and R, are half metals similar to CrO<sub>2</sub> [76,87] suggesting half metallicity and ferromagnetism are correlated in transition-metal oxides.

Similar to NM-M1, the FM-M0 configuration has a simple monoclinic lattice with space group P21/c ( $C_{2h}^5$ , No. 14) and dimerized zigzag V-V chains. However, the crystal structures of NM-M1 and FM-M0 exhibit subtle differences, as shown in Figures 3.1(a) and 3.1(b). The short V-V bond of FM-M0 is longer and the long bond is shorter than the corresponding bonds in NM-M1. Therefore, the FM-M0 crystal structure can be viewed as an intermediate phase between the crystal structures of NM-M1 and FM-R. In fact, both the short and long V-V bonds of FM-M0 are closer to the bond length found in FM-R than their NM-M1 counterparts, indicating a FM-M0 intermediate state would be structurally closer to FM-R than to NM-M1. Furthermore, the 175° bond angle of FM-M0 is also closer to the 180° angle found in FM-R than the 166° angle of NM-M1. Diffraction measurements and optical or electrical measurements below the Curie temperature are needed to verify the structure and metallic character of the FM-M0 phase.

		Experiment	Theoretical results					
			This work	HSE			GW	DMFT
				[64] <sup>c</sup>	[65] <sup>d</sup>	[67]	[62]	[60] <sup>g</sup>
Magnetic ground states	M0	FM/PM [85,86] <sup>a</sup>	FM					
	M1	NM [82,83] <sup>b</sup>	NM		AFM	AFM		
	M2	AFM [52]	A-AFM			FM		
Band gap (eV)	M1	0.6-0.7 [79,84]	0.63	1.10	2.23 (AFM) 0.98 (NM) <sup>e</sup>		0.65	0.60
	M2	>0.10 [88]	0.56	1.20				
	R	0 [79,84]	0	0	1.43 (FM) 0 (NM) <sup>f</sup>		0	0

Table 3.2. Magnetic states and band gaps for various VO<sub>2</sub> phases compared to experiments and other theoretical calculations. Table adapted with permission from reference [50].

- <sup>a</sup> Divergence of the magnetic susceptibility below 30 K underlines the importance of exploring the unknown low-temperature magnetic properties.
- <sup>b</sup> The disagreement of measurements of small positive [83] susceptibility and another publication [82] reporting small negative susceptibility justified our designation of M1 as NM as similar to previous authors [65].
- <sup>c</sup> Band gap of each VO<sub>2</sub> phase was calculated by assuming the magnetic state found in experiments.
- <sup>d</sup> Non-spin-polarized calculations similar to those of Eyert [64] were reproduced and then spin-polarized calculations for each potential magnetic state were performed [65].
- <sup>e</sup> The correct magnetic phase, NM-M1, has a calculated band gap close to the experimental value. However, AFM-M1 was calculated to be lower in energy, and its band gap is more than triple the expected value.
- <sup>f</sup> A ferromagnetic R phase with a band gap of 1.43 eV was calculated to be the ground state. However, a NM state with a correct band gap of 0 was also obtained, albeit at a higher energy.
- <sup>g</sup> A stable nonmagnetic structure was obtained with cluster-DMFT, but it was not compared to other magnetic states to determine the ground state.

Recently, a stable metallic monoclinic VO<sub>2</sub> phase (mM) has been observed near room temperature in thin films [76] and single crystals under high pressure [89]. We found that the crystal structures and metallic character of the predicted FM-M0 and the experimental mM phases are very similar, which suggest that FM-M0 may be related to this mM phase. In the thin films [76], x-ray absorption fine-structure spectroscopy (XAFS) demonstrated that the short V-V bond elongates, the long V-V bond shortens, and zigzag V-V chains straighten when VO<sub>2</sub> metallizes [76], leading to an intermediate crystal structure with lattice constants and bond lengths nearly identical with those for FM-M0 shown in Table 3.1. Pressure-dependent Raman spectroscopy, mid-infrared reflectivity, and optical conductivity measurements confirmed an insulator-to-metal transition without an accompanying structural transition from monoclinic to the rutile phase [89]. However, although a subtle change in structure was attributed to the appearance of the M2 phase, that assignment explains neither the metallization nor the fact that intermediate Raman spectra are unlike those of either M2 or M1 [89]. Instead, a monoclinic metallic phase, such as M0, with slightly different crystal structure than either M1 or M2, would explain both the mM phase in thin film samples [76] and the metallic monoclinic VO<sub>2</sub> phase that appears under high pressure [89]. The similar crystal structures and metallic character of the predicted FM-M0 and the experimental mM states suggest that FM-M0 may be related to this mM phase.

Although most work on VO<sub>2</sub> over the past fifty years has focused exclusively on the transition between the insulating M1 and metallic R phases, multiple authors [52,57,64,90,91] have suggested that the M2 insulating phase may hold the key to a complete understanding of the VO<sub>2</sub> phase transition. Three possible AFM configurations [92] designated as A-AFM, G-AFM, and C-AFM are shown in Figure 3.3(a), 3.3(b), and 3.3(c),

respectively. Each configuration represents a unique magnetic ordering of the zigzag chains, while the straight chains have no moments. The A-type and G-type exhibit antiparallel moments along the canted zigzag V-V chains [52]. For A-AFM, moments on V-atoms in a canted zigzag chain are parallel to moments of its nearest V-atom neighbors on the next canted chain, while they are antiparallel for G-AFM and C-AFM. However, the moments of all vanadium atoms on a single chain are aligned in C-AFM.

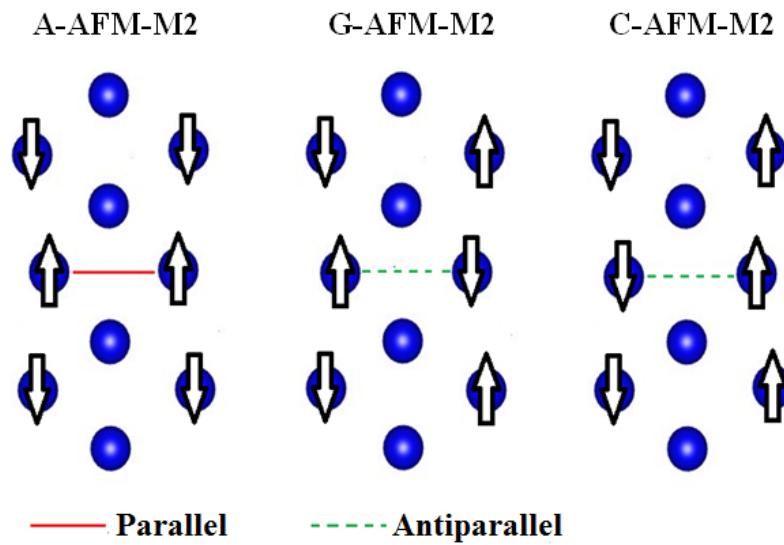


Figure 3.3. (a) Schematic of the three possible magnetic structures of AFM-M2: A-AFM, G-AFM and C-AFM. The blue solid circles are V atoms and the overlaid white arrows represent the orientation of their magnetic moment. The solid red line between two adjacent canted chains represents parallel magnetic moments between the nearest vanadium neighbors from two separate chains, while the dashed green lines represent an antiparallel configuration. The magnetic moment orientations along a single V-chain are either alternating (A-AFM and G-AFM) or constant (C-AFM). The A-AFM configuration was calculated to have the lowest energy. Reprinted with permission from reference [50].

Our calculations show that the A-AFM is the lowest-energy configuration of M2 and the G-AFM, C-AFM, FM, and NM configurations of M2 are higher in energy than A-AFM

by 4 meV, 27 meV, 16 meV, and 32 meV per formula unit, respectively. Although numerically accurate, the small energy difference (4 meV) between A-AFM and G-AFM may not be captured accurately by the approximate functionals. Nevertheless, both A-type and G-type AFM-M2 agree with the experimentally derived model in which M2 is antiferromagnetic and local magnetic moments are present only on the canted zigzag V-V chains [52]. Similarly, the present calculations show that the local magnetic moments of AFM configurations are on the canted V-V chains while the straight, dimerized chains have negligible moments. The band gap of 0.56 eV calculated for A-AFM-M2 is in agreement with photoelectron spectroscopy (PES) of M2 quoting a band gap greater than 0.1 eV [88]. Furthermore, our value of 0.56 eV is consistent with the band model proposed by Goodenough [93] in which the band gap for M2 is comparable to, but smaller than, the band gap of M1 (0.6-0.7 eV).

### 3.5. Discussion and Impact of Results

The kernel of the long-standing debate about  $\text{VO}_2$  is whether the electronic properties of this material are better described by band theory in which electrons are represented by non-interacting quasiparticles that experience the same single-particle crystal potential, or by a many-body approach in which electron-electron interactions are explicitly incorporated. In principle, band theory can always describe any given material: ground-state properties are describable by DFT, which is an exact theory, assuming that a satisfactory exchange-correlation potential  $V_{xc}(r)$  can be constructed; excitations can be described by Hedin's GW expansion of the self-energy  $\Sigma(r, r'; E)$  followed by solving the Bethe-Salpeter equation (BSE) [94] to include electron-hole interactions. Both the DFT and Hedin equations look like

Schrödinger equations: the  $V_{xc}(r)$  in DFT is replaced by the nonlocal, energy-dependent  $\Sigma(r,r';E)$  in order to describe excitations. Using these equations, one gets quasiparticle energy bands, single-particle excitations, excitons (via the BSE), and plasmons (from the zeros of the real part of the single-particle dielectric function [95]), but the energy dependence in  $\Sigma(r,r';E)$  is often essential [61]. The standard procedure is to first solve the DFT equation with a reasonable choice of  $V_{xc}$ , and then use the solutions to construct  $\Sigma(E_k)$ , which are in turn used to correct the DFT energy bands. Ideally, the process should be carried to self-consistency to eliminate the effect of the initial  $V_{xc}$  choice. Gatti *et al.* [62] have already demonstrated that this process correctly predicts the band gap of insulating monoclinic VO<sub>2</sub>; however, the numerical procedures are quite cumbersome and magnetic calculations require separate, self-consistent GW calculations. Hybrid exchange-correlation functionals constitute an attempt to construct a  $V_{xc}(r)$  that also serves as a local, energy-independent approximation to  $\Sigma(r,r';E)$ , known as the COHSEX (Coulomb hole plus screened exchange) approximation [62]. The fact that  $\Sigma(r,r';E)$  is material specific justifies tuning the mixing parameter in the hybrid functional, as is done in the present paper. In this way, the tuned exchange-correlation functional models  $\Sigma(r,r';E)$  for each material. Similarly, the Hubbard U, which is present in theories that incorporate explicit electron-electron interactions, is also often treated as a free parameter. Here we have demonstrated that, by tuning the mixing parameter of a hybrid functional and using harder-than-usual pseudopotentials, the single-particle approach correctly yields both the electronic and magnetic properties of VO<sub>2</sub> phases; however, the underlying nature of the phase transition is not addressed here.

DFT and GW calculations serve as rigorous **quantitative** tests of quasiparticle theories. The early conclusions that VO<sub>2</sub> is a strongly correlated material were based on

model many-body Hamiltonians. Experimental data in the region of the phase transition were compared with the corresponding model behavior [54,57]. The appearance of correlated behavior at the phase transition, however, does not necessarily imply that strong correlations persist at temperatures away from the phase transition. Quantitative theories based on strong correlations, such as LDA+U, GGA+U and DMFT, assume at the outset that strong electron-electron interactions, incorporated via the Hubbard-model on-site parameter  $U$ , dominate. In the case of  $\text{VO}_2$ , LDA+U yields insulating behavior for both the monoclinic and rutile phases [96,97]. The DMFT calculations by Biermann *et al.* [60] and by Weber *et al.* [61] are anchored on a zero-gap DFT calculation and found that strong correlations are needed to reproduce the observed value of a Peierls-induced energy gap. However, these methods have not yet been used to study the competing magnetic orderings. Thus, only the present calculations, based on band theory, reproduce the observed structural, electronic, *and* magnetic properties of *all*  $\text{VO}_2$  phases. The present band theory, DMFT, and GW/COHSEX all give a band-gap value in accord with experiment, which raises the following challenge: If DMFT and GW/COHSEX calculations were to be anchored on the present hybrid-functional band structure, which yields a correct energy gap, instead of the zero-gap LDA band structure, would they retain this value of the energy gap? If so, the role of correlations beyond what is captured by the present hybrid functional would be negligible. Clearly, such calculations would be valuable to establish the origin of the agreement between seemingly incompatible theories.

In conclusion, our study underlines the power of the hybrid DFT approach to produce a comprehensive theoretical picture of all the major  $\text{VO}_2$  phases and their magnetic properties. We have successfully reproduced the electronic and magnetic properties of M1,

M2, and R phases of VO<sub>2</sub> using DFT calculations with a hybrid functional and accurate pseudopotentials. The success of these hybrid DFT calculations suggests that band theory can provide an adequate description of VO<sub>2</sub> phases despite the unusually large coupling between magnetic and structural degrees of freedom in VO<sub>2</sub>. The strength of that coupling is perhaps displayed more clearly in this work than ever before given the strong influence that the initial magnetic state has on the optimized crystal structure. Moreover, the present calculations predict a new monoclinic ferromagnetic metal state of VO<sub>2</sub>, which accounts for the magnetic data at low temperature and is also a candidate for the recently observed metallic monoclinic mM phase that appears in thin films or under high pressure. In addition, the antiferromagnetic structure of M2 was predicted to be A-type. Experimental verification of ferromagnetism in room-temperature VO<sub>2</sub> under high pressure, as well as structural and electronic measurements at low temperatures in unstrained VO<sub>2</sub>, clearly set important priorities for future research to test the validity of these particular findings.

## CHAPTER 4

### NANOSCALE HOLOGRAPHIC IMAGING OF VANADIUM DIOXIDE THIN FILMS WITH X-RAYS

#### 4.1. Introduction

Although the phase transition of vanadium dioxide was discovered [98] as early as 1959, the nature of the VO<sub>2</sub> phase transition holds mysteries to this day. One mystery of particular importance to a VO<sub>2</sub>-based optical modulator is the transient behavior when pumped by ultrafast pulses at low-fluence. Understanding the short-lived monoclinic metal phase could improve device performance. For example, stabilizing the crystallographic configuration of the transient state could enable lower switching fluences of the film and thus lower energy consumption of the device.

In this chapter, the crystal structure and electronic state of the VO<sub>2</sub> are simultaneously probed with 50 nm spatial resolution to gain insight into the role of defects in the phase transition. These x-ray holography measurements suggest that the M2 phase plays a pivotal role in the phase transition, perhaps nucleating the transformation at temperatures slightly below the transition temperature. Although I played only minor roles in the interpretation of results and preparation of the manuscript, published in reference [99], my main contribution to this work, discussed more thoroughly in section 4.3, was developing a pulsed laser deposition recipe that would not damage gold apertures on the opposite size of the Si<sub>3</sub>N<sub>4</sub> membranes necessary for the experimental configuration. This represented a major step forward in the deposition processes available in our laboratory.

## 4.2. Overview of X-Ray Holography

The diffraction limit suggests that electron or x-ray beams, with wavelengths of only a few nanometers, are a prerequisite for nanoscale imaging. Electron beams, unlike x-ray beams, suffer from space-charge spreading [100] due to Coulombic repulsion. However, manipulating light in the x-ray region, as when focusing on the sample, is challenging. Furthermore, obtaining nanoscale resolution with a focused x-ray beam spot would require rastering the beam spot and time-consuming measurements.

As an alternative to direct real-space imaging, x-ray holographic imaging can be used to reconstruct a real-space image from a momentum-space image. In these experiments, an x-ray beam, which is approximately collimated, is split into two beams; one of the beams passes through the sample, while the reference beam does not. A Fourier transform can be performed on the interference of the two beams to obtain a real-space image with nanoscale spatial resolution. This method, using a collimated x-ray beam, does not require focusing of the x-rays and no need for rastering.

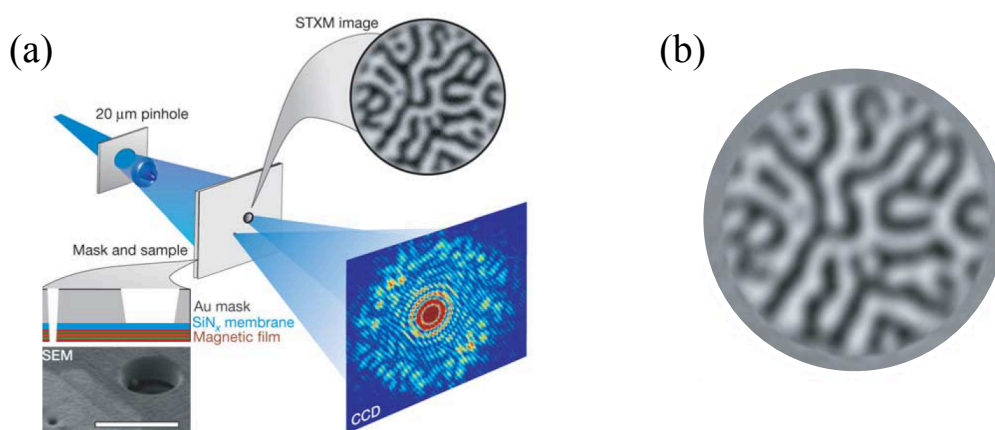


Figure 4.1. (a) Experimental configuration for the Eisebitt experiment. Inset shows scanning transmission x-ray micrograph of the Co/Pt multilayer film used in the experiment. (b) Holographic image of the Co/Pt multilayer film computed in the Eisebitt experiment. Images adapted with permission from reference [101].

Figure 4.1(a) illustrates an experimental configuration for x-ray holography [101]. A 20- $\mu\text{m}$  pinhole acts as a coherence filter for the monochromatic synchrotron x-rays. The mask is far enough away (7.23 meters in the Eisebitt experiment) from the 20- $\mu\text{m}$  pinhole that the center Airy disk diffracted from the circular aperture illuminates both holes in the gold mask with high enough coherence to enable holography. The smaller hole in the gold mask, extending the entire way through the sample, acts as the reference beam. The larger hole contains the area of interest. In the Eisebitt experiment, the sample is a stack of alternating cobalt and platinum films and it is imaged directly with scanning transmission x-ray microscopy (STXM), similar to SEM, and shown in the greyscale image in Figure 4.1(a). The interference of the reference and sample beams, referred to as a hologram, is collected by the CCD camera; an example for the Eisebitt experiment is found in color in Figure 4.1(a). A holographic image that reproduces the real space image can be obtained by computing the Fourier transform of the hologram, seen in Figure 4.1(b) for the Eisebitt experiment. The STXM image in Figure 4.1(a) is in good agreement with the holographic image, Figure 4.1(b), demonstrating the ability of this lens-less imaging technique to produce a real-space image. Note that by tuning the electric-field polarization and x-ray wavelength of synchrotron, this holographic imaging technique can provide element- and polarization-specificity of the x-ray absorption spectrum. Furthermore, since holography is an interference-based imaging technique, it is sensitive to the relative shifts of the amplitude and phase of the transmitted light across the sample. Thus, it is particularly well-suited for measuring phase-separated materials, which modulate the local transmission, even on the nanoscale [101].

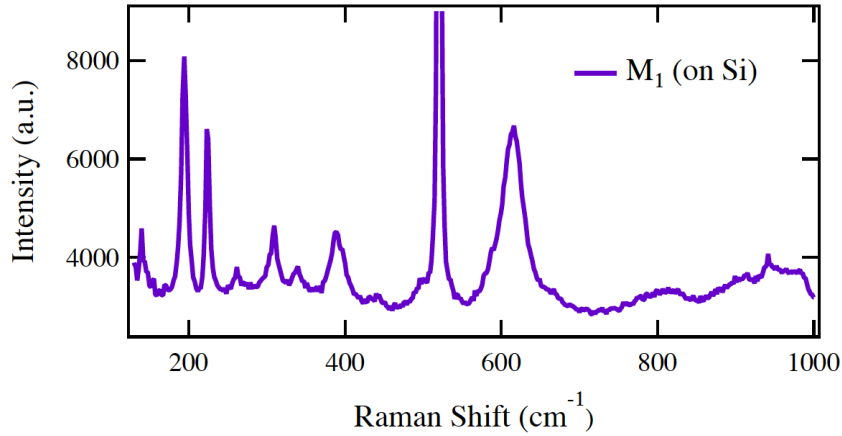


Figure 4.2. Raman spectrum of film near  $\text{Si}_3\text{N}_4$  window demonstrates that the  $\text{VO}_2$  is in the M1 phase at room temperature. The saturated peak at about  $520 \text{ cm}^{-1}$  corresponds to the silicon substrate. Reprinted with permission from reference [99].

### 4.3. Sample Fabrication and Characterization

Samples were fabricated by pulsed laser deposition on  $\text{Si}_3\text{N}_4$  membranes and were shown to be in the M1 phase by Raman scattering as seen in Figure 4.2. In addition, the  $\text{VO}_2$  is confirmed to undergo the phase transition by measuring the transmission of light through the  $\text{VO}_2$  as a function of temperature, as shown in Figure 4.3. For these measurements, the emission from a tungsten-halogen lamp was filtered to give light only with wavelengths longer than 1310 nm and focused onto the  $\text{VO}_2$  film on the  $\text{Si}_3\text{N}_4$  window with a microscope objective. The transmitted infrared light was collected with a second microscope objective and measured with an InGaAs photodiode. The sample was mounted on a copper plate with a hole to allow transmission of the light, and the copper plate was heated by a Peltier thermoelectric device.

The fabrication of these devices required depositing VO<sub>2</sub> thin films on 40-nm Si<sub>3</sub>N<sub>4</sub> membranes with gold apertures on the backside. Typically, a laser power of 325 mJ/pulse, corresponding to fluence of about 2 J/cm<sup>2</sup> on the vanadium metal target, has been used during the pulsed laser deposition of VO<sub>2</sub> in our group [49]. However, this recipe was found to destroy the gold apertures. This damage was ascribed to local melting of the gold as a result of the heat generated in the sample by the energy VO<sub>2</sub> species, a lack of a good thermal sink in the form of a thick substrate, and the inability of the atmosphere to wick heat away from the sample in the form of convection since the deposition was done under vacuum. Instead, a laser power of about 260 mJ/pulse, or about 1.6 J/cm<sup>2</sup> on the target, was used. Although this was a reduction in laser power of about 20%, it doubled the deposition time for the VO<sub>2</sub> films. More importantly, it decreased the number of gold apertures destroyed during the deposition from greater than 90% to about 25%.

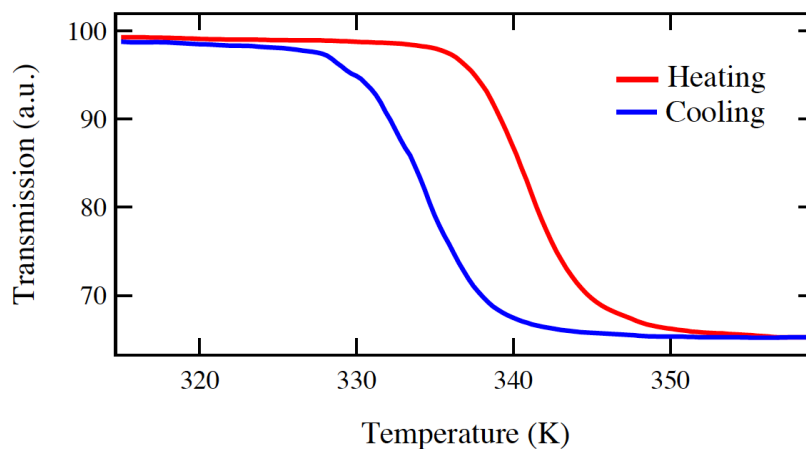


Figure 4.3. Transmission of white light through the VO<sub>2</sub> film as a function of temperature shows a hysteresis width of about 6 K. The measurement is taken through the Si<sub>3</sub>N<sub>4</sub> window. Reprinted with permission from reference [99].

#### 4.4. X-Ray Absorption Spectroscopy and Band Diagram of the VO<sub>2</sub> Film

Recently, Gray *et al.* suggested that soft x-ray absorption spectroscopy (XAS) could be used to measure the strength of electronic correlations independent from the structural phase transition. Furthermore, the temperature dependence of the XAS signal observed by Gray *et al.* suggested that the correlations weaken before the structural changes occur. However, until this work, no measurements successfully probed both the structural and electronic aspects of the phase transition while simultaneously maintaining sufficient spatial resolution to ensure homogeneous probing. Using polarization- and wavelength-resolved x-ray holography, both the structural and the electronic degrees of freedom were imaged during the insulator-to-metal phase transition in thin films of VO<sub>2</sub> with 50 nm spatial resolution. Depending on the local environment, the phase transition can take two pathways: directly from the M1 phase to the R phase or an indirect transition through an intermediate phase. While this phase has been ascribed to the monoclinic metallic phase [37,41,42,76,102], the XAS signature suggests it is the insulating (but electronically excited) M2 phase. Nanoscale defects that affect the local strain within the sample seem to determine whether a region takes the direct or indirect pathway. These results highlight the key role played by defects in the phase transition in VO<sub>2</sub> and the ability of resonant x-ray holography for studying phase separation in correlated materials.

A schematic band diagram for the M1 and R phases, based on the Goodenough [55] model, is shown in Figure 4.4(a). In this simplified picture, which does not include correlations, the rutile  $\pi/\pi^*$  levels are bonding/anti-bonding states formed by a hybridization of the vanadium  $3d$  and oxygen  $2p$  orbitals, and the  $d_{||}$  states result from the overlap between

vanadium ions along the rutile c-axis. The monoclinic distortion of the M1 phase splits the  $d_{||}$  band into two ( $d_{||}$  and  $d_{||}^*$ ) bands and moves the  $\pi^*$  orbital above the Fermi level.

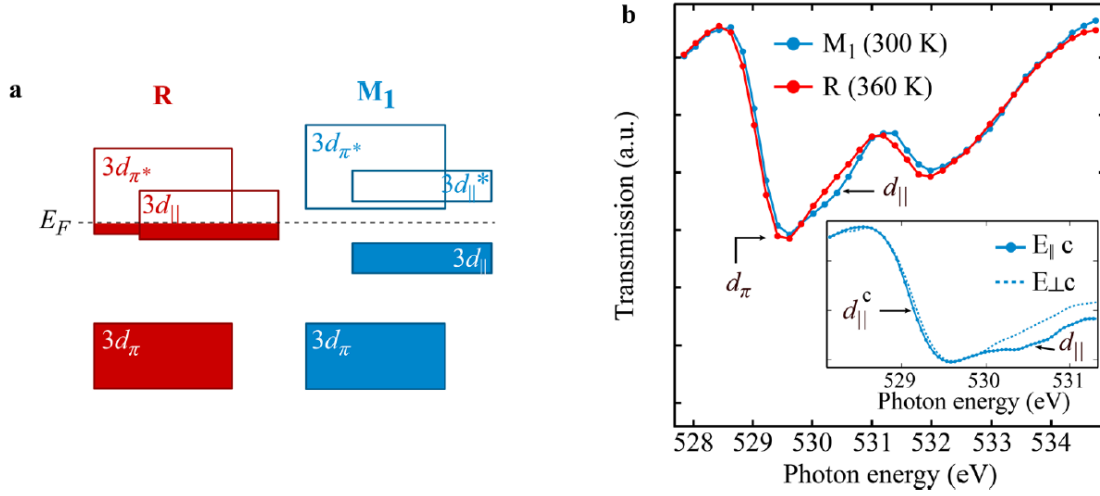


Figure 4.4. (a) Band structure of VO<sub>2</sub> as proposed by Goodenough [55]. (b) X-ray transmission at the oxygen edge shows absorptions corresponding to the transitions to the  $d_{\pi^*}$  and  $d_{||}$  states. The inset shows normalized spectra at room temperature, in the M1 phase, for x-rays parallel and perpendicular to the rutile c-axis. The polarization-dependent edge shift, labeled  $d_{||}^c$ , corresponds to the contribution from the  $d_{||}$  state due to the formation of correlated dimers [60,81]. Reprinted with permission from reference [99].

Despite its simplicity, this model can qualitatively explain most of the XAS features. Spatially integrated XAS measurements on the VO<sub>2</sub> thin films on freestanding Si<sub>3</sub>N<sub>4</sub> membranes are shown in Figure 4.4(b). Due to the strong hybridization between the oxygen  $2p$  and vanadium  $3d$  levels, XAS spectra at the oxygen K-edge also probe the  $3d$  orbitals of the vanadium ions. In the Goodenough picture, the bottom of the conduction band is the  $\pi^*$  band, which is derived from the isotropic vanadium  $d_{xy}$  and  $d_{yz}$  orbitals [55]. In the R phase, the  $\pi^*$  band moves below the Fermi level, resulting in an increase in absorption at lower energies, as observed. The  $d_{||}$  bands are derived from the vanadium  $d_{x^2-y^2}$  orbitals, which

are strongly anisotropic. Transitions into the  $d_{\parallel}$  states are only observed when the electric field vector is parallel to the rutile c-axis. When the  $d_{\parallel}$  band is split due to the structural distortion in the low temperature phase, an additional higher-energy absorption process is observed as indicated in Figure 4.4(b). This polarization-sensitive  $d_{\parallel}$ -peak allows the measurement of both the structural transition and the orientation of the sample c-axis.

Although the Goodenough model [55] predicts an isotropic  $\pi^*$  conduction band, the XAS shows a small, polarization-dependent shift [81] indicated as  $d_{\parallel}^c$  in the insert of Figure 4.4(b) in the monoclinic phase. This feature is often ascribed to effects resulting from electronic correlations [81,103], as it is found in cluster dynamical mean field theory calculations [60], where electronic correlations provide an additional contribution from the  $d_{\parallel}$  states to the bottom of the conduction band due to the formation of a correlated vanadium singlet state in the monoclinic phase.

Based on the temperature dependence of the XAS dichroism of the  $d_{\parallel}$  and  $d_{\parallel}^c$  states, Gray *et al.* argued that the singlet state is lost 7 K below the temperature of the conventional structural phase transition, and interpreted this as a sign of weakening electronic correlations prior to the structural transition [103]. This may explain the monoclinic-like metallic phases that have been observed [42,102,104], which also occur near the conventional structural transition temperature. However, in this temperature range, both the metallic and insulating phases have been observed to coexist. Furthermore, from area-integrated XAS measurements, it is unclear if the loss of correlations is homogeneous or heterogeneous across the sample, or if nanoscale phase coexistence may affect the interpretation of the spectra. Resonant soft x-ray holographic imaging can directly address this issue.

#### 4.5. Comparison of Electron Microscopy and X-Ray Holography

Although the  $\text{Si}_3\text{N}_4$  substrate is amorphous, regions of the sample with micron-sized single crystals of  $\text{VO}_2$  can be found among smaller crystallites; those larger crystals are the focus of this study as indicated in Figure 4.5. Figure 4.5(a) shows an SEM image of a  $\text{VO}_2$  thin film. On the perimeter of these single crystals, several defects can be observed, with features as small as 50 nm. In Figure 4.5(b), the same region of the thin film is reconstructed by x-ray holography. For these measurements, the x-rays were tuned to the  $d_{\parallel}$  peak, providing maximum contrast for the insulator-metal transition. There is good agreement between the SEM image in Figure 4.5(a) and the holographic image at room temperature, shown in Figure 4.5(b), considering the difference in the origin of the contrast in the two imaging techniques.

When the sample is heated to 330 K, near the phase transition temperature, bright stripes can be observed across the crystallite as seen in Figure 4.5(c). These stripes are metallic filaments that are observed because the sample has a higher transmissivity when metallic at the photon energy corresponding to the  $d_{\parallel}$  x-ray absorption feature. These domains, while long, can be as narrow as 50 nm at 330 K and grow in width as the temperature is further increased, as demonstrated in Figure 4.5(d). Further heating eventually merges the light gray filaments (not shown) indicating a fully metallic crystal. Defects, denoted by black arrows in Figure 4.5, appear dark in the SEM but bright in holography indicating x-ray high transmission. We associate these defects with grain boundaries between  $\text{VO}_2$  crystallites. It can be seen from Figure 4.5 that the nanoscale defects nucleate the growth of metallic areas, which then connect to form the metallic filaments, demonstrating the role of local strain in lowering the transition temperature in the vicinity of the defects.

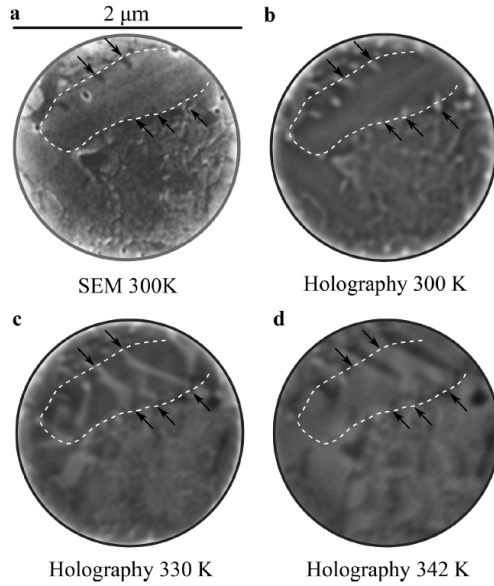


Figure 4.5. (a) SEM images of the  $\text{VO}_2$  sample show that large single crystals grow together with nanoscale crystallites. The dotted white line indicates the perimeter of a single crystal. On the edges of the crystal, several defects are observed (some indicated with black arrows). (b) Holographic image of the same sample imaged at 530.5 eV at room temperature, showing good agreement with the SEM image. (c) Same sample heated to 330 K, close to the transition temperature ( $T_c \approx 340$  K). Thin stripes appear spanning the single crystal corresponding to the metallic phase. (d) At a higher temperature, after  $T_c$ , the metallic domains grow bigger until the whole sample becomes metallic. Reprinted with permission from reference [99].

#### 4.6. Spectroscopic X-Ray Holographic Response and Local Phase Determination

This x-ray holographic technique was also used to investigate the role of electronic correlations and the presence of other phases in the growth of the metallic phase during the insulator-metal transition. To accomplish this, spectrally-resolved imaging was performed at multiple x-ray wavelengths. This imaging is performed in a different sample than that shown in Figure 4.5, with the x-rays polarized along the rutile  $c$ -axis. We collect x-ray holograms at 518 eV incident photon energy on the vanadium  $L_2$ -edge, which is also sensitive to the  $d_{||}$  states [105], at 529 eV to be sensitive to the  $\pi^*$  and  $d_{||}^c$  levels and at 530.5 eV to be resonant

to transitions into the  $d_{||}$  states. We then use the images obtained at these three photon energies to encode the red (518 eV), blue (529 eV), and green (530.5 eV) channels of a false-color image. In this spectral fingerprinting approach, we can observe if changes occur in different regions of the sample and at different temperatures. For example, if electronic correlations precede the structural transition as observed by Gray *et al.* [103], then the  $d_{||}^c$  (blue channel) will change before the  $d_{||}$  (green channel), resulting in a color change.

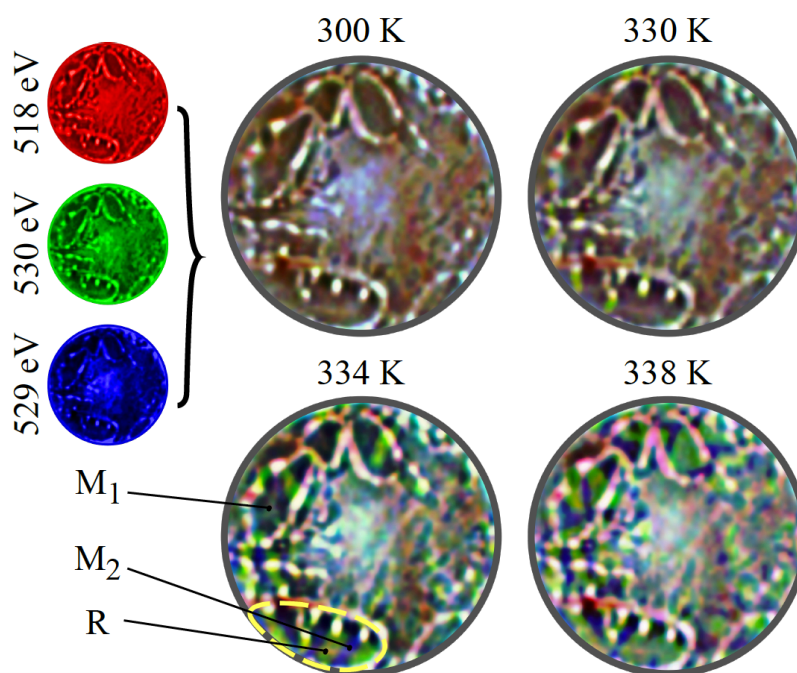


Figure 4.6. Spectrally resolved images at the vanadium and oxygen edges. The images are recorded at 518, 529 and 530.5 eV and are used to encode the intensities of the three color channels of an RGB image. At 330 K, an increase in intensity of the green channel, which probes the rutile phase through the  $d_{||}$  state, is observed in small regions similar to that observed in Figure 4.5. As the sample is heated further, it becomes clear that the blue channel, which probes the  $d_{||}^c/d_{\pi^*}$  state, also changes but in different regions. At 334 K, three distinct regions can be observed corresponding to the M1, M2, and R phases. As the temperature increases, the R phase dominates. Dashed line corresponds to the ROI shown in Figure 4.7. The circular field of view is 2  $\mu\text{m}$  in diameter.

Figure 4.6 shows the spectrally resolved changes as a function of temperature. Again, we see the formation of nanoscale domains that span the small single crystals, starting at defects. However, now we can see that in different regions of the sample the x-ray transmission changes differently. At 334 K, we can discern at least three different phases as indicated: the original M1 phase and two new phases, one with a subtle change in the  $d_{\parallel}^c$  (blue) channel and a second one with the greater change in the  $d_{\parallel}$  (green) channel.

To understand how these phases grow, we perform a finer temperature scan and focus on one of the small single crystals indicated in Figure 4.6. In addition, to amplify the changes we threshold each channel and show images at key temperatures in Figure 4.7(a). At low temperature, the sample is predominantly black within this color-coding scheme, indicating the presence of the initial M1 phase, together with some defects (red). As the sample is heated, the new phases (blue, green) nucleate at the boundaries and defects of the single crystals. At intermediate temperatures (334 K), a striped state is present between regions with changes primarily in the  $d_{\parallel}^c$  channel and in the  $d_{\parallel}$  channel, before the changes tracked by the  $d_{\parallel}$  feature dominate the region. This phase growth is captured in Figure 4.7(b), which shows the volume fraction of the blue and green regions as a function of temperature within the region of interest (ROI). Both phases start to nucleate at similar temperatures and grow, before the green area dominates, as indicated in the extracted volume fraction of each phase shown in Figure 4.7(b).

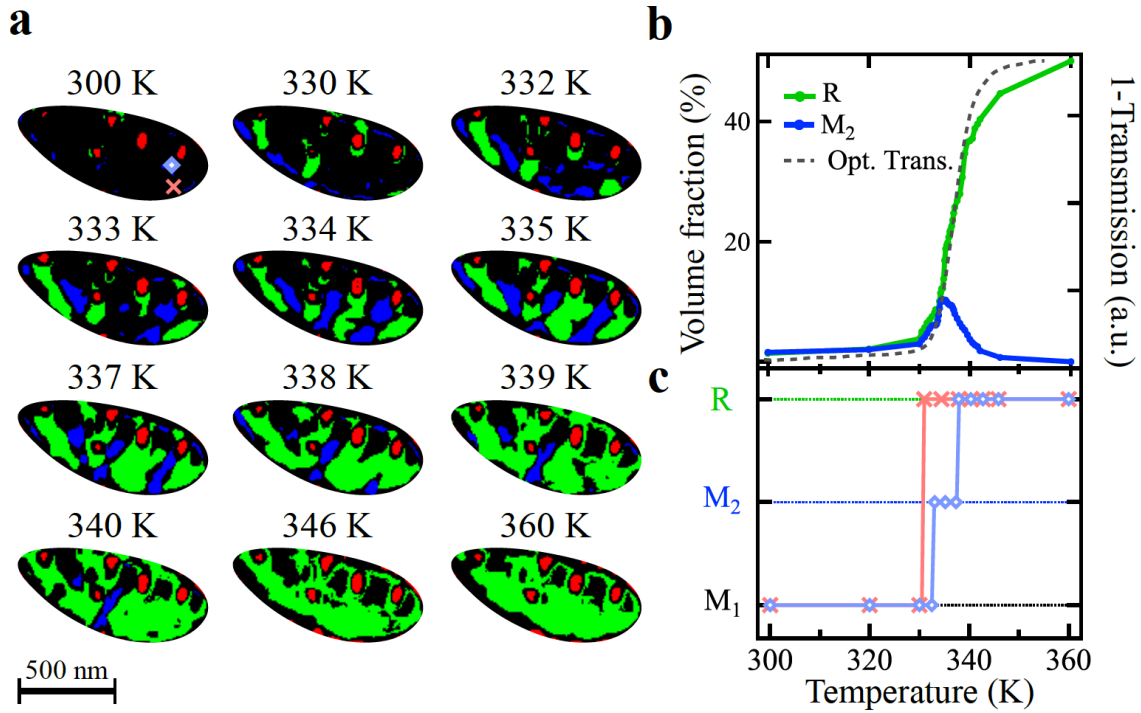


Figure 4.7. (a) Threshold images of domain growth in VO<sub>2</sub> of the single crystal outlined in Figure 4.6 at selected temperatures. Growth starts from defects (red) and consists of two phases M<sub>2</sub> (blue) and R (green). The diamond and cross markers correspond to the ROIs used in part (c). (b) Temperature dependent growth of the two phases. The volume fraction of the M<sub>2</sub> phase peaks at about 335 K before the whole sample becomes metallic. The growth of the R phase is in good agreement with the change of the optical transmission measured on a witness sample. (c) Temperature dependence of the local transition pathway of the two regions marked in (a). The area marked by a red cross transitions directly from M<sub>1</sub> to R, while the region marked by a diamond transitions via the blue M<sub>2</sub> phase.

The green,  $d_{\parallel}$  domains can be easily interpreted as the metallic R phase, that dominates at high temperatures. If changes in electronic correlations precede the structural transition, we would expect any green region to first turn blue as changes at  $d_{\parallel}^c$  should occur before those at  $d_{\parallel}$  [103]. However, we note that most regions show a direct transition from M<sub>1</sub> to R without weakening of correlations. Only in some spatially distinct regions do we

observe the intermediate blue regions. This is highlighted in Figure 4.7(c), which shows the phase as a function of temperature for two nanoscale (about 50 nm) regions of the sample. This indicates that the loss of correlations is not the driving mechanism for the insulator-metal phase transition as previously reported [103]. Instead, as strain is responsible for nucleating the phase transition, we suggest that these blue regions can be assigned to the insulating M2 phase, which is frequently observed in macroscopically strained samples. This assignment is further justified by recent calculations of the M2 phase density of states, which show anisotropic changes in the  $d_{yz}/d_{xz}$  orbitals [106], which would result in polarization sensitive changes in the XAS in the same vicinity of  $d_{||}^c$ . However, we cannot exclude that the blue regions correspond to the triclinic insulating phase and further calculations of the XAS spectral differences for these phases are needed before a conclusive assignment can be made.

These spatially resolved measurements allow us to draw a new interpretation of the phase transition in thin films. Nanoscale defects in the thin film modify the local strain environment, locally reducing the phase transition temperature for the M1-to-R transition. Due to the large volume difference of the R phase, a new strain field is generated which can also nucleate the M2 phase. Both phases continue to grow and form a striped phase due to the interaction of the strain fields. As the temperature is further raised, a complete transformation of the M2 to the R phase occurs. The temperature separation between the formation of M2 and R domains for the ROI considered is approximately 5 K, in agreement with the shift in temperature observed by Gray *et al.* [103]. This interpretation can also explain the usual temperature dependence of the XAS signal in the vicinity of  $d_{||}^c$  during a thermal cycling previously reported [107], as the M2 phase can be stabilized back to room

temperature, although the transition temperatures and growth pattern will depend on the local distribution of strain, which will be sample specific. In our measurements, the domain patterns observed were repeatable on thermal cycling, again suggesting that strain from extrinsic defects is the dominant mechanism in these samples [108]. In the future, the role of doping impurities could potentially be examined by tuning the photon energy to be resonant to the dopant ion in order to image the homogeneity of the doping process.

#### **4.7. The Potential for Similar Measurements with Femtosecond Resolution**

While the x-ray holography measurements discussed above give some insight into the nature of VO<sub>2</sub>, it must be noted that the phase transition in these experiments was driven thermally. Applying the conclusions and observations from the x-ray measurements to an all-optical modulator based upon VO<sub>2</sub> should be approached with caution. This difference between the thermal transition and the photo-induced transition is underscored by recent ultrafast measurements in which both the metallic and insulating phases of VO<sub>2</sub> were probed by extreme ultraviolet (XUV) light [40]. Jager *et al.* observed that ultrafast excitation of the insulating and the metallic phases with a NIR pump yielded a similar excited state after about 100 fs [40]. However, this excited phase was not the same as the metallic phase and it persisted for more than 60 ps. Although an all-optical modulator with a 60 ps response time would be too slow to compete with state-of-the-art devices, these XUV measurements [40] demonstrate that the thermal phase transition of VO<sub>2</sub> cannot reliably predict the ultrafast dynamics of the photo-induced transformation.

However, these x-ray holography experiments, based upon the thermally driven phase transition, do indicate the utility of Fourier transform x-ray holography for

simultaneous nanoscale imaging of the electronic and structural degrees of freedom in VO<sub>2</sub>. The success of these measurements indicate that similar experiments could be performed with a NIR pump and an x-ray probe. There are few femtosecond x-ray lasers capable of generating the necessary x-ray fluence, but the Linac Coherent Light Source (LCLS) at the SLAC National Accelerator Laboratory can achieve the needed x-ray flux. A proposal to perform this work was accepted and two separate beam-times at LCLS have been conducted, and analysis of the collected data is underway.

## CHAPTER 5

### NANOSECOND MODULATION OF VO<sub>2</sub>-ON-SILICON HYBRID DEVICES

#### 5.1. Introduction

This chapter discusses the fabrication, static characterization, and nanosecond optical modulation of hybrid VO<sub>2</sub>-silicon devices. Absorption modulators consisting of VO<sub>2</sub> patches on silicon and phase modulators comprising VO<sub>2</sub> patches on silicon ring resonators coupled to a bus waveguide show record-setting modulation of the light transmitted through the waveguides when the phase transition of the VO<sub>2</sub> is driven by a nanosecond infrared laser. A portion of the work discussed in this chapter is published in reference [109]. My contributions to this work included assisting Judson Ryckman with the nanosecond measurements, reconfiguring the setup used for nanosecond modulation for excitation by a femtosecond laser, and carrying out those femtosecond measurements.

#### 5.2. Fabrication and Description of VO<sub>2</sub>-On-Silicon Devices

To prepare the Si-VO<sub>2</sub> hybrid devices, silicon-on-insulator wafers with a 220-nm p-type Si(100) device layer and a 1 μm buried oxide layer were purchased from SOITEC, excess silicon was etched away, and VO<sub>2</sub> was deposited. Electron-beam lithography (JEOL JBX-9300-100kV) was used to pattern the reverse-image of the silicon photonic structures and the silicon device layer was created by anisotropic reactive ion etching (Oxford PlasmaLab 100) of the silicon layer with C<sub>4</sub>F<sub>8</sub>/SF<sub>6</sub>/Ar process gases. A second round of electron-beam lithography (Raith eLine) was used to open windows for the VO<sub>2</sub> patches.

After amorphous sub-stoichiometric  $\text{VO}_x$  was deposited by electron-beam vaporization of  $\text{VO}_2$  powder (100-mesh, 99.5% purity) over the entire wafer, lift-off in acetone was performed prior to final annealing. The  $\text{VO}_x$  patches were annealed in a vacuum chamber under 250 mTorr of oxygen at  $450^\circ\text{C}$  for ten minutes to form stoichiometric and polycrystalline  $\text{VO}_2$  in accordance to our prior work [110]. Note that this process temperature is within the regime required for CMOS-compatible processing ( $T \leq 450^\circ\text{C}$ ).

In Figure 5.1, a schematic (left) and scanning electron micrograph (right) are shown for each of two device geometries utilized in this work: absorption modulators (a) and phase modulators (b) discussed in more detail in the following paragraphs. Note that ‘phase’ can refer to the electromagnetic phase in the waveguide (like in the previous paragraph) or the crystallographic phase of the  $\text{VO}_2$  patch (like in the text of Figure 5.1).

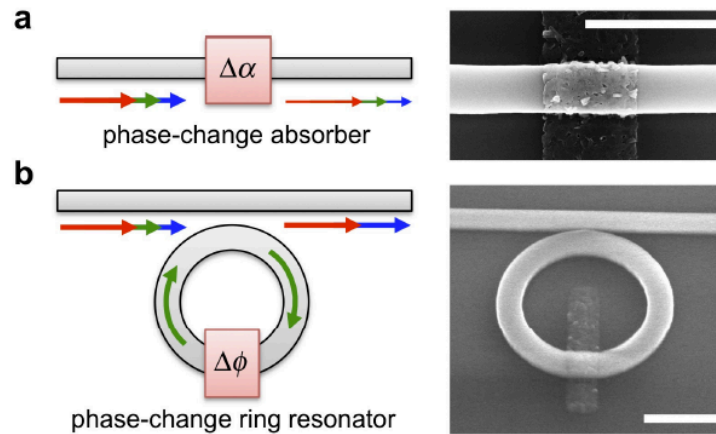


Figure 5.1. (a) Illustration of a phase-change absorber where the SMT induces a broadband change in absorption  $\Delta\alpha$ . SEM image of a typical ultra-compact Si- $\text{VO}_2$  absorber with a  $1\ \mu\text{m}$   $\text{VO}_2$  patch length. (b) Illustration of a phase-change ring resonator where the SMT induces an intracavity phase modulation  $\Delta\phi$ . Scanning electron micrograph of an ultra-compact Si- $\text{VO}_2$  micro-ring resonator with radius of  $1.5\ \mu\text{m}$  and a  $500\ \text{nm}$   $\text{VO}_2$  patch length. Scale bars in both SEM images correspond to  $1.5\ \mu\text{m}$ , approximately the probe wavelength in free space. Reprinted with permission from reference [109].

By integrating a phase-change material, VO<sub>2</sub>, onto the single-mode silicon waveguides, seen in light gray in Figure 5.1, the SMT can be harnessed to introduce a change in absorption,  $\Delta\alpha$ , of the hybrid Si-VO<sub>2</sub> waveguide mode. This non-resonant configuration capitalizes on the large contrast in the imaginary portion of the VO<sub>2</sub> refractive index,  $\Delta Im(n_{VO_2}) = Im(n_{Metal}) - Im(n_{Semi})$ , on the order of  $+2.6i$  at 1550nm [111]. The absorption of the waveguide mode can be engineered by controlling the evanescent field overlap with the VO<sub>2</sub> patch, by tuning device properties such as waveguide dimensions, patch thickness, and by tuning the VO<sub>2</sub> patch length. Near telecommunication frequencies, the optical properties of VO<sub>2</sub> are relatively constant with respect to wavelength, so device operation is broadband. However, the high optical contrast necessary to generate large modulation depths for the devices requires substantial volumes of VO<sub>2</sub> that will be detrimental to overall system performance. Since the imaginary portion of the VO<sub>2</sub> refractive index is nonzero for both phases of VO<sub>2</sub>, insertion loss for the absorption modulators will not be negligible and will increase with additional VO<sub>2</sub>.

Alternatively, the large contrast in the real part of the VO<sub>2</sub> refractive index,  $\Delta Re(n_{VO_2}) = Re(n_{Metal}) - Re(n_{Semi})$ , approximately  $-1.06$  at 1550 nm, can be used to introduce a significant change in effective index, or phase  $\Delta\phi$ . When placed inside an optical cavity, such as an ultra-compact micro-ring resonator ( $R = 1.5 \mu\text{m}$ , Figure 5.1(b)), a short 500 nm-long patch is sufficient to promote large changes in resonant wavelength without significantly affecting Q-factor [30]. In principle, this configuration could serve as a wavelength-selective reconfigurable filter or modulator, or combined with a drop port for use as a router. With longer patch lengths, intracavity absorption modulation could also effectively extinguish resonances [112]. However, given the disadvantages of this approach in realistic device

structures, resonant frequency modulation is emphasized below.

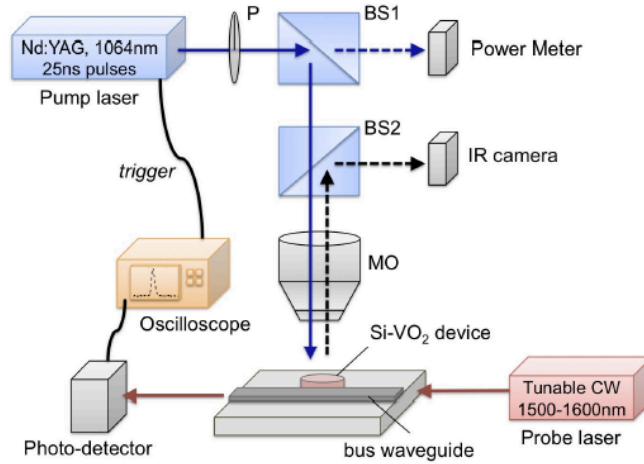


Figure 5.2. Schematic of the experimental pump-probe configuration utilized in this work. Tunable probe laser transmission is monitored with a photo-detector and oscilloscope, while nanosecond-pulsed pump light is delivered to the device through a microscope objective (MO) and two beam-splitters (B1 and B2) with power controlled by a linear polarizer (P). Reprinted with permission from reference [109].

### 5.3. Nanosecond All-Optical Modulation Setup Description

Figure 5.2 illustrates the measurement scheme used to measure the nanosecond response of the VO<sub>2</sub>-on-silicon devices. Continuous-wave (cw, not pulsed) probe light from a tunable infrared laser (Santec TSL-510) was coupled into and out of millimeter-length bus waveguides using polarization maintaining lensed fibers (OZ Optics). Each lensed fiber was mounted on piezo-controlled XYZ stages to aid alignment to the bus waveguides with end facets with cross sections less than five square microns. Detection of the probe light transmitted through the waveguide devices was performed using a fiber coupled avalanche photodiode photoreceiver (Newport 1647), with differential outputs monitored by an oscilloscope (Tektronix TDS 2024C). The oscilloscope was triggered directly from the

nanosecond pump laser, which consisted of a Q-switched Nd:YAG laser operating at 1064 nm with a 10 Hz repetition rate (Continuum Minilite). The pump intensity was controlled by a polarizer (P) and delivered to the sample through two beamsplitters (BS1 and BS2) and a Mitutoyo near-infrared, apochromatic, infinity-corrected, long-working-distance, 5x microscope objective (MO). A power meter (Newport 2936 C) and IR camera (Sensors Unlimited 320M) facilitated the calibration and measurement of the pump fluence and positioning of the pump beam spot onto the device to be measured.

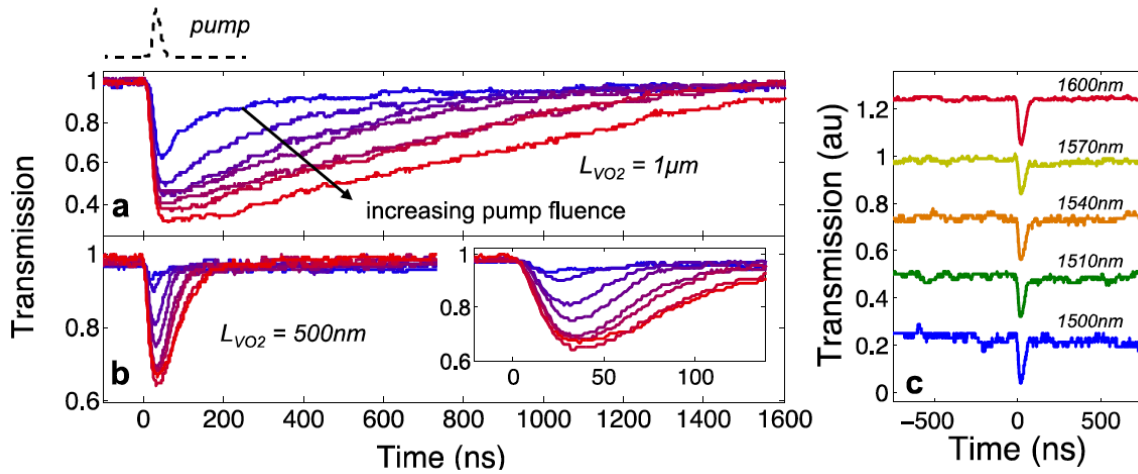


Figure 5.3. Normalized probe transmission through Si-VO<sub>2</sub> absorption modulators with (a) 1000 nm and (b) 500 nm VO<sub>2</sub> patch lengths. The pump fluence is incrementally increased in the range 0.5 to 8 mJ/cm<sup>2</sup>. The pump pulse is shown above (a) on the same timescale for comparison. (c) Transmission through a 500-nm VO<sub>2</sub> device for probe wavelengths between 1500 and 1600 nm, demonstrating broadband modulation. The pump fluence was ~5 mJ/cm<sup>2</sup>, above the threshold fluence. Transmission plots are vertically offset by 0.25 a.u. for clarity. Reprinted with permission from reference [109].

#### 5.4. Nanosecond Characterization of All-Optical Absorption Modulator

Figure 5.3(a) shows the time-dependent optical transmission of the Si-VO<sub>2</sub> absorption modulators, similar to the devices depicted in Figure 5.1(a), for varying pump fluence and patch lengths of 1000 nm and 500 nm. Both devices exhibit an abrupt reduction in optical transmission consistent with the time scale of the pump pulse (FWHM of about 25ns) which is shown by the black dashed line above Figure 5.3(a) on the same time scale. This tracking of the pump pulse aligns with reports using 10<sup>-8</sup> to 10<sup>-14</sup> second laser pulses to optically trigger the SMT in VO<sub>2</sub> thin films [39]. For both absorption modulators devices, designated as absorber1 (1000 nm) and absorber2 (500 nm), the modulation depth increases approximately linearly with pump intensity and saturates near a threshold fluence of 1.27 mJ/cm<sup>2</sup> in Figure 5.4(a). This saturation is indicative of a completed SMT occurring throughout the VO<sub>2</sub> patch and is a hallmark of the SPT [113]. The observed threshold of about 1.27 mJ/cm<sup>2</sup> is comparable to other reports spanning both nanosecond and femtosecond measurements [42,46]. At threshold, we estimate the modulation depth of the Si-VO<sub>2</sub> absorption modulators to be 4±0.3 dB/μm, which is approximately 40 times larger than monolayer graphene-on-silicon absorbers [114] (about 0.1 dB/μm) and more than three orders of magnitude larger than silicon-based two-photon cross-absorption modulation (about 0.001 dB/μm) [115]. The insertion loss of the 1000-nm Si-VO<sub>2</sub> device was within fiber-to-chip coupling variations, between about 0.5 and 2 dB. Broadband device operation was verified from 1500 to 1600 nm, as shown in Figure 5.3(b) and in agreement with the relatively constant complex refractive index of VO<sub>2</sub> over this spectral range [33].

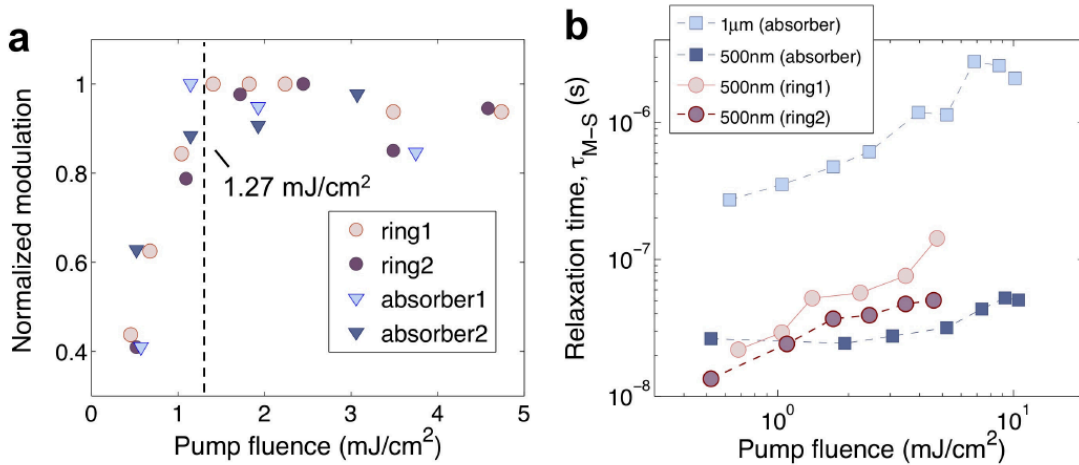


Figure 5.4. (a) Transmission modulation saturates for all devices beyond a fluence of  $\sim 1.27 \text{ mJ/cm}^2$ . (b) Time required for the  $\text{VO}_2$  in the devices to return to the initial insulating phase from the metallic state as a function of fluence. Reprinted with permission from reference [109].

The SMT is limited by the duration of the nanosecond laser pulse for all fluences while the reverse transition is only limited by the pulse at lower fluences, as seen in Figure 5.3(b). However, the reverse transition to the semiconducting phase of  $\text{VO}_2$  can be significantly slower than the SMT and depend strongly on both pump fluence and  $\text{VO}_2$  patch length, demonstrated with a comparison of Figure 5.3(a) and 5.3(b). The photo-induced SMT is an abrupt and potentially ultrafast athermal process, driven by photo-generation of electron-hole pairs and an electronically-controlled lattice transformation into the higher symmetry rutile structure [46,116]. The ensuing thermalization transiently increases the internal temperature of the  $\text{VO}_2$  patch [39], so undoing the SPT is a thermally mediated relaxation process dependent on thermal diffusion and nucleation of the monoclinic phase [113,117]. As discussed later, faster device relaxation might be achieved by pumping below the threshold fluence to drive the electronic SMT without causing a complete SPT. As shown in Figure 5.4(b) or by comparing Figure 5.3(a) to 5.3(b), simply changing the patch length

of VO<sub>2</sub> on the waveguides to sub-micron dimensions, from 1 μm to 500 nm, reduces the relaxation decay time  $\tau_{M-S}$  by approximately one order of magnitude. All Si-VO<sub>2</sub> hybrid ring resonators discussed in the next section utilize the shorter 500 nm VO<sub>2</sub> patch length and show similarly reduced relaxation times.

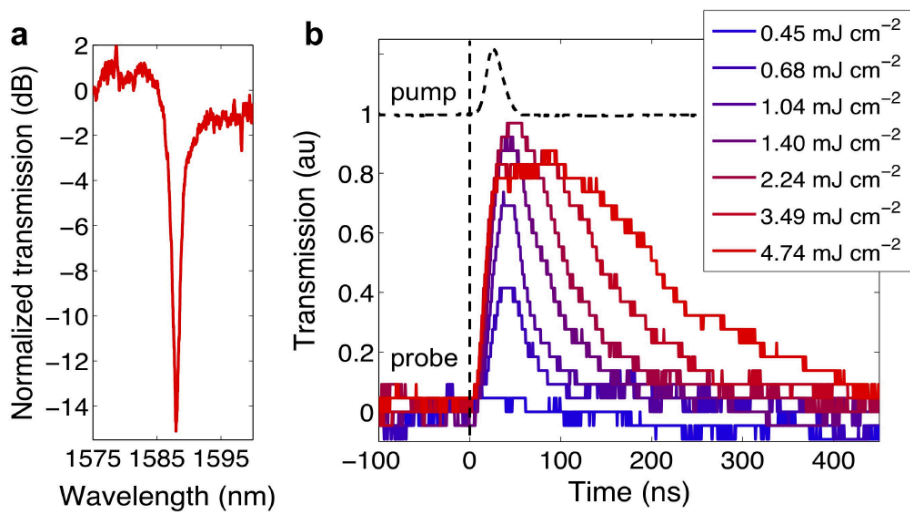


Figure 5.5. (a) Typical transmission spectrum for 1.5 μm VO<sub>2</sub>-Si ring resonator. (b) Corresponding time-dependent device transmission for a ring resonator with a 1.5 μm radius with the probe wavelength tuned to the ring resonance at 1588.5 nm. The time-signature of the pump is shown for comparison. Reprinted with permission from reference [109].

### 5.5. Nanosecond Characterization of All-Optical Phase Modulator

In addition to the Si-VO<sub>2</sub> absorption modulators, we also tested Si-VO<sub>2</sub> hybrid micro-ring resonators, like the one shown in Figure 5.1(b). The transmission spectra in Figure 5.5(a) is for an ultra-compact device with a radius of 1.5 μm and a VO<sub>2</sub> patch coating a portion of the ring waveguide. The patch extends about 500 nm along the length of waveguide it is about 70 nm thick. As a result of the small ring radius, the device shows a modest Q-factor of about 10<sup>3</sup>, corresponding to an optical bandwidth exceeding 100 GHz. The time-dependent

optical transmission for the pump-probe experiment is shown in Figure 5.5(b) for a variety of pump fluences, where the probe wavelength of the cw light is tuned to match the resonance minimum at 1588.5 nm. Photo-inducing the SMT causes an abrupt increase in transmission, estimated in this case to peak at about 7.2 dB, followed by a slower relaxation to the low initial value. The observed modulation contrast for the 1588.5 nm probe light is several times larger than what can be achieved for the absorption modulator with the same active VO<sub>2</sub> area. For this device, with bandwidth greater than 0.8 nm, the large increase in transmission suggests that the resonance wavelength is significantly modified by the photo-induced SMT. This is in stark contrast to conventional silicon-only ring resonators, where relatively weak electro-optic or nonlinear effects necessitate the use of high Q-factor resonators, with less than 0.05 nm bandwidth, to observe significant modulation [118].

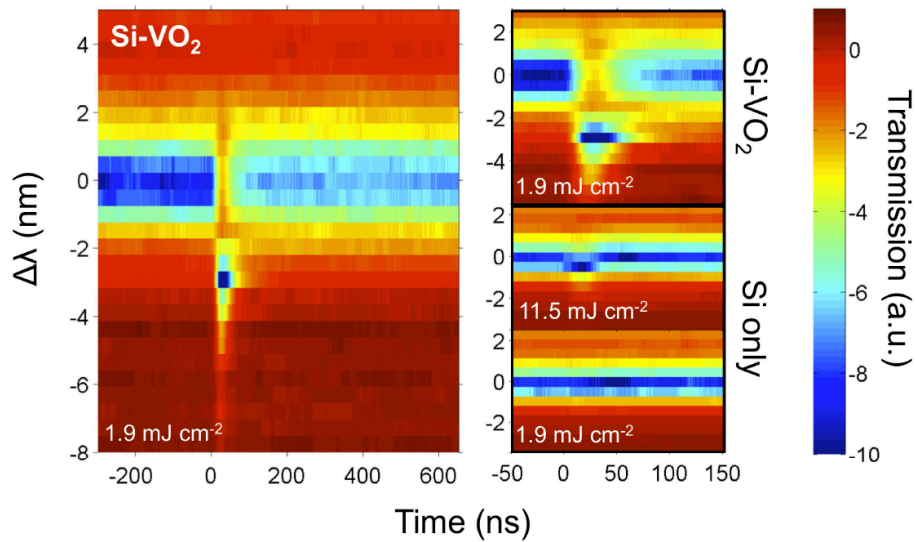


Figure 5.6. At the left is a time-dependent spectrum for a ring resonator of radius 1.5  $\mu\text{m}$  slightly above the threshold fluence at 1.9  $\text{mJ}/\text{cm}^2$ . On the right-hand side, a zoomed-in spectrum for the VO<sub>2</sub>-Si hybrid device is compared to the transmission from a silicon-only device. At 1.9  $\text{mJ}/\text{cm}^2$ , the silicon-only device has a negligible modulation and a fluence of 11.5  $\text{mJ}/\text{cm}^2$  is required to detect even a small modulation. Reprinted with permission from reference [109].

To confirm this larger resonance shift, the time-dependent spectrum of this Si-VO<sub>2</sub> hybrid ring resonator of radius 1.5 μm is needed. Measurements similar to each of those in Figure 5.3(a,b) were performed at varying probe wavelengths. The result is shown in Figure 5.6 and further analyzed in Figure 5.7(a). For this measurement, the device is pumped at 1.9 mJ/cm<sup>2</sup>, above the threshold required to complete the SMT by forming the rutile crystalline phase in VO<sub>2</sub>. The rapid shift in resonant wavelength of about -3.07 nm, seen in Figure 5.7(a), was extracted by fitting the data to a Lorentzian line shape. The same measurement, at the same fluence, performed on a control silicon-only resonator reveals a wavelength shift of -0.057 nm, nearly sixty times smaller (Figure 5.6, right-bottom). Even at when pumped at 11.5 mJ/cm<sup>2</sup>, the resonance shift was measured to be only -0.325 nm, as shown in the right-middle plot of Figure 5.6. This is unsurprising, since the resonance shift of the Si-VO<sub>2</sub> hybrid device arises from the substantial modification of VO<sub>2</sub> refractive index,  $\Delta Re(n_{VO_2}) = -1.06$ , and the resonance shift of the control device is dependent upon the silicon refractive index modulation due to the change in free-carrier concentration, estimated in this case to change by  $\Delta Re(n_{Si}) = -1.6 \times 10^{-4}$ . At the higher fluence of 11.5 mJ/cm<sup>2</sup>, phonon excitations in the silicon lattice produce a residual thermo-optic redshift as high as +0.13 nm in addition to the free-carrier effect, visible in Figure 5.7(a) beyond about 30 ns. This corresponds to a transient temperature increase of the silicon waveguide less than 2°C [119]. No such effect is observed at 1.9 mJ/cm<sup>2</sup> fluence, indicating that the silicon waveguide temperature is not affected by the pump pulse near, but just above, threshold. With a negligible thermo-optic contribution of the silicon waveguide at the low pump fluence, the optical response of the Si-VO<sub>2</sub> device is entirely controlled by the SMT in the VO<sub>2</sub> patch. This maximizes the achievable optical response, since the SMT in VO<sub>2</sub> and the thermo-optic

effect in silicon generally provide opposing contributions to refractive index. Furthermore, the timescale for device operation is dictated solely by the switching time of the VO<sub>2</sub>.

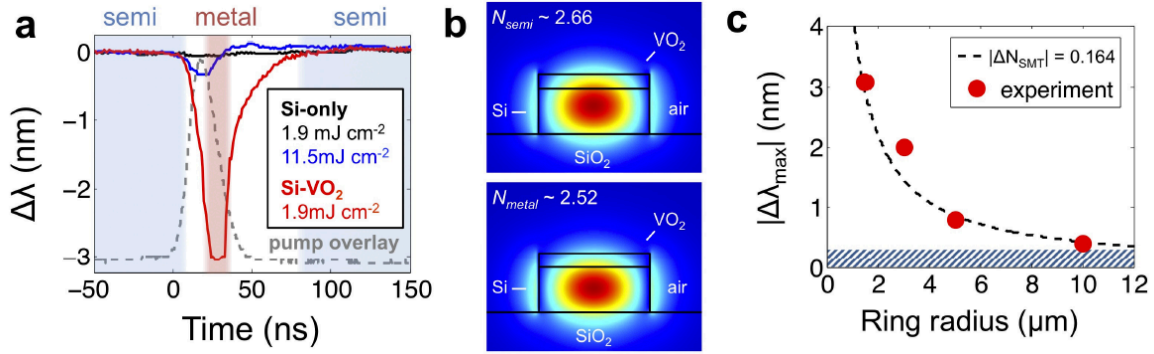


Figure 5.7. Analysis of phase modulation of Si-VO<sub>2</sub> micro-ring resonator configuration. (a) Resonant wavelength as a function of time, extracted from the time-dependent spectra found in Figure 5.6. The pump signal is above (a) for comparison purposes. (b) FDTD mode simulation for a hybrid Si-VO<sub>2</sub> waveguide. In semiconductor phase (top), more of the mode passes through the VO<sub>2</sub> than in the metallic state (bottom). Silicon waveguide dimensions are 220 x 500 nm with a 70 nm thick VO<sub>2</sub> patch on top. (c) Magnitude of resonance blue-shift as a function of ring radius for Si-VO<sub>2</sub> micro-ring resonators with a fixed 500 nm VO<sub>2</sub> patch length. Dashed line is fit with  $R^{-1}$ , while the shaded region indicates the regime where resonance change is less than 0.3 nm. Reprinted with permission from reference [109].

As shown in Figure 5.7(a), the SMT-induced resonance shift and the SPT are completed in about 30 ns. At threshold, this timescale is primarily controlled by the pump pulse. Based on the reported response times of VO<sub>2</sub> thin films optically excited by shorter pulses [21,39,116], it should be possible to extend device operation to ultrafast all-optical modulation with a switch-on time of about 26 fs [40]. Although the reverse SMT to its higher-index semiconducting phase takes over 50 ns, this relaxation time scale is not intrinsic to the phase-transition of VO<sub>2</sub> and can be controlled by a variety of factors. If the full SPT is driven,

possibilities for improving the return time could include a more sophisticated thermal design, such as reducing the VO<sub>2</sub> thickness, depositing a top-cladding, or tailoring the SOI substrate geometry. Alternatively, THz conductivity experiments indicate lattice-relaxation times of less than 3 ps are possible when the fluence for ultrafast pump pulses (15 fs) is below the threshold to drive the SPT [120]. In this low-fluence regime, it is hypothesized that photo-generated carriers may excite the electronic transition and rapidly decay through a fast trapping or other relaxation pathways without driving a complete SPT. There is additional evidence for the existence of a monoclinic metallic phase after ultrafast excitation of VO<sub>2</sub> that suggests fast relaxation of the metallic phase is possible [38,43,117]. Rapidly sweeping out photo-generated carriers with a voltage bias may be another via option to increase modulation speed [121]. Thus, there are several strategies through which Si-VO<sub>2</sub> hybrids could be a practical platform for ultrafast all-optical devices.

The observed resonance shift of more than 3 nm for the Si-VO<sub>2</sub> hybrid ring resonator is achieved with a small active area (0.275 μm<sup>2</sup>) of 70 nm thick VO<sub>2</sub>, corresponding to a 5.3% coverage of the micro-ring. By controlling the surface coverage, VO<sub>2</sub> thickness, or modal overlap with the VO<sub>2</sub> patch, the resonant change induced by the SMT could be tuned and optimized. For a hybrid Si-VO<sub>2</sub> waveguide, with silicon dimensions of 220 nm by 500 nm and a 70 nm thick VO<sub>2</sub> layer, the SMT is expected to produce a large change in the effective index of the hybrid waveguide,  $\Delta N_{\text{hybrid}}$ , of about -0.14, as indicated by finite difference time domain (FDTD) modal simulations shown in Figure 5.7(b). To demonstrate that adjusting the fractional coverage of the ring can probe large and highly tunable effects, variable-wavelength pump probe measurements were performed on devices with the same 0.275 μm<sup>2</sup> VO<sub>2</sub> patch area but ring radii,  $R$ , ranging from 1.5 to 10 μm. As shown in Figure

5.7(c), the magnitude of the resonant response,  $|\Delta\lambda_{\max}|$ , follows an  $R^{-1}$  dependence. This agrees with calculations where the average effective index change in the ring resonator,  $\Delta N_{avg}$ , can be modeled as:

$$(5.1) \quad \Delta N_{avg} = \frac{\Delta N_{hybrid} \cdot L_{VO_2}}{2\pi R}$$

Using a fit based upon the  $R^{-1}$  dependence, shown as a dashed line in Figure 5.7(c), and the assumption that  $\Delta\lambda_{\max}/\lambda_0 = \Delta N_{avg}/N_g$ , we estimate  $\Delta N_{hybrid}$  to be  $-0.164 \pm 0.033$ , where  $N_g$  is the group index of the ring waveguide ( $\sim 4.4$ ) and  $\lambda_0$  is the initial resonant wavelength. The experimental  $\Delta N_{hybrid}$  is within the experimental error of the value found with FDTD simulations. The intracavity phase modulation  $\Delta\phi_{SMT} / L_{VO_2} = 2\pi/\lambda_0 \Delta N_{SMT}$  induced by the SMT is then about  $\pi/5$  rad/ $\mu\text{m}$ , while that of the silicon-only device is estimated to be three orders of magnitude lower, about  $\pi/5000$  rad/ $\mu\text{m}$ . This large difference in the modulated phase is the reason that such a small ( $\sim 0.275 \mu\text{m}^2$ ) active area of  $\text{VO}_2$  can provide  $\sim 60$  times larger resonance shift than the silicon-only device.

One important advantage of a large resonant response is that ambient effects, such as thermal fluctuations, are minimized. The shaded gray region in Figure 5.7(c) covers for which the resonance shift is less than 0.3 nm corresponds to a temperature tolerance of  $\pm 3^\circ\text{C}$  for silicon resonators with a typical thermo-optic sensitivity of about  $0.1 \text{ nm}/^\circ\text{C}$ . This region also corresponds to roughly two linewidths for a cavity with Q-factors of about  $10^4$  so devices that operate in this regime are highly susceptible to noise or error. Furthermore, the longer cavity lifetime of these high-Q resonators also limits their modulation speed. By providing larger enhancements for larger fractional  $\text{VO}_2$  surface coverage, the Si- $\text{VO}_2$  platform further favors ultra-compact device geometries.

In conclusion, all-optical operation of Si- $\text{VO}_2$  broadband absorption modulators

consisting of patches of VO<sub>2</sub> on silicon waveguide yielded record values of modulation ( $\sim 4$  dB/ $\mu\text{m}$ ) upon excitation with a nanosecond laser pulse. Phase modulators were realized by depositing VO<sub>2</sub> patches on silicon ring resonators. These resonant devices exhibit large bandwidth, reduced ambient sensitivity, ultra-compact geometries, and record-setting intracavity phase modulation ( $\sim \pi/5$  rad/ $\mu\text{m}$ ). Given the ability to optically trigger the SMT in less about 25 fs and evidence for a switching time below 3 ps if the full SPT can be avoided, the hybrid Si-VO<sub>2</sub> platform could lead to a new class of ultrafast photonic devices.

### **5.6. All-Optical Phase Modulation After Femtosecond Excitation**

To characterize the temporal response of the devices after femtosecond irradiation, an optical setup, diagrammed in Figure 5.8, was built that allows the devices to be pumped from above (out-of-plane) while a tunable cw-probe beam propagates along the bus waveguide of the device. A titanium-sapphire oscillator (Spectra-Physics Mai Tai SP) seeded a Ti:sapphire amplifier (Spectra-Physics Spitfire Ace) which in turn pumped an optical parametric amplifier (Light Conversion TOPAS) at 1 kHz to yield signal and idler beams. The signal beam at 1550 nm was used as the pump beam for these experiments, while the idler beam (1670 nm) was removed from the OPA output beam with a polarizing beamsplitter. The bandwidth of the signal beam was measured to be about 40 nm, which is consistent with the manufacturer specifications and pulse durations of less than 200 fs; those measurements are discussed further in Chapter 6. A silver-coated parabolic mirror (focal length of 2 inches) was used to focus the beam before the sample, so that the sample was placed beyond the focus. The purpose of this choice was two-fold. First, the large beam spot ( $\sim 100$   $\mu\text{m}$ ) kept the beam from drifting off the devices. Second, with the 1 kHz repetition

rate, the average pump beam power necessary to switch the VO<sub>2</sub> at the focus was below the noise floor of the power meter, but measurable with the de-focused beam spot. The power meter was on a flip mount right before the parabolic mirror (not shown in Figure 5.8).

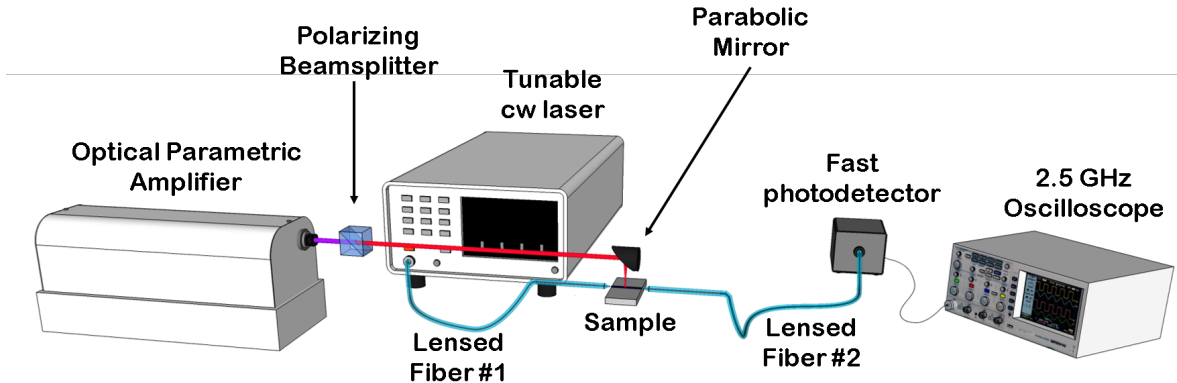


Figure 5.8. Out-of-plane pump, in-waveguide cw-probe setup. The probe laser can be tuned independently from the fs-pump laser with 0.001 nm resolution. The polarizing beamsplitter removes the idler beam, and the remaining light (signal beam) at 1550 nm is focused onto the devices at normal incidence with the parabolic mirror. Although the pulse length is less than 200 fs, the time resolution of this setup is limited by the oscilloscope and the detector.

A tunable cw laser (Santec TSL-510) with a wavelength tunable from 1500 to 1630 nm was used as the probe beam, and a lensed fiber focused the beam down to a spot of about 3  $\mu\text{m}$  on the end-facet of the silicon waveguide. Another lensed fiber collected the output and delivered it to a fast photodiode detector (Newport 1647) and a fast oscilloscope (Tektronix DPO7254C; 2.5 GHz bandwidth).

The device shown in Figure 5.9(a,b) was characterized using the out-of-plane pump, in-waveguide cw-probe setup. The VO<sub>2</sub> patch on the device is 550 nm wide (same as the silicon waveguide) and 500 nm long and about 80 nm thick. Typical responses when only the pump is unblocked (black) and both the probe and pump are unblocked (red) are shown

in Figure 5.9(c). By subtracting the former from the latter, the response of the probe to the pump is obtained; it is shown in gold in Figure 5.9(c).

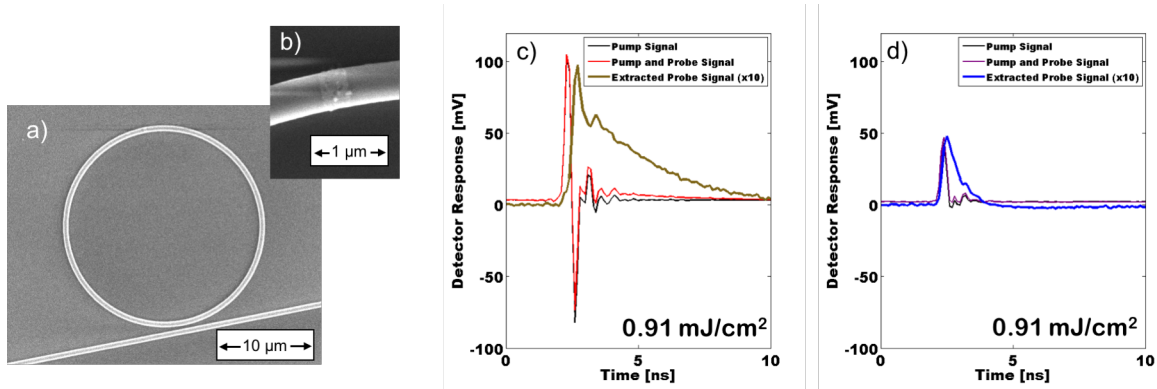


Figure 5.9. (a) SEM image of typical device with 550x500x80 nm patch of VO<sub>2</sub> and (b) enlarged image of VO<sub>2</sub> patch. (c,d) Typical probe signal (gold, blue) extracted from the pump-and-probe signal (red, purple) and the pump-only signal (black, black). The extracted signal is magnified by a factor of 10 for clarity.

By varying the probe wavelength using a tunable cw laser and holding the pump fluence constant, the time-dependent spectral response of the devices was obtained as in Figure 5.10. The probe wavelength was varied over the measured bandwidth of the ring resonator. Comparing similar time-dependent spectral responses for the VO<sub>2</sub>-device in Figure 5.10(a) and Si-only device in Figure 5.10(b) one can see that the resonance shifts are significantly larger for the VO<sub>2</sub> device. Furthermore, the bandwidth of the hybrid ring resonator is larger (~1 nm) than that of the Si-only device (~0.6 nm), as expected due to the decrease in Q-factor caused by the presence of the VO<sub>2</sub>. Unlike similar experiments [109] with nanosecond laser pulses, both the Si-only and the VO<sub>2</sub> devices show a blueshift after excitation. Because the net redshift in the nanosecond experiments was attributable to the thermo-optic effect in the silicon, this suggests that the thermo-optic effect can be neglected for femtosecond excitation. The lack of thermo-optic signal is consistent with the fact that

the energy of the pump pulse is deposited on a time scale that is much faster than the thermal diffusivity.

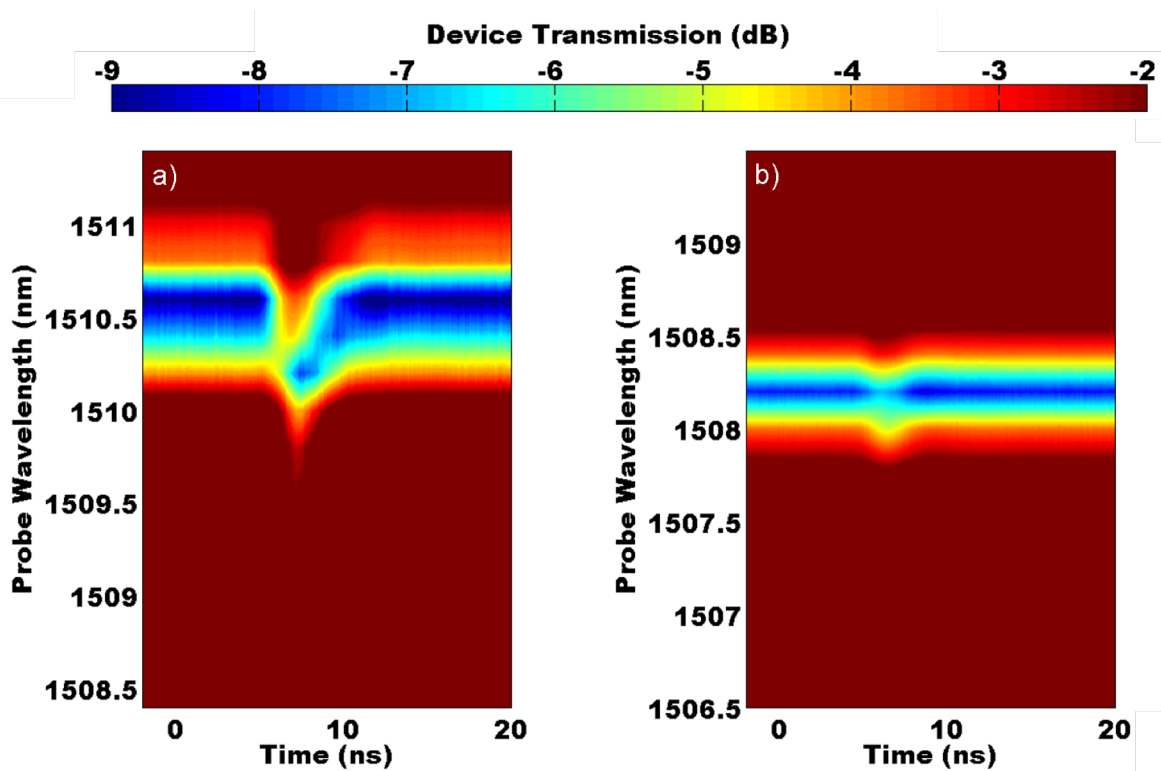


Figure 5.10. Time-dependent spectra for the (a) VO<sub>2</sub>-Si device at  $\sim 0.6$  mJ/cm<sup>2</sup> and the (b) Si-only device at  $\sim 0.9$  mJ/cm<sup>2</sup>.

In order to compare the magnitude of the VO<sub>2</sub> and the Si-only devices, the probe wavelength was held constant and the pump laser fluence was adjusted with a pair of polarizers. Probe wavelengths slightly blueshifted (0.1 nm) from the resonance were chosen to maximize each device response. A few time-spectra taken during the fluence sweeps for the hybrid and Si-only devices are shown in Figure 5.11(a). The fluences (in mJ/cm<sup>2</sup>) are listed on the left of each pair (VO<sub>2</sub> in gold and Si-only in blue) of the time plots. Note that the y-scale was decreased with decreasing fluence, as noted by the multipliers on the right. However, the Si-only and VO<sub>2</sub> plots for a given fluence are plotted on the same scale, which

makes it obvious that the response of the VO<sub>2</sub> device is larger than that of the Si-only device for any fluence.

Above 0.24 mJ/cm<sup>2</sup>, the transient responses in both the hybrid and Si-only devices are positive, with a long relaxation time that is typical of thermal relaxation processes. The transient response of the hybrid device is larger than that of the Si-only device in both cases (Figure 5.11) consistent with a larger absorbed fraction of the pump light. The increase in transmission in this fluence regime is similar to what was previously observed for nanosecond pumping at 1.06 μm wavelength, substantially above the band edge of the VO<sub>2</sub>. The long relaxation time is consistent with substantial (but not complete) metallization of the VO<sub>2</sub> patch, as previously seen in nanosecond switching of similar ring resonators [109]. Right at 0.24 mJ/cm<sup>2</sup>, it appears that the behavior of the ring-waveguide system is switching from one regime to the other.

In Figure 5.11(b), the maximum (or minimum) device responsivities are plotted with respect to the incident fluence as circles (or triangles). The responsivities for the hybrid VO<sub>2</sub> devices are only about a factor of two larger than the silicon-only devices above the threshold fluence. However, below the threshold fluence, the VO<sub>2</sub>-enhanced devices exhibit about 10 dB higher responsivities than the silicon-only ones, until the noise floor of the measurements at about 0.03 mV/W. For 175-fs pulses (see section 6.3.1) like the ones used in these experiments, the appearance of a signal at between 0.15 and 0.20 mJ/cm<sup>2</sup> is in excellent agreement with commonly accepted value of the onset for two-photon absorption in silicon, 1 GW/cm<sup>2</sup> [122]. Note that the threshold fluence of 0.24 mJ/cm<sup>2</sup> for the VO<sub>2</sub>-device is consistent with the onset of a measurable signal in the nanosecond-pumped experiments in Section 5.5 and Rini *et. al* [123]. At this fluence, the VO<sub>2</sub> is probably in the very short-lived

monoclinic metallic phase identified by several experiments [41,44–46].

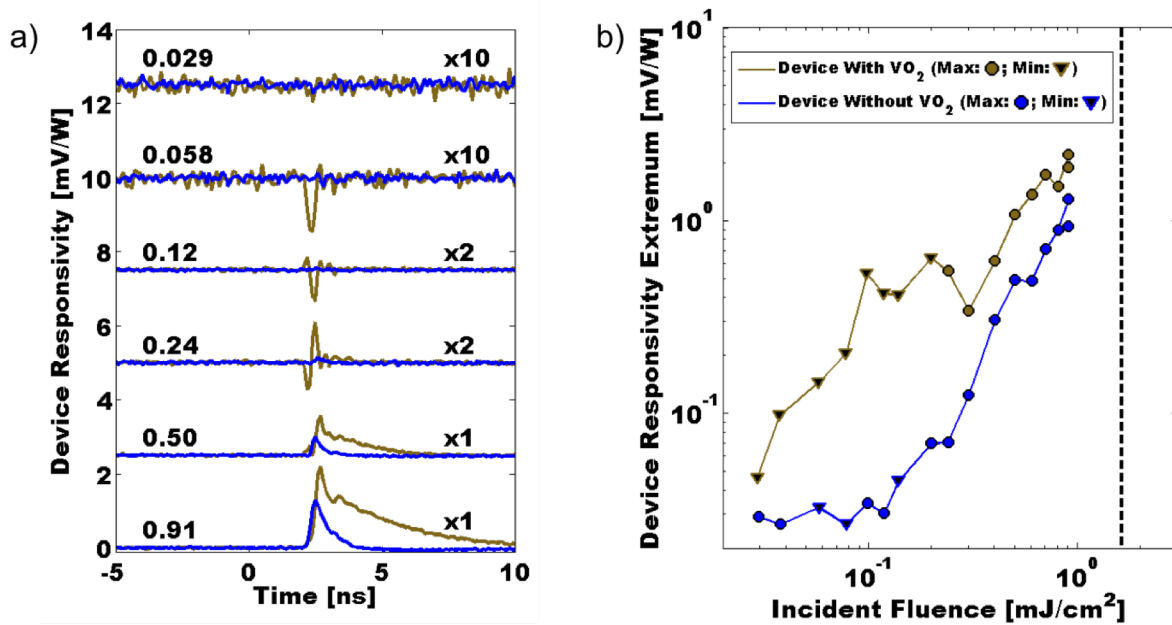


Figure 5.11. (a) Comparison of extracted probe signals from a silicon-only device (blue) and a VO<sub>2</sub> device (gold) at various fluences. The smaller signals at lower fluences were multiplied by the factors listed at the right, and the fluences are listed in units of mJ/cm<sup>2</sup> at the left. (b) Device responsivity extrema for modulators with VO<sub>2</sub> show enhanced modulation. The probe wavelength was 0.1 nm above the resonance wavelength for all measurements.

Note that below 0.24 mJ/cm<sup>2</sup>, the detector response is negative, indicating that the power transmitted through the waveguide is diminished. Since the probe for these measurements is basically on-resonance, we would expect an increase in probe transmission, like we see at the higher fluences. This surprising result was explored further in Figure 5.12. When the pump is above the threshold fluence and the probe wavelength is far above, slightly above, and below the resonance wavelength, a small positive, large positive, and large negative response, respectively, as expected and as can be seen in Figure 5.12(a). However, when the pump is below the threshold fluence, the device shows a negative response for all

three wavelengths.

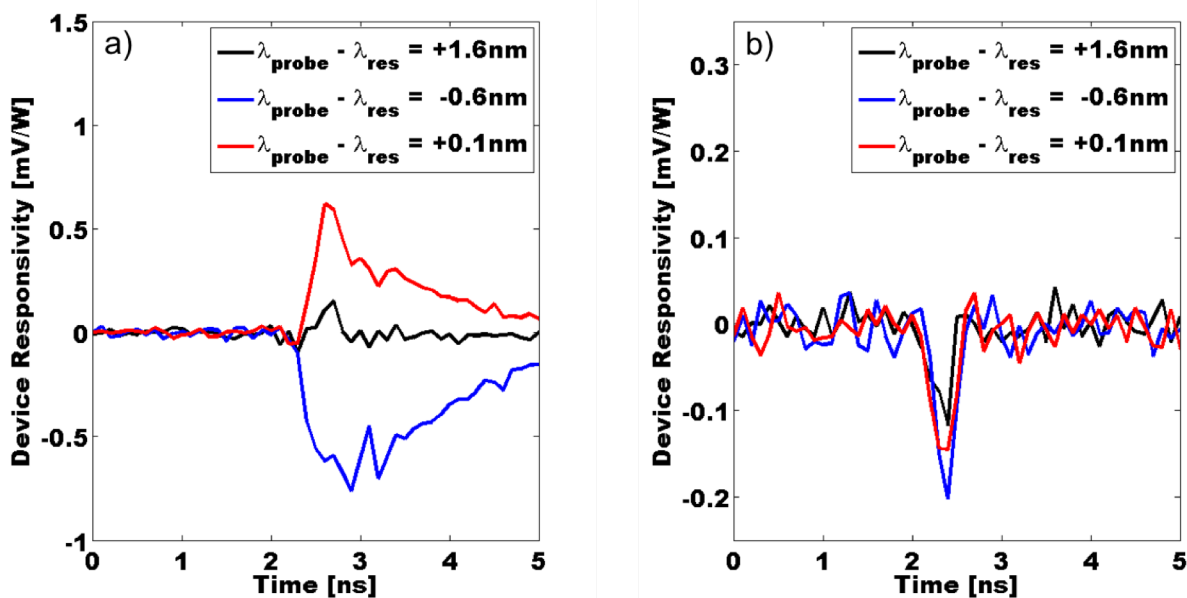


Figure 5.12. (a) Above the device threshold, device responsivities when the probe wavelength is far from (black), shorter than (blue), and longer than (red) the resonance wavelength are zero, negative, and positive, as expected. (b) Below threshold, all responses are negative and of a similar magnitude. For all three measurements, the pump fluence was (a) 0.40 mJ/cm<sup>2</sup> (b) 0.058 mJ/cm<sup>2</sup>.

At this time it is unclear why the signal is always negative below the threshold pump fluence, but the effect is not observed in the Si-only control sample as seen in Figure 5.11(a). This consistently negative response would suggest that the VO<sub>2</sub>-silicon ring system causes a decrease in probe transmission through the bus waveguide that is slightly larger near the resonance (blue and red) than further from it (black). This puzzling result is inconsistent with the shift of the resonance from one wavelength to another, despite the ability of that resonance shift to explain the observations from the nanosecond experiments and these femtosecond measurements when above the threshold fluence of 0.24 mJ/cm<sup>2</sup>. If the resonance were to be destroyed, rather than simply shifted, one would expect a larger

transmission through the bus wavelength when the cw probe is set to the resonance wavelength. The constant negative result in Figure 5.12(b) would suggest that the VO<sub>2</sub>-ring system is suddenly lossy at all wavelengths traversing the bus waveguide and only slightly more absorptive, less than a factor of two, on resonance than far from it (+1.6 nm).

Despite these unexplained results, two conclusions are clear. First, the VO<sub>2</sub>-based device has a time response limited by the resolution of the detector, which is about 250 ps. This result bodes well for the prospect of all-optical modulation in VO<sub>2</sub>-based devices, and drove the development of a measurement system with a faster response time, as will be discussed in the next.

The second item to keep in mind is that these measurements involving the femtosecond excitation of VO<sub>2</sub> should not be expected to track too closely with the nanosecond results. Although the exact mechanism of the photo-induced and thermally driven phase changes have been thoroughly debated, it is widely accepted that the two mechanisms are not equivalent. The origin of the thermal transition from the M1 to R phase has been discussed for decades, the debate has largely centered on whether the Peierls or Mott interpretation is a better model for the transition. Although the debate has probably not concluded, most researchers have come to agree the thermal phase transition involves a complex interplay between the Mott and Peierls effects, as discussed more thoroughly in Chapter 3 and references [50–67]. The ultrafast transition is similarly complicated, but the debate focuses on the relationship between two critical threshold densities: one of carriers and one of 6-THz phonons. The photoinduced involves both 1) interband transitions which generates free carriers and cause an orbital reconfiguration and 2) a catastrophic collapse of the oxygen-cage vibration with a frequency of about 6 THz [38,39,44–46,113,116,120,124].

Furthermore, wavelength dependent ultrafast measurements have more explicitly shown that the threshold energy density necessary for the ultrafast structural transition is incongruous with the thermal transition as discussed more thoroughly in Chapter 1 [37].

## CHAPTER 6

### ULTRAFAST MODULATION OF EMBEDDED VO<sub>2</sub>-SILICON WAVEGUIDE HYBRID DEVICES

#### 6.1. Introduction

In the last chapter, a resonant VO<sub>2</sub>-on-silicon device demonstrated a detector-limited signal with a FWHM of about 500 ps. However, the negative polarity of the low pump-fluence signal did not seem at the time to be consistent with expectations or results on the same device at higher pump fluences. An ultrafast pump-probe experiment would enable characterization of this fast response. In this chapter, such a setup is built but with the probe beam confined in a waveguide.

Typically, a control sample, or standard with a large signal facilitates alignment and data acquisition before the test sample is characterized by a pump-probe measurement. However, for an in-waveguide probe, it was difficult to conceive of a relevant control or calibration device. Therefore the device used in the first measurements with this out-of-plane pump, in-waveguide probe setup was carefully chosen, and the rationale for the choice was twofold. First, spectrally resolving a signal results in a lower signal-to-noise ratio since the signal is divided by the number of channels in the detector. Combined with the wavelength-dependent uncertainties associated with the hybrid ring resonator device outlined at the end of the last chapter and the fact that an ultrafast pulse necessarily has a finite bandwidth, a non-resonant device was chosen. Second, the device geometry was chosen to maximize the device modulation without concern for the fabrication difficulty or insertion loss of the

device. As a result, a device was chosen in which the probe beam passes **fully through** the  $\text{VO}_2$  rather than through a silicon bus waveguide with  $\text{VO}_2$  **on top** of it. This chapter is organized as follows: first, the device is discussed and characterized by cw laser light, simulations, scanning electron microscopy, and atomic force microscopy [125]. Next, the optical setup is described, and finally, the chosen device was characterized.

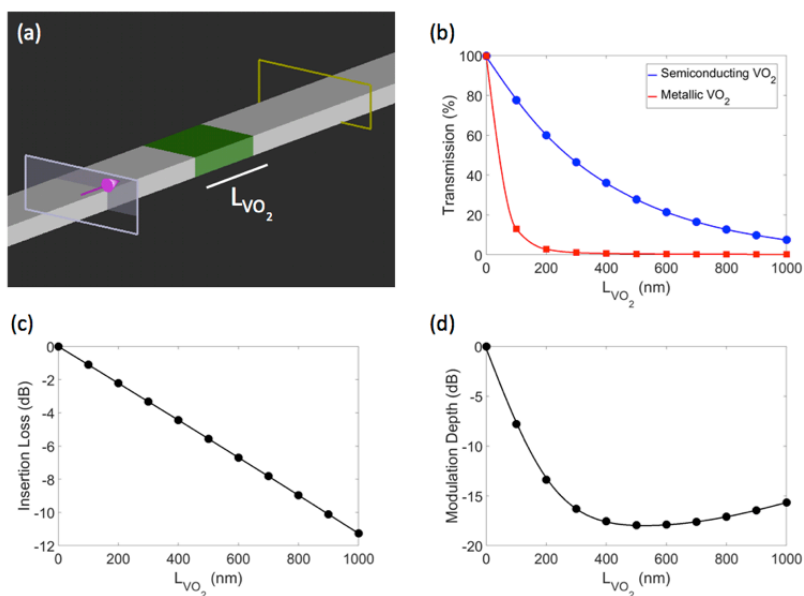


Figure 6.1. (a) Schematic for simulation of  $\text{VO}_2$ -embedded silicon waveguide modulator. The  $\text{VO}_2$ -embedded silicon waveguide modulator is shown in gray (Si) and green ( $\text{VO}_2$ ). The purple arrow surrounded by the gray box and yellow box represent the optical source and monitor, respectively. (b) Simulated transmission as a function of trench length through  $\text{VO}_2$ -embedded silicon waveguide modulator with  $\text{VO}_2$  in its semiconducting (blue circles) and metallic (red squares). Optical properties of  $\text{VO}_2$  are taken from reference [33]. (c) Insertion loss and (d) modulation depth of  $\text{VO}_2$ -embedded silicon waveguide modulator as a function of  $L_{\text{VO}_2}$ , calculated from transmission data shown in (b). The corresponding curve fits in (b), (c), and (d) serve as guides to the eye. Reprinted with permission from reference [125].

## 6.2. Description of Embedded VO<sub>2</sub>-Silicon Hybrid Devices

Figure 5.7 underscores how little interaction there is between the guided mode and the VO<sub>2</sub> on the waveguide in the VO<sub>2</sub>-on-silicon devices. Only the evanescent halo of the mode interacts with the VO<sub>2</sub>. One approach to more efficiently capitalize on the optical properties change in VO<sub>2</sub> could involve embedding a portion of a VO<sub>2</sub> waveguide in a silicon waveguides, as shown in Figure 4.8(a). This section discusses the fabrication and static characterization of these VO<sub>2</sub>-embedded devices.

### 6.2.1. Design and Simulations

The image from the Lumerical FDTD Solutions simulation package shown in Figure 6.1(a) shows an ideal device in which VO<sub>2</sub> is embedded in a trench between two silicon waveguides on a SiO<sub>2</sub> substrate. All simulations were performed using three-dimensional finite-difference time-domain (FDTD) analysis. The width of the waveguide and VO<sub>2</sub> patch was 700 nm and the depth was 220 nm. The length of the VO<sub>2</sub> patch in the direction of propagation ( $L_{VO_2}$ ) was varied from 0 to 1000 nm in steps of 100 nm. Transmission through each waveguide was calculated using frequency-domain field and power monitors; both the semiconducting and metallic states of VO<sub>2</sub> were considered. Optical constants for VO<sub>2</sub> were taken from [33] and imported into Lumerical for the simulations. Figure 6.1(b) shows transmission as a function of trench length for both semiconducting and metallic VO<sub>2</sub> at 1550 nm, presenting individual simulation results using blue circles (semiconducting VO<sub>2</sub>) and red squares (metallic VO<sub>2</sub>). Due to the nearly perfect refractive index match between semiconducting VO<sub>2</sub> and silicon, reflection is simulated to be less than 1% for all VO<sub>2</sub> patch lengths when in the semiconducting phase. Therefore, for semiconducting VO<sub>2</sub>, transmission is dictated by absorption in VO<sub>2</sub> and the curve fit for the transmission data is a single

exponential function obeying Beer's law for an extinction coefficient of about 0.3, which is in good agreement with the optical properties of semiconducting VO<sub>2</sub> films at 1550 nm [33]. The curve fit for the transmission data with metallic VO<sub>2</sub> patches does not simply follow Beer's law for light transmitted through an equivalent thickness VO<sub>2</sub> thin film. This may be related to the spread in the optical mode profile as light passes through the low refractive index metallic VO<sub>2</sub> section of the waveguide causes a significant portion of the mode to propagate in the cladding region outside the lossy VO<sub>2</sub> patch.

Insertion loss and extinction ratio of the VO<sub>2</sub> embedded silicon waveguide switch are calculated from the transmission data in Figure 6.1(b). Insertion loss, Figure 6.1(c), is reported based on the transmission of the VO<sub>2</sub>-embedded silicon waveguide switch when the VO<sub>2</sub> patch is in the semiconducting state relative to the transmission of a control silicon ridge waveguide with no trench and no VO<sub>2</sub>. Extinction ratio, in Figure 6.1(d) is the ratio of transmission through the VO<sub>2</sub> embedded silicon waveguide switch for VO<sub>2</sub> in the semiconducting and metallic states. The trend in extinction ratio as a function of VO<sub>2</sub> length that shows a maximum extinction ratio for a VO<sub>2</sub> patch length of 400 nm can be explained by considering the saturation in the transmission intensity of light through the VO<sub>2</sub> embedded silicon waveguide switch for metallic VO<sub>2</sub> patch lengths greater than about 400 nm. Taking into account both extinction ratio and insertion loss, Figure 6.1 suggests that a favorable geometry is a 200 nm embedded VO<sub>2</sub> patch, which enables nearly 14 dB extinction ratio with approximately 2 dB insertion loss.

### **6.2.2. Device Fabrication**

The VO<sub>2</sub>-embedded silicon waveguide modulators were fabricated with silicon-on-insulator wafers (220 nm device layer, 3 μm buried oxide layer, purchased from SOITEC)

using standard lithographic procedures. Silicon waveguides with and without trenches were defined by electron beam lithography (JEOL 9300FS-100kV) and subsequent reactive ion etching using a  $C_4F_8/SF_6/Ar$  gas mixture (Oxford Plasmalab 100). A second round of electron-beam lithography (Raith eLine) was used to open windows in the trenches for the  $VO_2$  deposition. Then,  $VO_x$  was deposited by RF magnetron sputtering of vanadium metal at 6 mTorr total pressure with 20 sccm Ar and 1 sccm  $O_2$ . After lift-off, the devices were annealed for 7 minutes at  $450^\circ C$  at 250 mTorr of  $O_2$  to form polycrystalline  $VO_2$ . The lithography and  $VO_2$  deposition process was performed in two identical iterations to ensure complete  $O_2$  diffusion during the anneal step. Stylus profilometry on a  $100\ \mu m \times 100\ \mu m$  square of  $VO_2$  patterned on a separate region of the wafer revealed a cumulative  $VO_2$  thickness of 250 nm. The thickness of the deposited  $VO_2$  films embedded in waveguides with differing trench lengths is discussed in Section 5.2.2. Resistive heaters (false colored gold in Figure 6.2) were fabricated adjacent to the waveguides using electron beam lithographic patterning (Raith eLine), thermal evaporation of a 5-nm chromium adhesion layer and a 120-nm gold layer, and lift-off. Additionally, another set of bifurcated silicon waveguides was fabricated with  $VO_2$  deposited on top of the control waveguides in order to compare their performance with the silicon waveguides having embedded  $VO_2$  films.

Figure 6.2 shows a plan-view schematic of a set of devices. Each waveguide on the right side of the image is bifurcated with a Y-shaped splitter into two waveguides on the left. The lower waveguide of each pair on the left side is a standard ridge waveguide for control measurements as seen in the top right inset of Figure 6.2 outlined in blue. The upper waveguide in each pair includes the short  $VO_2$  waveguide. A typical device before and after  $VO_2$  deposition is in the top-left and bottom-left insets outlined in orange, respectively.

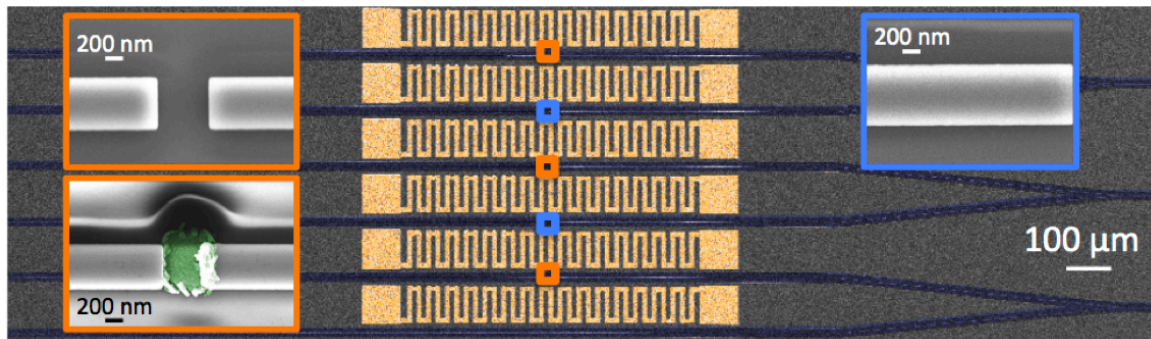


Figure 6.2. SEM image of bifurcated silicon waveguides (false colored navy) including integrated heaters (false colored gold). In the center of the Figure, the small boxes highlight VO<sub>2</sub>-embedded silicon waveguide modulators (small orange boxes) and control waveguides (small light blue boxes). The left insets with orange outline show SEM images after the patterning of the silicon waveguide and trench (top) and backfilling with VO<sub>2</sub> (bottom), which is shown in false colored green. The right inset outlined in light blue shows the control silicon waveguide. Reprinted with permission from reference [125].

### 6.2.3. Static Characterization

Tilted scanning electron microscopy (SEM) images of VO<sub>2</sub>-embedded silicon waveguide modulators with three different trench lengths are shown in Figure 6.3(a). Even the two consecutive VO<sub>2</sub> depositions were not sufficient to completely fill the trenches, and the shorter trenches with higher aspect ratio (ratio of depth to width) had thinner VO<sub>2</sub> films compared to the longer trenches. This issue is most likely due to known challenges with depositing material into high aspect-ratio holes, commonly referred to as shadowing. Atomic force microscopy for a waveguide with trench length ( $L_{VO_2}$ ) of 1000 nm suggest that the VO<sub>2</sub> film thickness in the lowest aspect ratio trench is less than the 220 nm silicon waveguide height and peaks at about 180 nm, as seen in Figure 6.3(c). Note that the deposition of VO<sub>2</sub> on top of the silicon waveguide at one end of the trench, visible in both tilted SEM measurements (Figure 6.3(a)) and the atomic force micrographs (Figure 6.3(b)), was due to

a slight misalignment of the resist window during VO<sub>2</sub> deposition. Atomic force microscopy measurements also show the VO<sub>2</sub> patches on top of the control waveguides (not shown) have a thickness of approximately 210 nm, which is slightly less than the thickness measured with the stylus profilometer of the 100 μm × 100 μm square VO<sub>2</sub> film due to shadowing effects of the resist.

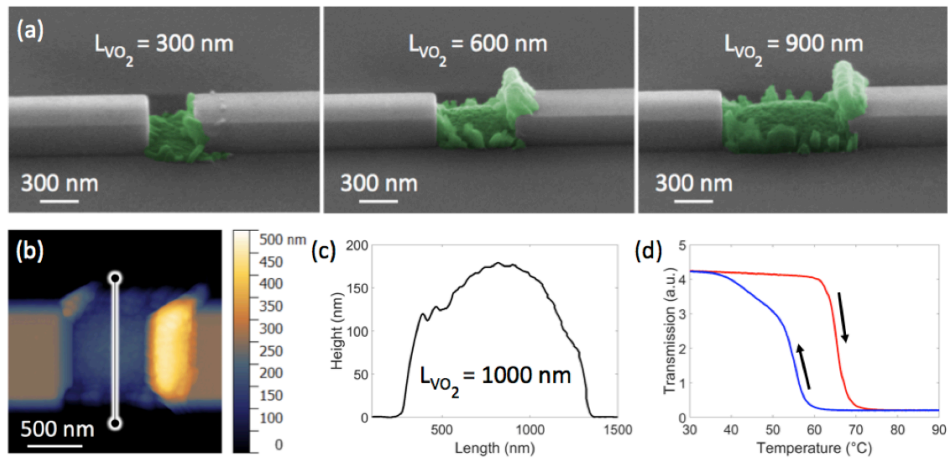


Figure 6.3. (a) Tilted SEM images of VO<sub>2</sub>-embedded silicon waveguide modulators with trench lengths of 300, 600, and 900 nm. VO<sub>2</sub> is shown in false colored green. (b) Atomic force micrograph of VO<sub>2</sub> embedded silicon waveguide modulator with a trench length 1000 nm. Vertical profile of line cut (black line outlined in white) is presented in (c), showing a VO<sub>2</sub> thickness of ~ 180 nm within the trench. (d) Temperature dependent transmission measurements on a thin film VO<sub>2</sub> witness sample. The red and blue curves show transmission with increasing and decreasing temperature, respectively. Reprinted with permission from reference [125].

Waveguide transmission measurements were carried out using the Santec Swept Test System STS-510 software package with a tunable laser (Santec TSL-510) and power meter (Newport 2936-C). The polarization of the input light was controlled by pulling the beam from the polarization-maintaining fiber into free-space where a linear polarizer and half wave

plate were used to obtain transverse electric (TE) polarization. This near-infrared (NIR) light (1500-1630 nm) was coupled into and out of the waveguides using lensed tapered fibers (OZ Optics). Laser light scattered from the sample was coupled into an infrared camera (Sensors Unlimited SU320M) by an infinity-corrected NIR apochromatic microscope objective (Mitutoyo Plan Apo NIR). In addition, a fiber-optic illuminator was used to scatter light from the sample into the camera to aid in alignment.

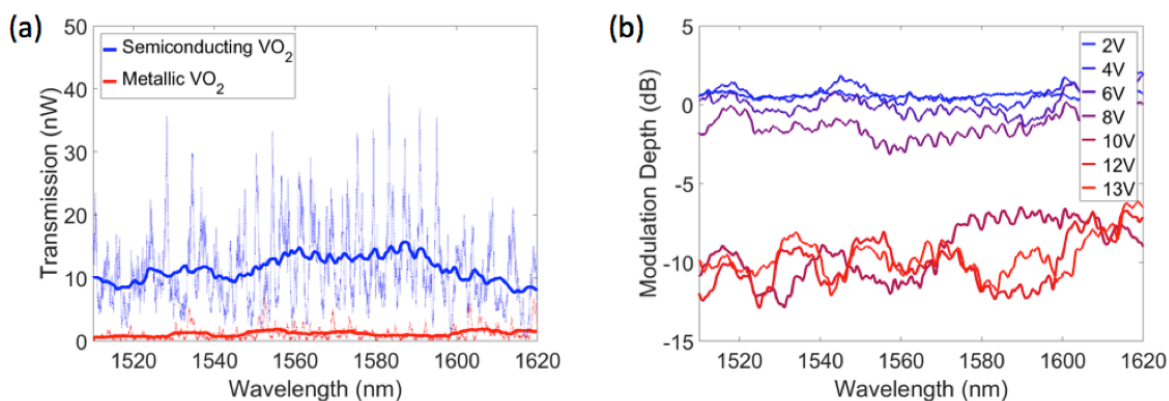


Figure 6.4. (a) Raw (thin lines) and smoothed (thick lines) transmission data through a VO<sub>2</sub>-embedded silicon waveguide modulator with 600 nm trench length. Blue curves correspond to an applied potential of 0V (VO<sub>2</sub> in semiconducting phase) and red curves correspond to 12V (VO<sub>2</sub> in metallic state). (b) Modulation depth, referenced to the 0V measurement, of the same sample for various applied voltages, calculated from the smoothed spectra. Reprinted with permission from reference [125].

High contrast Fabry-Perot fringes observed in the raw transmission spectra, shown as thin lines in Figure 6.4(a), were attributed to reflections or scattering from stitching errors in the waveguides, roughness at the Si-VO<sub>2</sub> and Si-air interfaces, and the bifurcated waveguide splitter. To minimize the effect of the Fabry-Perot fringes, the data were smoothed with a moving average across 10 nm for each data point (5 nm to each side of the data point). Examples of this smoothed data are represented by the thick lines in Figure

6.4(a), and they were used for all insertion loss and modulation depth calculations. To test the phase transition of the VO<sub>2</sub>, temperature-dependent transmission measurements were carried out by varying the potential across the gold resistive heaters. Figure 6.4(b) shows the modulation depth for a number of applied voltages, which is reported based on the ratio of transmission through the VO<sub>2</sub>-embedded silicon waveguide modulator with and without an applied voltage. As indicated by the change in modulation depth, the phase transition of VO<sub>2</sub> was initiated with approximately 8 V applied to the gold heaters and was completed at a potential of about 12 V. For all calculations, we assume that VO<sub>2</sub> is in the semiconducting phase at 0 V and VO<sub>2</sub> is fully in the metallic phase at 13 V. The relatively small variation in optical constants of VO<sub>2</sub> from 1510 to 1620 nm result in a broadband response for the device, as shown by the bandwidth of over 100 nm in Figure 6.4(b).

Trends in the transmitted intensity, insertion loss, and modulation depth were measured as a function of trench length for ten devices were measured at a wavelength of 1550 nm, as shown in Figure 6.5. The error bars in Figure 6.5 are the standard deviation of multiple measurements for each trench length. Note that both the experimental and simulation results in Figure 6.5 deviate from the simulation data presented in Figure 6.1(b,c,d) that assume complete filling of VO<sub>2</sub> in the trench because the fabricated structures have only partially filled VO<sub>2</sub> trenches. The simulation results presented in Figure 6.5 alongside the experimental data assume VO<sub>2</sub> thicknesses from 90 nm for  $L_{VO_2} = 100$  nm to 180 nm for  $L_{VO_2} = 1000$  nm, with a linear interpolation between these values. In other words, the VO<sub>2</sub> thickness in the trench was increased 10 nm in height for each 100-nm increase in  $L_{VO_2}$ . As in Figure 6.1, for all simulation results shown in Figure 6.5, the optical properties of VO<sub>2</sub> were taken from literature [33] and imported into Lumerical.

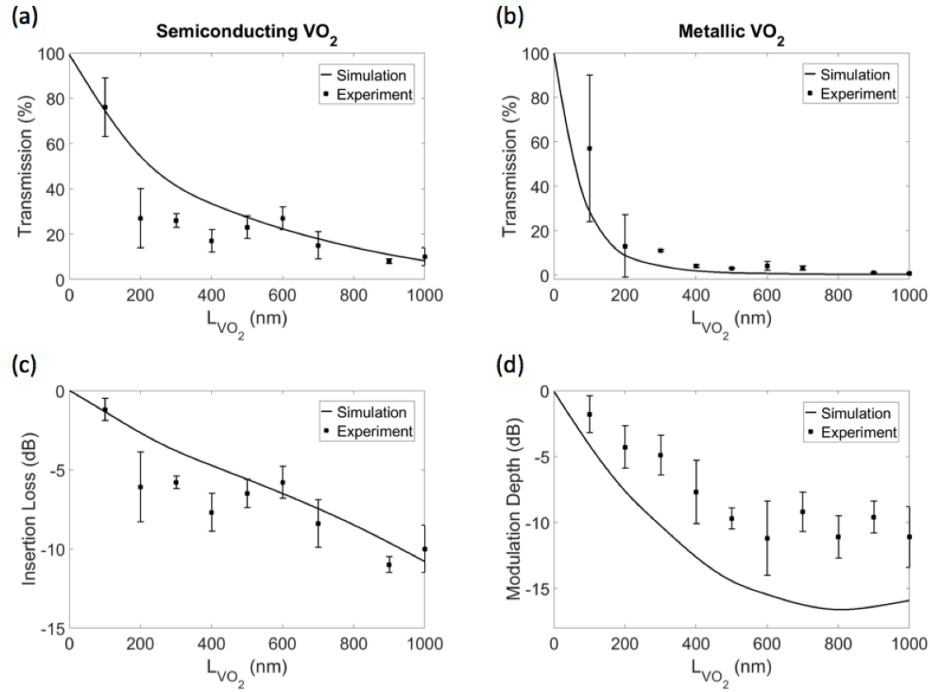


Figure 6.5. Transmission through  $VO_2$ -embedded silicon waveguide modulator as a function of trench length, normalized to the reference silicon waveguide, for  $VO_2$  in its (a) semiconducting and (b) metallic phases. (c) Insertion loss and (d) modulation depth of  $VO_2$ -embedded silicon waveguide modulators as a function of trench length based on measured data in (a) and (b). In all 4 panels, the solid curves present Lumerical simulation results that assume partial  $VO_2$  filling of the trench. Reprinted with permission from reference [125].

The simulations performed with partially filled  $VO_2$  trenches shown in Figure 6.5 are in good agreement with the experimental data. As seen in Figure 6.5(b), when the  $VO_2$  patch is in the metallic phase, the measured transmission is consistently measured slightly higher than the simulated transmission; this difference results in the deviation between experiment and simulation for modulation depth seen in Figure 6.5(d). The data in Figure 6.5 reveal a clear tradeoff between insertion loss and modulation depth as is expected for a waveguide made of a lossy material like  $VO_2$ . Due to the absorption of  $VO_2$  in the semiconductor phase, longer  $VO_2$  filled trenches lead to higher insertion losses. At the same time, the longer  $VO_2$

filled trenches allow more absorption of light when VO<sub>2</sub> is in the metallic phase, leading to a larger modulation depth. For the partially filled VO<sub>2</sub>-embedded silicon waveguide modulator with a trench length of 500 nm, a modulation of  $9.7 \pm 0.8$  dB with a corresponding insertion loss of  $6.5 \pm 0.9$  dB is demonstrated.

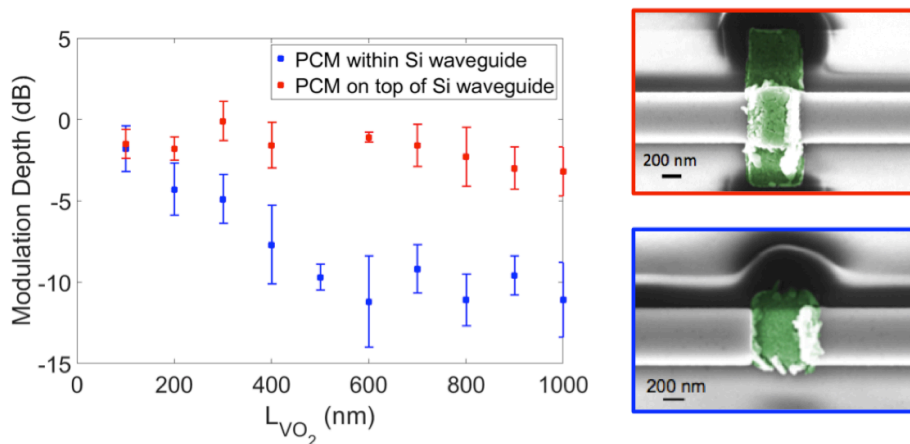


Figure 6.6. Measured modulation depth for Si-VO<sub>2</sub> waveguide modulators with VO<sub>2</sub> on top of (red data points and upper right SEM image) and embedded within (blue data points and lower right SEM image) the silicon waveguide. Reprinted with permission from reference [125].

In order to demonstrate the advantage of placing the VO<sub>2</sub> patch within the silicon waveguide rather than on the waveguide, we carried out a direct experimental comparison, shown in Figure 6.6. As expected, the integrated geometry provides a larger modulation depth because of the improved modal overlap of the guided mode with the phase change material (PCM). Note that although the on-waveguide devices were processed in a manner identical to the embedded devices, the resulting VO<sub>2</sub> thicknesses were slightly different as discussed with the atomic force microscopy results. As seen in Figure 6.1, simulations, which assumes complete filling of VO<sub>2</sub>, for the 200-nm trench length demonstrate a modulation depth and insertion loss of 13.8 dB and 2.2 dB, respectively. Therefore, with improved

fabrication procedures that allow more complete filling of VO<sub>2</sub> in the trench, it should be possible to achieve even larger modulation depths with lower insertion losses using the VO<sub>2</sub>-embedded silicon waveguide modulator platform.

In conclusion, we demonstrate a compact and broadband hybrid Si-VO<sub>2</sub> integrated waveguide modulator. While integration of PCMs into a silicon waveguide in order to improve modal overlap with the PCM has been proposed in the past [126,127], this work is probably the first experimental realization of such a device. Simulations suggest that improved fabrication of these devices could produce modulation depths greater than 12 dB with less than 3 dB insertion loss.

### **6.3. Ultrafast Response of Embedded VO<sub>2</sub>-Silicon Hybrid Devices**

#### **6.3.1. Out-of-Plane Pump, In-Waveguide Probe Configuration**

Figure 6.7 shows the experimental setup used to measure the dynamical response of the waveguide device. An amplified titanium-sapphire laser system (not shown) pumps an optical parametric amplifier (OPA) at 1 kHz, as discussed more thoroughly in sections 2.2.4 and 5.6. The signal beam at 1550 nm is used as the probe beam that propagates through the waveguide; while the idler beam, with a wavelength of 1670 nm, is used as the free-space pump beam. A polarizing beam splitter is used to separate the orthogonally polarized signal and idler beams.

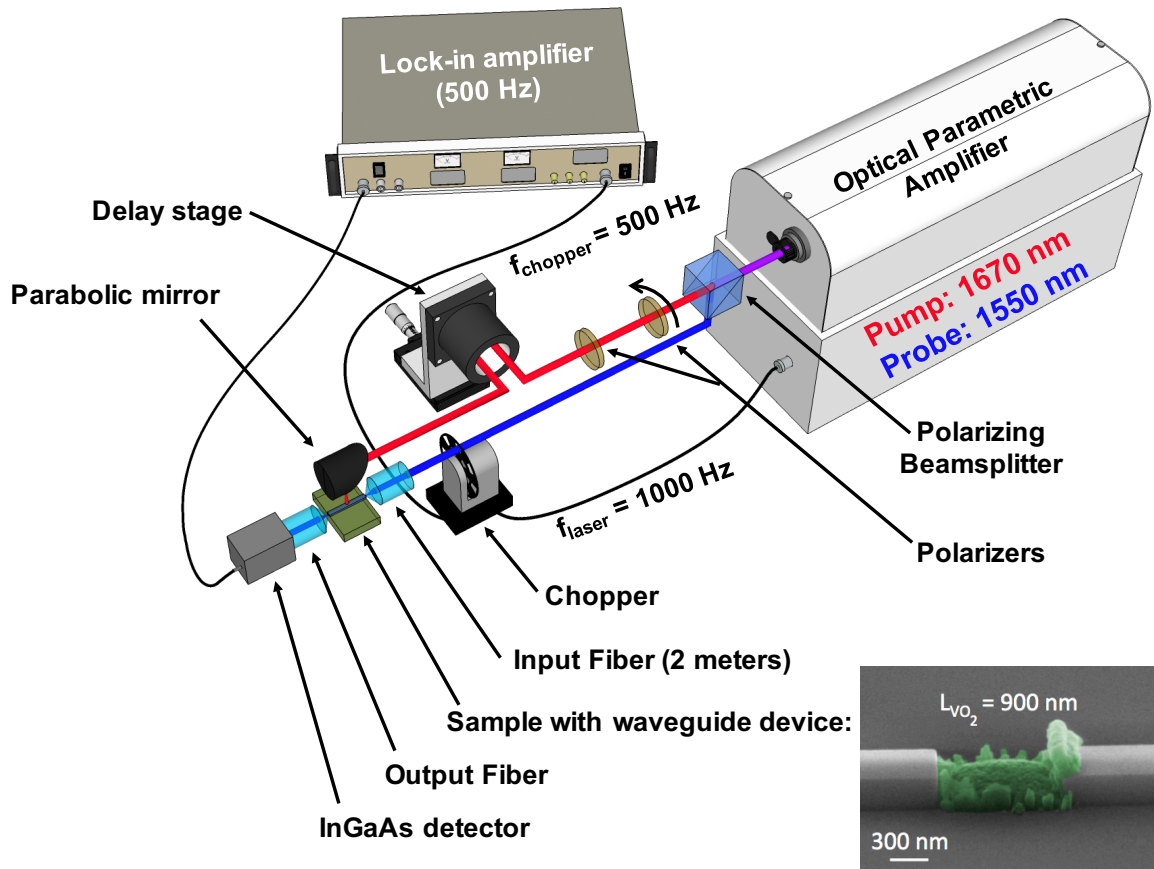


Figure 6.7. Out-of-plane pump, in-waveguide probe optical setup used to measure the time-response of the embedded-VO<sub>2</sub> silicon photonic device.

The pump beam (red, Figure 6.7) is delayed with respect to the probe beam by a corner cube on a translation stage and then focused onto the sample by a parabolic mirror. A pair of crossed polarizers controls the fluence of the pump beam. To prevent the polarization from drifting as the power is changed, only the first (upstream) polarizer is adjusted. The first polarizer is mounted on an automated rotation mount and controlled by the same computer that controls the delay stage and reads data from the lock-in amplifier (LIA). A pyroelectric power meter (not shown in Figure 6.7) on a flip mount in front of the parabolic mirror measures the pump power.

The probe beam is chopped at 500 Hz by an optical chopper synchronized to half the laser repetition rate, and this frequency is used as the reference for the lock-in amplifier. The average power coupled into the probe lensed fiber-tip can be estimated by switching the fiber-tip for an ordinary patch fiber connected to a fiber-coupled power meter. This is used to confirm that the optical chopper is removing half of the average power of the probe beam (half the probe pulses). The input lensed fiber-tip focuses the beam to a 2.5  $\mu\text{m}$  spot and the XYZ piezoelectric actuators on which the fiber-tip is mounted enables coupling that light into the end-facet of the silicon waveguide (220 x 700 nm). The VO<sub>2</sub> device sits in the middle of a silicon waveguide about 2 mm long. However, the VO<sub>2</sub> only extends about 900 nm along the waveguide axis, as shown by the scanning electron micrograph of the device used in these measurements, seen in the inset of Figure 6.7 with the VO<sub>2</sub> in false-color green. The light transmitted from the other silicon waveguide facet is collected by the output fiber-tip, enabled with similar piezoelectric actuators. Without further optical filtering, the fiber-tip delivers the transmitted light to a fiber-coupled indium gallium arsenide (InGaAs) detector. Electrical filtering of the resulting signal is accomplished with a lock-in amplifier locked to the frequency of the probe-chopper. A computer (not shown) controls the delay stage, the delay stage, and the first pump-polarizer (indicated with a curved black arrow in Figure 6.7).

The beam waist of the pump beam spot was measured by blocking the probe beam, changing the LIA reference frequency to 1000 Hz, and translating the parabolic mirror so the beam spot is swept across the device. In this configuration, pump light is scattered from the device and coupled into the waveguide. The magnitude of the scattered light was measured by the LIA as a function of beam spot (parabolic mirror) position and then fit with a Gaussian distribution. Negligible differences between measurements in which the parabolic mirror is

swept parallel and perpendicular to the waveguide axis justify the claim that the axis of the parabolic mirror is aligned to the incoming pump beam axis. Both measurements fit a Gaussian distribution; the beam waist was found to be 35.5 and 34.0  $\mu\text{m}$  for the measurements perpendicular and parallel to the waveguide, respectively.

Note that the pump beam and parabolic mirror axes must be parallel in order to assume that translating the parabolic mirror does not distort the beam spot shape on the sample. This, along with the lack of dispersion and chromatic aberrations in the reflective parabolic mirror, is one advantage of the optical configurations of Figures 6.7 and 5.8 over the setup in Figure 5.2, which uses a refractive microscope objective to focus the pump beam. In order to adjust the pump beam spot position in the setup in Figure 5.2, the microscope objective, along with the two beam splitters, was translated changing the relationship between the microscope objective and pump beam axes. Since it was an apochromatic microscope objective, this was negligible for the nanosecond laser, with a bandwidth less than 1 nm. However, the dispersion and chromatic aberrations would probably not be negligible for a bandwidth of about 40 nm like the femtosecond beam used in the setups in Figures 6.7 and 5.8.

The spectra of the signal and idler beams are shown in Figure 6.8(b), while the raw spectra used to derive them are shown in Figure 6.8(a). To collect the raw spectra, a beam block, which is not shown in Figure 6.7, was placed before the polarizing beam splitter. The scattered OPA light was collected by an optical spectrum analyzer (Agilent 86140B, 100 second integration), and the background was obtained by blocking the amplified Ti:sapphire laser beam before the OPA. Note that the optical spectrum analyzer has a wavelength cutoff of 1700 nm, close to the idler wavelength of about 1670 nm. Near this upper wavelength

limit, a large signal is seen even in the background spectrum, as seen in Figure 6.8(a). Although subtraction of the two raw spectra yields a baseline approximately zero, the noise is large at the detector upper limit and interpretation of the pump-beam peak is difficult. Assuming a transform-limited pulse with a Gaussian temporal distribution, the FWHM of the signal beam of about 40 nm is consistent with a pulse duration of about 175 fs, consistent with the manufacturer specification of 150 to 200 fs.

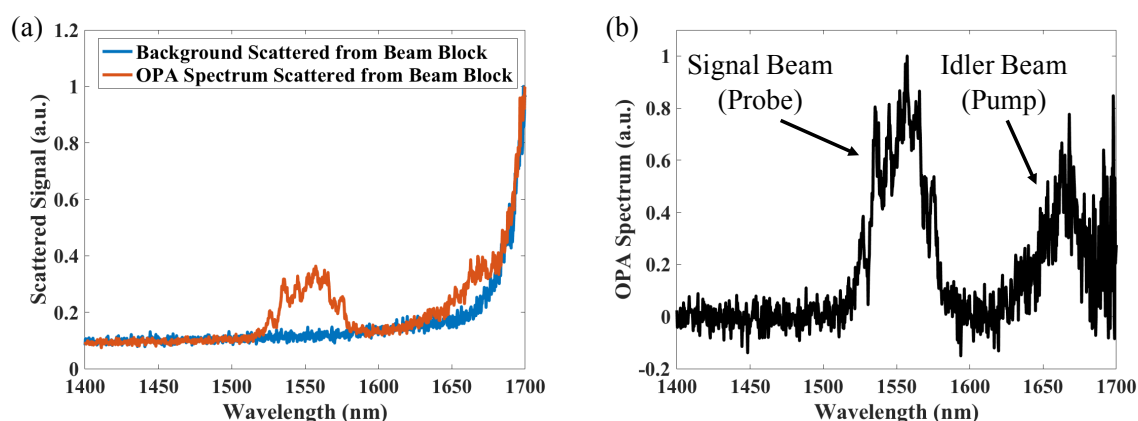


Figure 6.8. (a) Raw measurement before background subtraction and the background spectrum. (b) Pump and probe spectra, extracted from data in (a), scattered from a beam block placed before the polarizing beam splitter.

It should be noted that there are a few differences between this optical setup and a typical pump-probe setup. First, the probe intensity needs to be low enough to avoid nonlinear effects in the lensed fiber tips and silicon waveguide. Second, the probe beam propagates perpendicular to the pump beam. Although one might expect this perpendicular configuration to avoid measuring the pump beam with the detector, significant scattering of the pump beam from the  $\text{VO}_2$  device is observed. This scattered pump light can be conveniently used to fine-tune the position of pump beam spot onto the device, as discussed above. Coarse alignment is achieved with an infrared CCD camera with a 5x Mitutoyo microscope objective with a long working distance mounted at  $45^\circ$  to the sample surface.

Alignment is discussed in much more detail in Appendix B.

The third difference between the out-of-plane pump, in-waveguide probe optical setup and a typical pump-probe setup is that the probe beam is modulated to provide the reference frequency to the lock-in amplifier. Typically, the pump beam is modulated but then optically filtered out before the detector so the probe light is measured but at the frequency of the pump. This yields a signal in the lock-in amplifier that does not correspond to the pump or probe, but to the **effect of the pump on the probe**. Capitalizing on the ability of a lock-in amplifier to turn small AC voltage into a measurable signal, this configuration can routinely measure pump-induced modulations of the probe beam between  $10^{-4}$  and  $10^{-6}$  of the total probe beam power [128]. For our purposes, this is unnecessary because any device with a modulation depth this small would not be technologically useful. The advantage of modulating the probe beam, like in Figure 6.7, is that the optical signal does not need to be coupled from the lensed fiber-tip back into free-beam optics where an additional optic can be used to filter out the pump beam. Although a typical pump-probe configuration for the chopper was utilized at first, it was found that by chopping the pump beam and filtering it out later, the losses associated with the additional optic (the filter) and coupling back into free-beam reduced the signal-to-noise ratio below that of the configuration shown in Figure 6.7 where the probe beam is modulated. Instead, the scattered pump light (at 1000 Hz) was sufficiently small that the band-pass filter in the lock-in amplifier (set at 500 Hz) removed it.

### **6.3.2. Femtosecond Excitation of the Embedded-VO<sub>2</sub> Waveguide Device**

Figure 6.9(a) shows the change in probe transmission as a function of the time delay between the pump and probe pulses for an embedded-VO<sub>2</sub> device with a 700-nm trench similar to those in Figure 6.3(a). The legend gives the incident pump fluence for each

measurement. For clarity, the raw data from Figure 6.9(a) were smoothed with a 5-point running average and re-plotted in Figure 6.9(b). Also note that the axis has been inverted to correspond with typical pump-probe measurements. For example, the transmission of the device with an incident pump fluence of  $7.8 \text{ mJ/cm}^2$  was measured to drop from 100% to about 82%, while  $-\Delta T/T$ , which is typically measured in a pump-probe experiment, rises from a background of about 0% to about 18%.

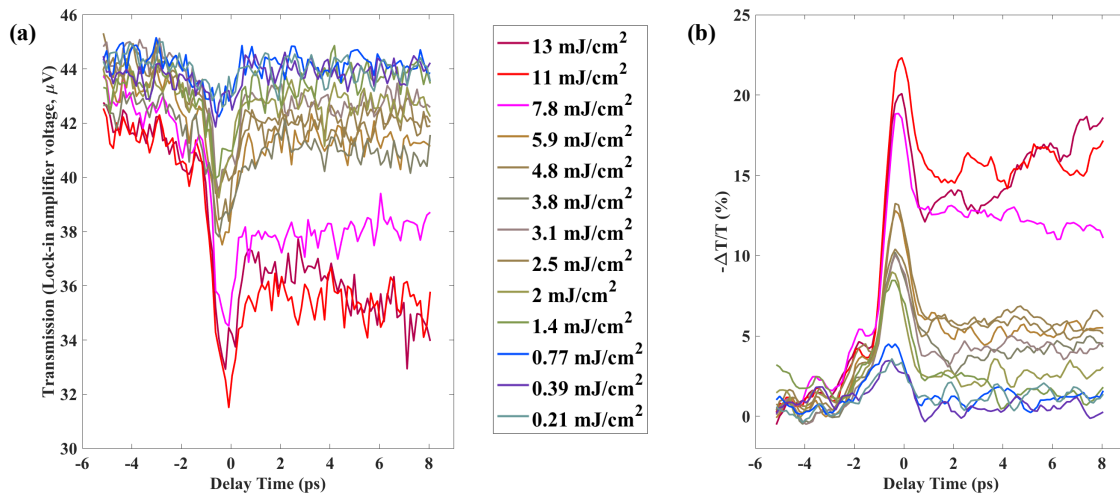


Figure 6.9. (a) Raw lock-in amplifier voltage corresponding to probe transmission through the  $\text{VO}_2$ -embedded device. (b) Data from (a) converted to percent transmission with 5-point smoothing. The legend, which applies to both plots, gives the incident pump fluence for each measurement. The delay stage acceleration was set at  $100 \text{ mm/s}^2$ .

At the highest fluence of  $13 \text{ mJ/cm}^2$ , it appears that the  $\text{VO}_2$  has absorbed enough light to fully undergo the structural phase transition. Below about  $7.8 \text{ mJ/cm}^2$ , the  $\text{VO}_2$  is undergoing the transient metallization discussed in chapter 1 and observed in other work [41,44–47].

In addition to those discussed in the last section, another advantage to this unusual pump-probe configuration, in which the probe beam is modulated rather than the pump beam,

can be understood by comparing Figure 6.9(a) to 6.9(b). During a typical pump-probe measurement, the baseline LIA voltage is zero, like in Figure 6.9(b), so if the probe beam drifts so that it is no longer fully on the detector, the issue will probably not be identified until fitting or comparing with other measurements. However, when the probe is chopped, a drift in the probe beam alignment will manifest itself as a decrease in the raw LIA voltage from the background voltage. For example, in Figure 6.9(a), this background voltage is about  $43 \mu\text{V}$ , and it can be monitored during to confirm probe alignment is maintained. The probe alignment for these experiments is dependent on the fiber tips staying aligned with the facets of the silicon waveguide, so drift is more common than typical for pump-probe measurements.

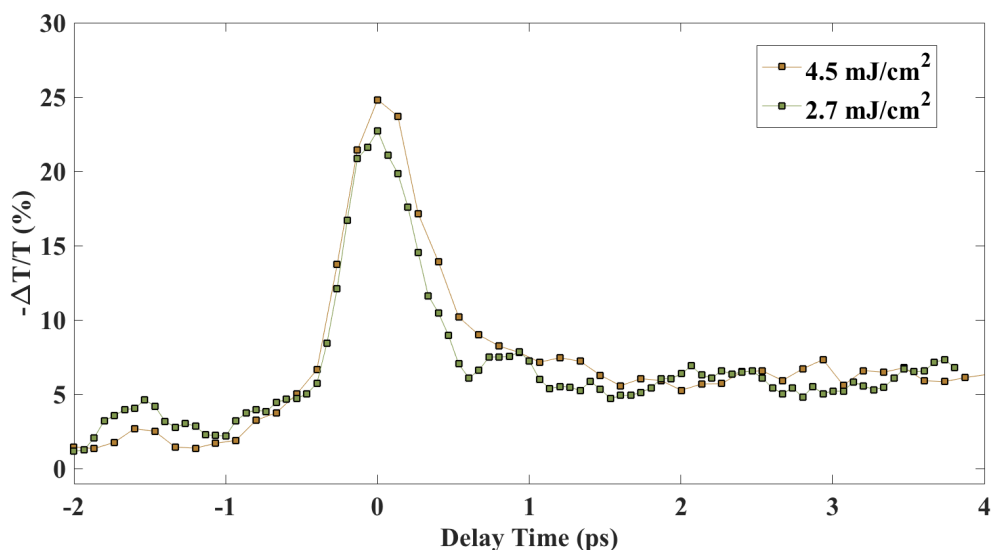


Figure 6.10. Time-response of the embedded  $\text{VO}_2$ -silicon device for a two pump fluences in the mid-fluence regime taken with lower delay stage velocity. Time step size is 134 fs for the  $4.5 \text{ mJ/cm}^2$  measurement and 67 fs for the  $2.7 \text{ mJ/cm}^2$ , and the delay stage acceleration was set at  $10 \text{ mm/s}^2$ .

Even if the fiber-tips that launch and extract the probe signal from the silicon waveguide do not permanently drift as discussed above, we believe small oscillations of the

fiber tips from their equilibrium position can cause issues with these pump-probe measurements. In Figure 6.10, measurements similar to those in Figure 6.9 were performed with the acceleration of the delay stage set to  $10 \text{ mm/s}^2$ . The measurements in Figure 6.9 were taken with an acceleration of  $100 \text{ mm/s}^2$ . At  $100 \text{ mm/s}^2$ , the light scattered from the surface of the silicon waveguide flashed with each stage movement. To observe this, the cw light used to align the setup was necessary because the average power of the femtosecond laser beam is too low to observe the light scattered from the surface of the waveguide with the CCD camera. The removal of these oscillations is responsible for the decreased noise in Figure 6.10 in comparison to Figure 6.9(a); the data in Figure 6.10 has not been smoothed like the data in Figure 6.9(b). It is unclear at this time, however, why the data in Figure 6.10 exhibit an increased contrast and a decreased response time for similar incident pump fluences. All measurements in Figure 6.9 and the  $4.5 \text{ mJ/cm}^2$  measurement in Figure 10 had a  $67 \text{ fs}$  step size, while the  $2.7 \text{ mJ/cm}^2$  measurement was performed with a  $33 \text{ fs}$  step size.

The response of the embedded-VO<sub>2</sub> device is the fastest ever reported for a waveguide device with a FWHM of less than  $1 \text{ ps}$ , corresponding to modulation just over  $1 \text{ THz}$  – a factor of about 3 faster than the current record held by a graphene-based all-optical modulator discussed more thoroughly in Chapter 1 [3]. The modulation depth of about 20%, or about  $1 \text{ dB}$ , is about half of that graphene-based modulator. However, the active portion of the modulator (graphene or VO<sub>2</sub>) is about 25 times shorter for the embedded-VO<sub>2</sub> device, yielding about  $1.4 \text{ dB}/\mu\text{m}$ , over an order of magnitude larger than the graphene-based device. Finally, unlike the graphene-based microfiber device in reference [3], this VO<sub>2</sub>-based embedded in a silicon waveguide is compatible with conventional CMOS fabrication techniques.

At a the threshold fluence for observing modulation,  $1.4 \text{ mJ/cm}^2$  in Figure 6.9(b), the pump energy absorbed by the device was estimated to be about  $1.7 \text{ pJ}$  by using:

$$(6.1) \quad E_{abs} = (1 - R) \cdot (1 - e^{-\alpha \ell}) \cdot V \cdot F_{inc}$$

In this equation,  $V$  is the volume of the  $\text{VO}_2$  embedded waveguide,  $F_{inc}$  is the incident fluence,  $\alpha$  is the absorption coefficient derived from the extinction coefficient in reference [33], and  $\ell$  is the  $\text{VO}_2$  thickness assumed to be  $220 \text{ nm}$ . The reflection at the air- $\text{VO}_2$  interface was calculated using the complex refractive index, again from reference [33], and the equation:

$$(6.2) \quad R = \left| \frac{\tilde{n}_{\text{VO}_2} - 1}{\tilde{n}_{\text{VO}_2} + 1} \right|^2$$

The switching energy of  $1.7 \text{ pJ}$  corresponds to  $0.83 \text{ pJ/bit}$  since, on average, only half of bits in a stream of data requires operating a modulator. This is over eight times larger than a commonly quoted industry target of  $100 \text{ fJ/bit}$  [2]. The threshold for modulating the device in the nanosecond experiments was also estimated using equations 6.1 and 6.2. With the optical constants and reflectivity appropriate for  $\text{VO}_2$  at the pump wavelength of  $1064 \text{ nm}$  and the threshold incident fluence of  $0.63 \text{ mJ/cm}^2$ , a threshold switching energy of  $0.25 \text{ pJ/bit}$  was calculated, about 3.3 times smaller than measured in these femtosecond experiments. The discrepancy between the switching energy for the nanosecond and femtosecond experiments on  $\text{VO}_2$ -based devices could be related to the difference in device geometries or the fundamental difference in the thermally- and photo-induced phase transitions, as discussed near the end of Chapter 5.

Although there is a discrepancy between the switching energy in the nanosecond and femtosecond experiments on  $\text{VO}_2$ -based devices, Table 6.1 illustrates that the threshold absorbed energy density measured in these femtosecond experiments is consistent with

literature. Details of the table contents are in the next paragraph, but a few important facts can be gleaned from its examination. When the pump wavelength and film thickness are accounted for, the result, which has units of energy density, is much more consistent between the literature: the lower bounds on the threshold incident fluence (the first number in each range) vary by over a factor of almost eight, while the lower bounds for the threshold absorbed energy density range by a factor of less than five. Since the thickness may differ between experiments, so an independent variable with units of energy density is more appropriate than what is typically quoted in ultrafast experiments:  $\text{mJ}/\text{cm}^2$ . It is not surprising that correcting for the pump wavelength brings our work in line with literature, since the wavelength-independence of the pump beam has been demonstrated by Rini, *et al.* [46]. They found that as long as the photon energy is higher than the band gap energy for  $\text{VO}_2$  thin films, the threshold fluence was the same, as shown in the 2<sup>nd</sup>-to-last entry in the table. This work, along with the last entry in the table, are included because they are the only two works in which the effect of the pump wavelength was examined for  $\text{VO}_2$  thin films. The third takeaway from Table 6.1 is that even with the wavelength and thickness corrections, the threshold absorbed energy density varies greatly – over a factor of four between the first four entries. In fact, it should be noted that the last two entries measured diametrically opposed trends in the threshold with respect to pump wavelength.

Source	Time Delay (ps)	Threshold $F_{inc}$ (mJ/cm <sup>2</sup> )	Threshold Absorbed Energy Density (mJ/mm <sup>3</sup> )
Brady, <i>et al.</i> [47]	4	0.62-1.12	30-50
This Work	4	5.9-7.8	65-85 (1.67 $\mu\text{m}$ )
Cocker, <i>et al.</i> [38]	4	3.7-4.9	130-180
Wall, <i>et al.</i> [46]	4	4.8-6.1	140-180
Rini, <i>et al.</i> [33]	0.3		120 (1.24, 1.41, 1.63, or 1.91 $\mu\text{m}$ ) 200 (2.30 $\mu\text{m}$ ) 500 (3.35 $\mu\text{m}$ )
Tao, <i>et al.</i> [37]	150		290 (0.80 $\mu\text{m}$ ) 160 (2.00 $\mu\text{m}$ )

Table 6.1. Threshold absorbed energy densities from literature are comparable to that measured in this work. Wavelength of the ultrafast pump beam is 0.80  $\mu\text{m}$  unless otherwise specified. See text above for more details.

The first four entries in this table were constructed by examining plots from each reference with pump-probe sweeps for multiple incident fluences, similar to Figure 6.9. For the purpose of this table, the threshold is defined as the incident fluence at which  $|\Delta T/T|$  ( $|\Delta R/R|$  for Wall *et al.*) drops to **one third** of its maximum value after 4 ps. Thus, the highest (or lowest) fluence at which  $|\Delta T/T|$  had (or had not) dropped by one third at 4 ps was used as

the lower (or higher) limit in the threshold  $F_{inc}$  column. Both the lower and upper limits on the value were converted to threshold absorbed energy density using equations 6.1 and 6.2 and optical constants from literature [33]. Since plots similar to Figure 6.9 were not available for Rini *et al.* and Tao *et al.*, a similar analysis was not possible. As a result, the last entries were not included in the main part of the table. For Rini *et al.*, a similar analysis to the ones above was used with three exceptions; the measure quantity was  $|\Delta\alpha/\alpha|$  rather than  $|\Delta T/T|$ , the only values available were at time delays of 300 fs, and they used their own optical constants in order to quote absorbed fluence. Note that the above definition of threshold fluence does not align with the choice made by Rini *et al.*, so the  $0.25 \text{ mJ/cm}^2$  absorbed fluence threshold that they quote was not used; although even that threshold value yields an absorbed energy density similar to Brady, *et al.* For Tao *et al.*, the absorbed energy densities were given directly in the text for time delays of 150 ps. With such a long time delay, it is not surprising that their value for the 800 nm pump is larger than in all the other works.

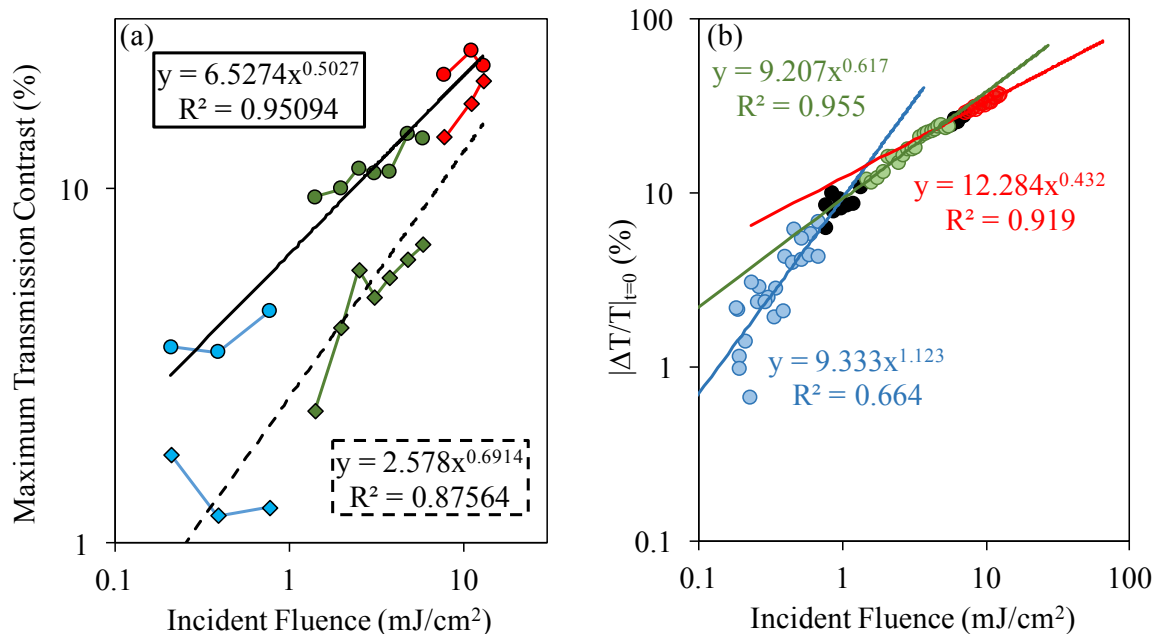


Figure 6.11. (a) Maximum transmission contrast for smoothed curve in Figure 6.9(b) immediately after excitation (0 ps, circles, solid black fit) and after thermal dynamics dominate (7 ps, diamonds, dashed black fit). (b) Transmission contrast at a constant time delay (time-zero) as a function of fluence. The three fits only used the data of the corresponding color. Data points between regime-defining fluences from Figure 6.9 are black and were not included in the fits.

In addition to the fluence threshold discussed in the last few paragraphs, which is readily apparent between  $5.9 \text{ mJ/cm}^2$  and  $7.8 \text{ mJ/cm}^2$  in Figure 6.9, there appears to be another discontinuity in the dynamical response between about  $0.77$  and  $1.4 \text{ mJ/cm}^2$ . While the former discontinuity is obvious, further analysis is necessary to determine if the seemingly apparent transition at about  $1 \text{ mJ/cm}^2$ ; this topic is a majority of the remainder of this chapter. For clarity, the three proposed fluence regimes separated by these two discontinuities are highlighted by the color scheme in Figure 6.9: low fluences with cold-colors, moderate fluences with earth-tones, and high fluences with hot-colors. This color scheme is maintained in Figure 6.10 (only contains two fluences in the middle region) and

Figure 6.11.

In Figure 6.11(a), the upper data points (circles) and fit (solid black line) are the maximum transmission contrast from the smoothed data in Figure 6.9(b) at 0 ps, while the lower data points (diamonds) and fit (dashed black line) are the transmission contrast at 7 ps, after thermal effects dominate the device response. At 0 ps, the power law fit, with an  $R^2$  of 0.95, fits the data nicely, while the response is more complex at 7 ps, as evidenced by the  $R^2$  of less than 0.88 and the obvious systematic error of the fit in the highest fluence regime. This simplistic method of analysis leaves it unclear whether the errors in the low fluence regime are random or systematic and thus it unclear whether the low fluence regime is in fact distinct from the middle fluence regime.

To be certain about this three-region model, a measurement with a constant time delay (0 ps) but finer fluence steps was accomplished by rotating the upstream polarizer (see curved black arrow in Figure 6.7). As can be seen in Figure 6.11(b), similar, though not identical, power law fits for this finer data in the middle and high fluence regimes were obtained. The low fluence data had a power law fit with almost twice the slope of the other two regions. However, the  $R^2$  value for the lowest fluence regime, below 0.66, is quite poor. Furthermore, there is an additional reason to be skeptical of this larger slope for the low fluence regime. In Figure 6.12, the data from 6.9(a) has been re-plotted, and the region near time-zero has been enlarged. Plotted this way, it is more apparent that the peak response shifts with fluence, as denoted by the dashed black arrow. Since the setup was aligned at high fluence, this time-zero shift would accelerate the decrease in transmission as the pump fluence is decreased.

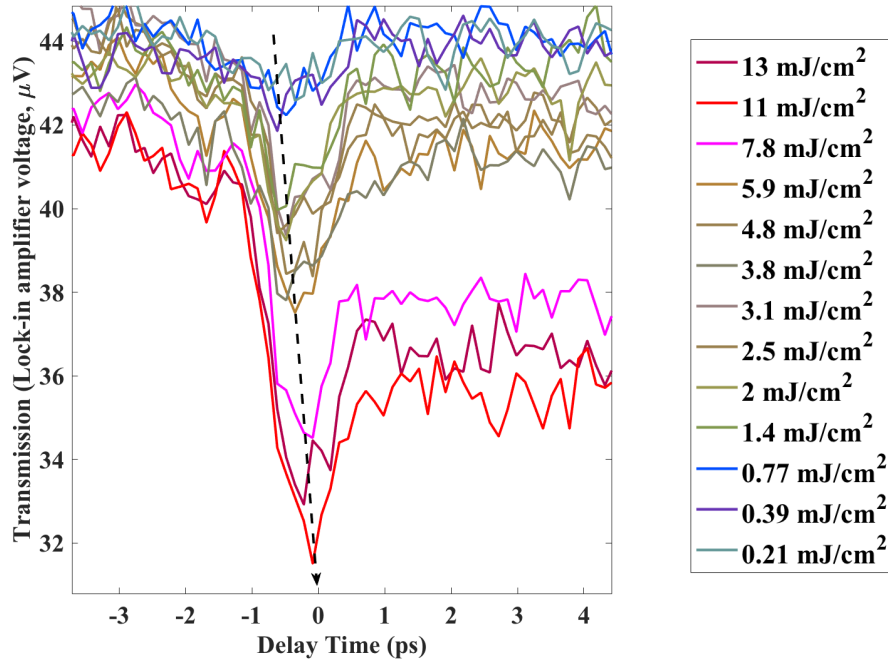


Figure 6.12. Transmission, as raw lock-in amplifier voltage, plotted against time delay. Same data as Figure 6.9(a), but the increased time-resolution of the time axis makes the fluence-dependence of the position of the maximum transmission more obvious.

With potential for modulation speeds in the THz range, these findings suggest all-optical modulation devices based upon this  $\text{VO}_2$ -silicon hybrid platform could play a role in the future of optical communications. However, the energy required to switch the device and the modulation depth require improved device geometry. Based upon the low modulation contrasts in comparison to the  $\text{VO}_2$ -on-waveguide structures presented in Chapter 5, the embedded- $\text{VO}_2$  design may not be worth the additional fabrication difficulty. Potential improvements to the transmission contrast could come from resonant structures, while electric field enhancement from plasmonic structures or photonic crystals could decrease the switching fluence.

## CHAPTER 7

### CONCLUSIONS

#### 6.1. Summary

The work in this dissertation first expanded the knowledge of the phase transition of vanadium dioxide and then explored the possibility of utilizing the associated transformation in optical properties in all-optical modulation devices.

In Chapter 3, density functional theory calculations predicted the electronic and magnetic structure of the M1, R, and M2 phases of VO<sub>2</sub> with a single set of hybrid functionals. This unprecedented success suggests that single-particle theories are sufficient to describe the individual phases of VO<sub>2</sub>; electron correlations are not needed. An additional phase of VO<sub>2</sub> is predicted, called the M0 phase, and is found to be ferromagnetic. It may be related to reports of ferromagnetic VO<sub>2</sub> [82,129–132].

In Chapter 4, x-ray holography experiments, with nanoscale spatial resolution, demonstrate that defects can cause local fluctuations in the activation energy for the thermally-induced phase transition, nucleating the transformation. Spectrally-resolved x-ray holographic measurements suggest that there can be more than one pathway from the M1 phase to the R phase. While a direct transition from M1 to R is observed, other positions in the crystal pass through an intermediate phase, most similar to the M2 phase. These observations, gathered from the thermally-driven phase transition, have limited implications for all-optical modulation applications requiring the ultrafast photo-induced transition. However, the success of these thermal x-ray holography measurements suggest that analogous

femtosecond measurements can be performed with a combination of near-infrared and x-ray pulses and inform future design of VO<sub>2</sub>-based all-optical modulators.

In Chapter 5, the ability of VO<sub>2</sub>-on-silicon waveguide devices to modulate cw light was characterized. First, nanosecond laser pulses were used to modulate both resonant (VO<sub>2</sub> on a silicon ring resonator) and non-resonant (VO<sub>2</sub>-on-silicon absorption modulator). Both sets of devices were able to modulate the cw on a timescale faster than the nanosecond laser pulse could resolve. As a result, femtosecond pulses were employed on the ring resonators. Above a threshold fluence of about 0.24 mJ/cm<sup>2</sup>, the results aligned with expectations and the nanosecond modulation results. Below the threshold fluence, a fast signal, with a response time of about 500 ps, was observed. However, the response did not have the expected spectral features and the temporal resolution of the detector, about 250 ps, made characterization difficult.

In Chapter 6, a pump-probe experimental configuration was employed to obtain a higher temporal resolution. A non-resonant device geometry was chosen to eliminate the need for spectrally-resolved detection and the unexpected spectral feature found with the ring resonators at low fluence in Chapter 5. To maximize the signal, the VO<sub>2</sub>-on-waveguide device geometry used in Chapter 5 was not employed; instead, an embedded-VO<sub>2</sub> device was used. Chapter 6 begins with the fabrication and characterization details of that device. Then, the out-of-plane pump, in-waveguide probe optical setup built for the project was overviewed before the measurement results for the embedded-VO<sub>2</sub> device were presented. A modulation of about 15% in the device transmission was observed with a FWHM of about 500 fs. To date, this modulation speed of about 2 THz is the fastest reported for a waveguide-device. These results suggest that a VO<sub>2</sub>-based all-optical modulation platform could be a viable

method of directing the flow of optical information.

## 6.2. Impact and Outlook

In the quest for a VO<sub>2</sub> all-optical modulator, a firm understanding of all aspects of VO<sub>2</sub> and its phase transition are crucial. From the density functional theory calculations in Chapter 3, two principal outcomes could be relevant for a VO<sub>2</sub> all-optical modulator. First, the ability of band theory to predict the VO<sub>2</sub> phases suggests that future modeling of the material does not need to invoke strong correlation far from its phase transition temperature. Secondly, the prediction of a non-transient monoclinic metallic state, M0, suggests that the complex phase space of VO<sub>2</sub> has yet to be fully explored and that there may be a way of stabilizing the transient monoclinic metallic state and thus reducing the switching threshold. The relationship between this monoclinic metallic state and the phase transition was further underscored in Chapter 4 by x-ray holography experiments. This work suggested not only corroborates the thermally-induced monoclinic metallic state, but also suggests the phase transition nucleates at defects and passes through an M2-like monoclinic metallic phase. It remains to be seen whether this observation of the thermally-induced transition has implications for the photo-induced transition. However, these measurements, which do not require rastering an x-ray beam to obtain the nanoscale spatial resolution, paves the way for a similar femtosecond experiment. Such a femtosecond stop-action movie could provide invaluable information about the nanoscale evolution of the ultrafast VO<sub>2</sub> phase transition.

The demonstration of nanosecond experiments in Chapter 5 underscores the claim that the large change in optical properties across the phase transition of VO<sub>2</sub> can be harnessed in an all-optical modulator device. Although modulating a resonant device, a VO<sub>2</sub>-enhanced

silicon ring resonator, with a femtosecond laser beam yielded results which were difficult to interpret, a response faster than the resolution of the detector, about 250 ps, was discernable for the VO<sub>2</sub>-based device. This justified developing a pump-probe measurement in which the probe propagated along a silicon waveguide.

Using this pump-probe optical setup, the response of an embedded-VO<sub>2</sub> device was demonstrated to be the fastest all-optical modulator reported for a waveguide device. With a FWHM of less than 1 ps, the response corresponds to modulation just over 1 THz, a factor of about 3 faster than the current record held by the previous record holder, a graphene-based all-optical modulator [3]. The modulation depth of about 20%, or about 1 dB, is about half that of the graphene-based modulator. However, the active portion of the modulator (graphene or VO<sub>2</sub>) is about 25 times shorter for the embedded-VO<sub>2</sub> device, yielding about 1.4 dB/μm, over an order of magnitude larger than the graphene-based device. Finally, unlike the graphene-based microfiber device in reference [3], this VO<sub>2</sub>-based embedded in a silicon waveguide is compatible with conventional CMOS fabrication techniques.

These results represent significant progress in the field of optical communications and perhaps a small step toward the distant goal of all-optical computing. To realize even the former goals, progress must include pumping the VO<sub>2</sub> device on the chip and reducing the energy required to switch the device while increasing the modulation depth. Possible ways to facilitate these improvements could involve enhancing the electric field in the vicinity of the VO<sub>2</sub>, perhaps by incorporating the VO<sub>2</sub> into a resonant photonic crystal or bringing plasmonic structures in close contact with the VO<sub>2</sub>. Increasing the modulation depth could involve optimizing a device geometry to simultaneously take advantage of **both** the refractive index and absorption coefficient change across the phase transition. This would be

in contrast to the device contained in this dissertation, which only leveraged one of the two at a time. For example, the ring resonators drew their modulation characteristics from the change in refractive index, while the on-waveguide and embedded devices leveraged the difference in absorption in the two VO<sub>2</sub> phases.

Although the work in this dissertation accomplishes a few necessary steps to realizing all-optical modulator based on VO<sub>2</sub>, many crucial questions remain unanswered. One necessary but illusive explanation is the origin of the decrease in cw-transmission upon femtosecond excitation below about 0.24 mJ/cm<sup>2</sup>. In addition, the factor of 3.3 higher threshold for observing device modulation in the femtosecond experiments, when compared to the nanosecond measurements, needs to be understood. The nanosecond experiments demonstrated that resonant devices and non-resonant (Figure 5.4(a)) have the same fluence threshold for switching, but it remains to be seen whether a resonant device can be designed to increase the modulation contrast. Decreasing the threshold fluence could involve device configurations like photonic crystals, or the addition of plasmonic particles, that enhance the electric field from the pump beam. Finally, attempts to compare these device-based measurements to traditional pump-probe experiments has revealed a dearth of information on the near-infrared pumping of VO<sub>2</sub>, especially at low fluences. Since the optical communications bands lie at 1.31 μm and 1.55 μm, this information is vital to realize, and even consider further, commercialization of products harnessing the phase transition of VO<sub>2</sub> for optical communication applications. Although this dissertation has made small steps toward a VO<sub>2</sub>-based all-optical communications, there is still much work to be done.

## APPENDIX A

### ALIGNMENT PROCEDURE FOR OUT-OF-PLANE PUMP, IN-WAVEGUIDE PROBE OPTICAL SETUP

#### A.1. Introduction

Below is the simplest process for aligning the out-of-plane pump, in-waveguide probe setup in order to take a measurement. The details of the process assume that the pump is the OPA idler beam at about 1670 nm and the probe is the signal beam at roughly 1550 nm. It is presented in the order that I believe to be clearest, although doing a set of numerous measurements in this order would be impractical. I will explain why it is impractical and how I compensate for that in more detail in paragraphs before or after a list of steps; each **Procedure** has a list of steps. I will give one such example after I quickly define the **Procedures** of the alignment process:

**Procedure #1 (Section A.2):** Align free-beam optics for the pump arm. This process includes making sure the beam entering the corner cube is parallel to the axis of translation of the delay stage so there is no drift of the beam spot position on the sample surface.

**Procedure #2 (Section A.3):** Align free-beam optics for the probe arm. This must be done after the pump arm since the pump arm only has the minimum number of degrees of freedom (mirrors). But there are extra degrees of freedom in the probe optics that can then be used to adjust for any mis-alignment of the probe arm introduced during alignment of the pump arm.

**Procedure #3 (Section A.4):** Align probe fiber-tips to the waveguide device. Just

like for the fiber-tip setup in the Weiss laboratory, scattering from the waveguide imaged in the CCD camera can aid alignment. However, the scattering from the femtosecond laser is near impossible to use because of the low average power of the beam. Instead, use the cw laser and the Thorlabs power meter. After it is aligned, drift can be compensated using the femtosecond beam, the fast photodiode, and the LIA.

**Procedure #4 (Section A.5):** Align pump beam spot on device. You will move the parabolic mirror around parallel to the surface of the optics table to move the beam spot around the surface of the sample until you find your device. In the embedded-VO<sub>2</sub> devices, the easiest way to do this is by blocking the probe beam and measuring

**Procedure #5 (Section A.6):** Measurement. During a measurement, a Labview program will move the delay stage a number of equally spaced increments, taking reading from the LIA at each position.

I will give one example of a useful modification to the above order of the Procedures here: The Poynting vector drift of the OPA-output is most severe in the first hour after it is turned on. So, if the OPA was turned on recently and I am loading a new sample, I will jump to Procedure #3, since this might take up to an hour with a new sample. Then I will go back to Procedure #1 to reduce the probability that the pump beam and probe beam alignments will become misaligned right after my careful alignment. After Procedure #2, I will re-perform a simplified variant of Procedure #3, with only the piezo-controllers, that usually takes less than a minute.

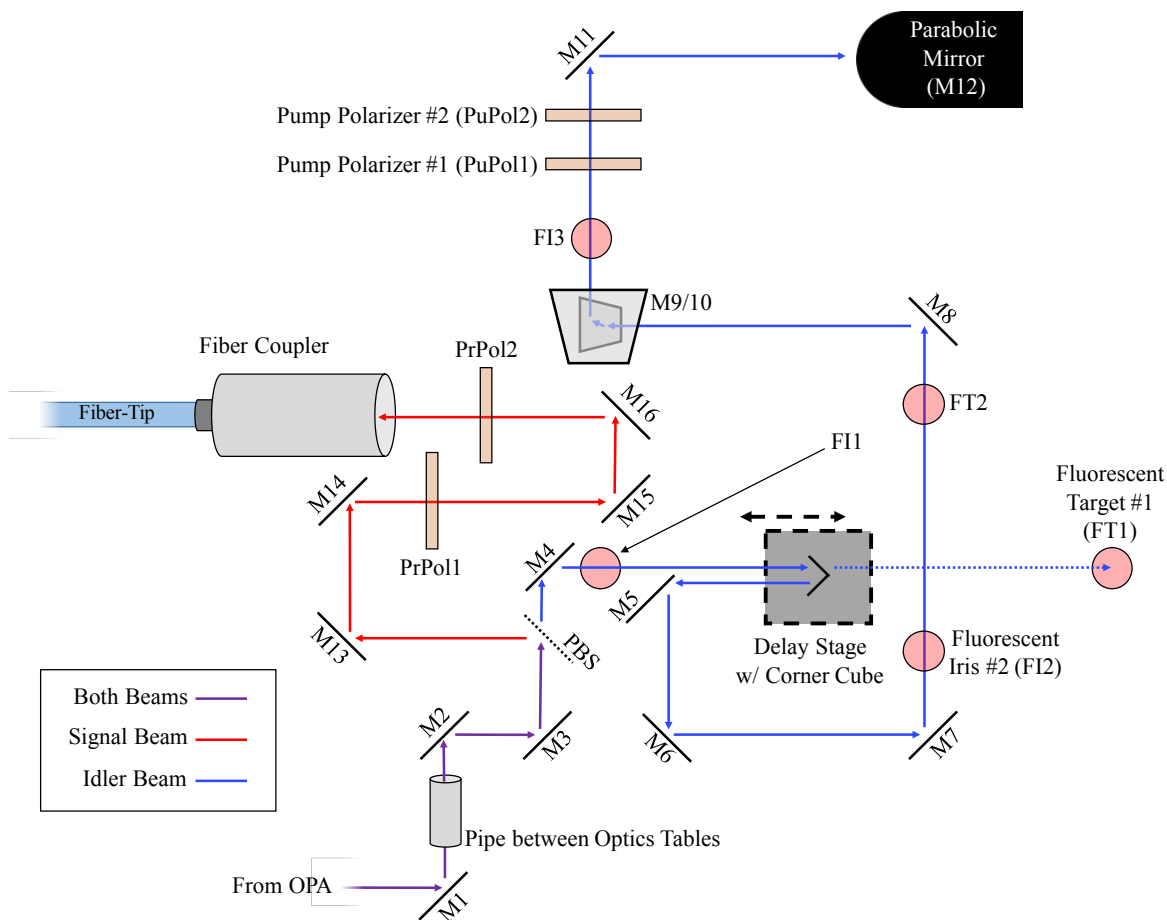


Figure A.1. Plan view schematic of out-of-plane pump, in-waveguide probe optical setup. Abbreviations are defined in the text. Dotted blue line represents idler beam only during alignment Steps 6-8. Fluorescent target and iris indicators represent the mounts where the fluorescent object should be place during the appropriate alignment step. The sample and fiber-tips near the sample are not shown for clarity; they would be beneath the parabolic mirror. Not drawn to scale.

## A.2. Align Pump Beam

1. Measure power right after OPA using the purple Coherent power meter. Should be  $>200$  mW. If not, bug the OPA-operator.
2. Measure power after all the filters on the Tolk optics table. Should be at least 50% of what you measured in Step 1.

3. Block sample by flipping the pyroelectric power meter up.
4. Acquire collimate-able flashlight (this procedure works best when the batteries are a little on the dead side). Turn off room lights completely. Turn off Squid-light, computer monitors, and CCD camera monitor.
5. Using fluorescent card (Thorlabs VRC2), confirm:
  - a. Beam is hitting center of mirror #1 (M1). On the rare occasion that it is not hitting M1 centered, block the OPA and move the mirror-mount of M1 around on the optics table while keeping the angle of the mirror at roughly  $45^\circ$  (easiest way to do this accurately is look down from above and compare to the line of screw holes that should be roughly  $45^\circ$  to the beam path and parallel to the mirror surface).
  - b. Beam is hitting center of mirror #2 (M2). If not, adjust M1 knobs.
  - c. Beam is hitting center of mirror #3 (M3). If not, adjust M2 knobs.
  - d. Both pump and probe beams are passing through opening in the polarized beam splitter (PBS). They will almost certainly not be centered but that is okay. Check that the beam transmitted from the PBS is the pump beam by watching the beam disappear when you switch from the VRC2 card to the VRC4 card.
  - e. Pump beam is hitting center of mirror #4 (M4). If not, adjust M3 knobs.

Note that it is rare to need to make any of the adjustments in Steps 3a-3e. If the setup has been used in the past month, it is probably not necessary. But check anyway or it may make your life much more difficult later in this procedure.

Below, a fluorescent target (FT) or fluorescent iris (FI) is the small object about the size of a quarter, but when given a number (e.g. FT1), it indicates a position on the optics table where you should find an optics mount to hold the object. The height of these are pre-defined, so you should only unscrew (screw) in the object about the size of a quarter.

6. Install fluorescent iris #1 (FI1) without unscrewing anything. Install a FT into one into fluorescent target #1 (FT1) by screwing it into the mount label 'DO NOT TOUCH' near the SLM without moving the mount or lens tube. Remove corner cube from delay stage by rocking it toward you in the way Kent will taught you.
7. Using M3 and M4, align the beam to FI1 and FT1:
  - a. Adjust knobs of M3 to get beam centered on FI1.
  - b. Adjust knobs of M4 to get beam centered on FT1. This will probably mess up what you did in Step 5a.
  - c. Repeat Step 5a + 5b until the beam is aligned to both FI1 and FT1.
8. Replace corner cube from delay stage in the way Kent will taught you. The motion is the reverse of Step 6. Do not touch it if Kent has not yet taught you how to do this smoothly by preventing the magnet mount from slamming.
9. Confirm that beam is hitting the corner cube and the pickoff mirror (M5). If it is not, DO NOT ADJUST THEM. Instead check that Step 5 was done correctly. Consult with Kent before adjusting corner cube or pickoff mirror.
10. Move fluorescent target from FT1 to FT2. If FI2 does not have a fluorescent iris in it, go get it from FI3. Install both FI2 and FT2. Although you can uninstall FI1 at this point, I prefer to leave it in place in order to better define

the beam path in the next Step. If you do remove it, do so without unscrewing anything.

11. Using M6 and M7, align the beam to FI2 and FT2. See Steps 7a-7c for an analogous discussion on how to do this.
12. Repeat/confirm Step 3 before you uninstall FI2 and FT2. Do not unscrew anything with a hex-key when you uninstall them. If you have not removed FI1 yet, do so now.
13. Confirm that beam is centered on M8, both telescope mirrors (M9/M10), beam block, Pump Polarizer #1 (PuPol1), and M11. If it is not, revisit Steps 10-11.
14. Optional. Check alignment of PuPol1. This Step is optional if the automated rotation mount (mount for PuPol1) has not been borrowed recently. Note that this is probably the most difficult part of the alignment and it is unnecessary for most measurements, so skipping it is advisable in most situations.
  - a. Move fluorescent iris from FI2 to FI3.
  - b. Turn off all sources of light.
  - c. Make sure beam is aligned on hole of FI3 and look for the back reflection from PuPol1 on FI3. If alignment is good it will be in the aperture and you won't be able to see it. If alignment is terrible, it will be off the target and you won't be able to see it on FI3. You'll either need to move FI3 closer (do not unscrew the mount from the table though) or use a fluorescent card to find the back reflection. To aid in identifying the back reflection, you may rotate PuPol1 and look for a

dot that moves in a circular pattern. You may also block/unblock the beam block and look for the appearance/disappearance of a dot. You may also move the tip-tilt knobs of the PuPol1 mount to see if it is in the aperture already.

- d. Once you have found the back reflection from PuPol1, use the tip-tilt knobs to put the back reflection into the aperture so you cannot see it. Now the beam is perpendicular to the PuPol1 surface and rotating it should not move it off the device.

15. REPEAT/CONFIRM STEP 3. If you don't confirm Step 3, you might blow the devices to bits, so MAKE SURE YOU HAVE BLOCKED THE SAMPLE before doing this. Unflip pump power-meter and confirm that beam is hitting centered on the parabolic mirror (M12). If it is not, adjust M11 knobs. If you cannot see it, you may rotate PuPol1 to obtain more power.

16. Make sure you do this Step after Step 11. Confirm that beam is hitting centered on Pump Polarizer #2 (PuPol2) and the pump power-meter (you'll have to flip it up). If it is not, revisit Steps 11-15.

17. If you turned up power using PuPol1 in Step 14, turn it back down to 200 nJ/pulse.

18. Turn on room lights, monitors, and Squid-light.

Procedure #1 will need to be repeated if the OPA Poynting vector drifts. This is indicated by a linear background at negative time delays (probe before pump, usually +30 to +50 mm as defined by Labview and the SMC software) as the corner cube is translated. Note that this background should not simply be subtracted since it occurs as a result of pump beam

spot movement on the sample surface, and thus a fluence on your device that is dependent on the position of the delay stage.

### **A.3. Align Probe Beam**

Now that the pump optics are aligned, the probe optics can be aligned. The pump alignment (Steps 1-18) should be done before the probe alignment (Steps 19-28) because there are more degrees of freedom to play with in the probe optics so you can compensate for any misalignment you caused in Steps 1-18.

19. If the blue patch-fiber or fiber-tip is still connected to the probe coupler, remove it now.
20. Re-confirm that both pump and probe beams are passing through opening in the polarized beam splitter (PBS) using a fluorescent card (VRC2). Check that the beam reflected from the PBS is the probe beam by seeing the beam stay when you switch to the VRC4 card. In contrast, the pump beam, which is transmitted through the PBS, should not appear on the VRC2 card, as you should have confirmed in Step 5d.
21. Confirm that the beam is sufficiently centered on M13, the first mirror after the PBS. If it is not, you should first check that the pump beam is still aligned (see Procedure #1), since this is exceedingly rare.
22. Confirm that the beam is centered on the next three mirrors: M14, M15, and M16. You may need to move the chopper blade to unblock the beam. If it is not sufficiently centered on M14, adjust the knobs of M13. If it is not centered on M15, adjust the knobs of M14. If it is not centered on M16, adjust the knobs of M15. Do not make changes if it is not necessary since this will make

the next couple steps more difficult. You may need to turn down the room lights and rotate the first Probe Polarizer (PrPol1) so that you can see the signal beam (at 1550 nm) on the fluorescent card. But take note of the polarizer setting before you do this. Note that you should never have to adjust the second probe polarizer (PrPol2) since that one defines the polarization entering the fiber-tip.

23. Using the blue patch-fiber, connect the probe coupler to the probe power meter (Thorlabs readout with very small InGaAs detector directly attached, called PrPM for the rest of these instructions). If you can measure the power, then you may skip the next Step. If not, try turning the PrPol1 to increase the power. However, if you cannot read a power, precede to the next step so you do not damage the patch fiber.
24. Optional – only necessary if you cannot read probe power in Step 23. Remove the blue patch-fiber so it is not damaged in this process. Turn out the room lights. Install a fluorescent iris or aperture onto the input side of the probe coupler. Using the knobs of M16, center the beam on the iris. Turn the PrPol1 back down to the value you found in Step 22, re-connect the blue patch fiber to the coupler, and then open the iris. You should be able to measure a value in the PrPM now.
25. Open the iris and optimize the power using the knobs on M16.
26. Close the iris until the power drops by about half. Re-optimize the power using the knobs on M15, making sure to make large sweeps (large turns with the knobs) and ignore spikes as you cross the edge of the iris.

27. Repeat Steps 25 + 26 until there is little change between the two. Make sure to end after an iteration of Step 25. Note that this is similar to the procedures in Step 7 and Step 11 (two mirrors-two irises technique) except that the second iris is the detector and you measure whether it is hitting the irises by looking at the value on the PrPM readout rather than looking at fluorescence from the iris or target. Do not be too careful on this step, since the main reason for this optimization process (rather than just performing Step 23 alone) is to make sure that the beam is hitting centered on the lens behind the iris relatively. The main purpose for hitting the lens centered is to reduce aberrations. This will prevent spatial and spectral chirp in the fiber.
28. Watching the PrPM, adjust the PrPol1 until you obtain the desired probe power. Remember that you will lose about 90% of that power when the light is coupled into the waveguide from the fiber tip (and another 90% from waveguide back to fiber tips).

#### **A.4. Align Probe Fiber-tips**

Even if you have learned how to couple fiber-tips to waveguides in Weiss lab, I would suggest at least skimming this section because it is trickier in this setup since the older CCD camera and 5x microscope objective lead to a much lower resolution image of the sample and fiber-tips. Perhaps more importantly, the CCD camera is at about  $45^\circ$  to the sample, not normal like in the Weiss lab. This not only means that only one or two waveguide devices will be in focus at one time, but moving the fiber-tips in the x- or z-directions (see below for coordinate definitions) will result in the fiber-tip moving toward or away from the ceiling on

the monitor. Consequently, you cannot simply align the fiber-tips in the x-direction (or z-direction) by making it collinear (or simultaneously in-focus) with the waveguide of interest like you can in the Weiss lab.

The coordinates I will use in these Procedure details will be defined as follows:

- The x-direction is axis of the waveguide, or the direction of propagation of the light while in the waveguide.
- The y-direction is perpendicular to the x-direction but still parallel to the table (or sample) surface. You will move the sample in the y-direction to change waveguides on the same sample.
- The z-direction is perpendicular to the x-direction but parallel to the normal-vector of the table surface (or sample surface). This should not be changed much, since that would change the distance between the sample and the parabolic mirror (M12). That would change the spot size, and in turn, the fluence on the device. That having been said, as long as the z-micrometer of the sample stage holder stays the same (8.0 mm), the thickness of the sample stays at 0.5 mm, and the sample is one carbon-tape-thickness (negligible) off of the brass sample stage, the z-position of the sample surface should have a negligible effect on the fluence at the device since the parabolic mirror has a focal length of 2 inches.

Note that I will refer to similar coordinates for both fiber-tips, the CCD camera, and the parabolic mirror (M12). However, the right fiber-tip is has a different x and z definition (they are flipped) so I will use  $x'$  and  $z'$  for those (primed coordinates are the coordinates defined above, un-primed are the manufacturer's coordinates). Once you no longer need these instructions, I would use the manufacturer's definitions, but for now, I thought it would be

clearest if  $x'$  mirrored  $x$  and  $z'$  mirrored  $z$ .

29. Turn on the piezo-controllers. Wait a moment and confirm that they 'jump' to their previous positions. Turn them all to 50 so you are near the center of their range.
30. Remove the front cover for the setup, and then put the top cover back in place. Mount the sample on a single-layer of carbon tape on the brass sample holder and slide it into the slot on the sample holder mount making sure that your sample will not hit the tips. Looking from above (consider un-flipping the parabolic mirror to see better), continue sliding the brass sample holder back until the fiber-tips are approximately aligned with the location of your waveguide-of-interest (WOI). This will require knowing approximately where on the sample your WOI is located.
31. Turn the SQUID light on. Find your device on the monitor by moving the camera micrometers. Since it is at an angle to the sample surface, you may need to move both the  $y$  and  $z$  micrometer simultaneously to move the area of the sample that is in focus without moving the sample's position in the image.
32. Turn on the Velocity laser. Note that the wavelength-tuning capability of this laser is gone, but it still serves as a fiber-coupled cw laser that can put enough IR light through these waveguides to be measured with the PrPM.
  - a. Flick the switch on the back-left of the Velocity Laser controller.
  - b. Wait about a minute for the temperature to reach about 20°C (read the temperature on the right).

- c. Turn the key.
  - d. Click the Laser-On button.
  - e. On the right, click on 'Display' button until 'Power' is selected.
  - f. Make sure 'Constant Power' is selected. If not, click the 'Mode' button once.
33. Move the left fiber-tip toward the sample until you can see it in the CCD camera. *Do not move the fiber-tip in the x- or z-directions yet, only toward the sample (y-direction).* Make sure not to crash the tip if it does not come into view, but as long as you have done Steps 30 and 31 correctly, this will not be a problem. Move it close to the sample but far enough away that it will not touch it even if it is below the sample surface, while following the fiber-tip to the sample with the CCD camera. Note that if you are too far from the sample, Step 35 will be impossible.
34. Connect the left fiber-tip to the Velocity laser. If you do not see light in the fiber-tip, re-visit Step 32.
35. Move the z-micrometer for the left fiber-tip up and down a couple times. You should see a flash as it passes the surface of the sample. Stop the z-micrometer mid-flash to the best of your ability. Now move the z-micrometer of the CCD until the fiber is in focus. If necessary, move the y-micrometer of the CCD camera in tandem to get the focal position on the monitor. Now the fiber-tip should be in focus as well as a portion of the sample that is right beside it. These are in the same plane. For the safety of the fiber-tip, back it away from the sample a little during Step 36.

36. Move the y-micrometer of the sample holder stage until your WOI is in aligned with the fiber-tip and in focus on the CCD (these should happen simultaneously). Moving this y-micrometer (rather than moving the one for the fiber-tip) will keep the two fiber-tips in line and make aligning the right-hand fiber-tip much easier than the left.
37. If you moved the sample a lot in Step 36, you may need to redo Step 35 since the surface of the sample may not be perfectly parallel to the table surface.
38. Since the left fiber-tip is aligned in z (Steps 34 and 36) and aligned in y (Step 35), now the only thing left to do is x. Since this is the most dangerous because you can crash the tip, only get as close to the sample as you feel comfortable right now. Hopefully, you will see a line of scattered light along the waveguide as you do this indicating you are properly coupled into the waveguide. If not, turn off the SQUID light and perhaps look at the right side of the sample and make small movements with the z and y micrometers. Look for flashes of light at the device, on the right-edge of the waveguide, at the lithography alignment markers, and along the first part of the waveguide (closest to the left fiber-tip).
39. Repeat Steps 33-35 for the right fiber-tip. You will need the blue patch-fiber and the butt-coupler for Step 34.
40. Repeat Step 36 for the right fiber-tip, except use the y-micrometer for the right fiber-tip, not the y-micrometer for the sample. However, you should not need to move the y-micrometer very much unless the waveguides are not very parallel to the fiber-tips (or they weren't the last time).

41. Repeat 37 and 38 for the right fiber-tip.
42. Connect the right fiber-tip to the PrPM and the left one to the Velocity laser.  

If you do not read any power, check Steps 32-41, making sure you can see scatter light from both configurations (left and right fiber-tips connected to Velocity laser). You can also turn up the power of the Velocity laser if necessary.
43. Optimize the power by moving the y and z piezo knobs for the left fiber-tip and the y' and z' knobs for the right fiber-tip (remember these are my coordinate definitions, not the manufacturers). You should not be reaching under a Post-It note yet.
44. Optimize the power for the x piezo knob for the right fiber-tip; now you should be reaching under a Post-It note. You will probably peg the knob, so be gentle. Once you peg it, note the power value and then return the knob to 50. Now you know that you are *probably* safe to move the x-micrometer until you see that power value again. If you jar the fiber-tip too much while moving it, this may not be true.
45. Re-optimize the y and z piezo knobs.
46. Repeat Steps 44 and 45 until you see a decrease in the power as you move the x piezo knob. The end-facet of the waveguide is now at the focal position of the lensed fiber-tip.
47. Repeat 44-46 for the right fiber-tip. Note this power maximum in your notebook.

48. Use a Sharpie to draw a circle on the monitor around the device. This will be used later, so try not to move the CCD camera after you have done this. These marks can be removed with the methanol near the KML laser.
49. Connect the left fiber-tip to the probe-coupler in the pump-probe portion of this setup and then the right fiber-tip to the detector on the lock-in amplifier (LIA). If necessary, hit the 'Auto-phase' button. Note this probe voltage value in your notebook.

#### **A.5. Align Pump Beam Spot on the Device**

50. Assuming everything is connected as it would be at the end of Procedure #3, change the 'Harmonic' to 2 on the LIA (under 'Ref Phase').
51. Rotate PuPol1 to get about 600 nJ/pulse of pump power in the PuPM. This should be enough to get a signal without damaging the device.
52. Block the probe and unblock the pump by flipping down the PuPM.
53. The beam should look closer to a tear-drop than a circle. Using the x- and y-micrometers of the parabolic mirror (M12) move the center of the beam spot to your Sharpie dot (see Step 46). Since it is tear-drop shaped, this needs a bit more explanation: the WOI should intersect the fattest part of the beam spot.
54. Using smaller movements of the M12 micrometers, maximize the LIA signal (the LIA needs to be set to readout the 2<sup>nd</sup> Harmonic of the reference frequency for this to work). Note that since you are using the chopper frequency as your LIA reference, the 2<sup>nd</sup> Harmonic frequency is actually the

laser repetition rate. You will probably want to re-press the ‘Auto-phase’ button once you get enough signal that the Auto-phase will work.

55. After you think you have found the device location with the beam spot, make sure you are still approximately near your Sharpie mark. Since you are only measuring the scattering of the pump beam into the waveguide, it is easy to accidentally align to another feature, light a defect in the waveguide or an alignment mark.
56. To make extra sure your pump beam is on the device check the contrast with a delay time greater than zero.
  - a. Turn the ‘Harmonic’ back to 1 and move the translation stage to a position of about +10 mm.
  - b. Unblock the probe, block the pump and ‘Auto-phase’. This should be the value you noted at the end of Procedure #3.
  - c. Now unblock/block the pump numerous times and see if the voltage is reduced whenever the pump is unblocked. If your device has a very transient signal, you may not notice a difference.

Note that sometimes, the device does not scatter much, and a process like Step 56 should be used to ‘find’ the device rather than the process described in Step 53-55. However, as noted in Step 56c, if you do not know where time-zero is, this will be difficult if not impossible. If that is the case, you might consider finding time-zero with an embedded-VO<sub>2</sub> device and assume it is the same for your device that does not scatter very much.

## A.6. Measurement

Depending upon which of the two measurement types is desired, there is a slightly different method to follow. For a pump-probe measurement perform Step 57 and all its substeps after setting the polarization angle manually. Since there is no method for setting the delay stage manually, that must be done with a short Labview program before using the *fluenceSweep.vi* program as outlined in Step 58 and 59 and their substeps. All of the Labview programs described here are to be run on the same laptop, the one on a stand above the piezo-controllers. Note that the Labview program used for a pump-probe measurement is found in Appendix B. All other Labview programs are simple enough that they can be examined on the laboratory laptop, with the exception of the *fluenceSweep.vi*. However, that Labview program is basically a duplicate of the *pumpProbeMeasurement.vi* but with the delay stage replaced with a rotational stage, so its reproduction here seemed unnecessary.

57. To make a pump probe sweep follow these procedures.

- a. Ensure that the LIA has the settings you want. A common mistake is to forget to change the time constant from 100 ms, used for alignment, back to about 1 second for measurements. Another common mistake is to leave the Harmonic Setting on the 2<sup>nd</sup> harmonic of the reference frequency, which will record the pump signal rather than the probe.
- b. Open the Labview program *setDelayStageParams.vi* and use the default settings. This tells the delay stage not to move in such a jarring manner, prevents the fiber-tips from shaking. Close this program as you only need it when reinitializing the setup.

- c. Open the Labview program *pumpProbeMeasurement.vi* and set your desired parameters. Note that there are a number of features that you may not want to use. For example, for a simple measurement, you probably only want 1 sweep of the delay stage. Since there two stages of movement, you can use two different step sizes, such as 0.01 mm near time-zero and 0.5 mm to see longer dynamics.
  - d. Press the arrow key in the upper left-hand corner and wait for it to run. If you need to stop it early, press the both of the two Stop buttons and wait for two more measurements to run. Using this method, rather than the red X in the upper left-hand corner, prevents a loss of communications between the equipment and the laptop.
58. After setting the desired parameters in the *fluenceSweep.vi* Front Panel, click the ‘Prompt At Each Position Boolean’ to True. Then run the measurement once, with the pump beam blocked by the PuPM. At each position, measure the pump pulse energy and record it in a data file before clicking ‘Move Onto Next Position’ in the message box. The message box will prevent the Labview program from proceeding while you collect this pump power calibration data.
59. Re-run the program with the pump unblocked. After it is finished, a pump power and a device response are correlated to each polarizer angle, eliminating the need for that variable.
60. To perform a scattering knife-edge measurement, like the one discussed in section 6.3.1, use the ‘Prompt At Each Position Boolean’ in the *pumpProbeMeasurement.vi* to allow yourself time to move one of the two

micrometers for the parabolic mirror. Unlike in Steps 58, the record LIA value will be your data, but you must keep track of the micrometer positions on your own. Note that those micrometers positions are in inches.

## APPENDIX B

### LABVIEW PROGRAM FOR OUT-OF-PLANE, IN-WAVEGUIDE PUMP-PROBE OPTICAL SETUP

This appendix contains the Labview program used to run the pump-probe setup shown in Figure 6.7 and Figure A.1. All other Labview programs are simple enough that they can be examined on the laboratory laptop, with the exception of the *fluenceSweep.vi*. However, that Labview program is basically a duplicate of the *pumpProbeMeasurement.vi* outlined below, but with the delay stage replaced with a rotational stage, so its reproduction here seemed unnecessary.

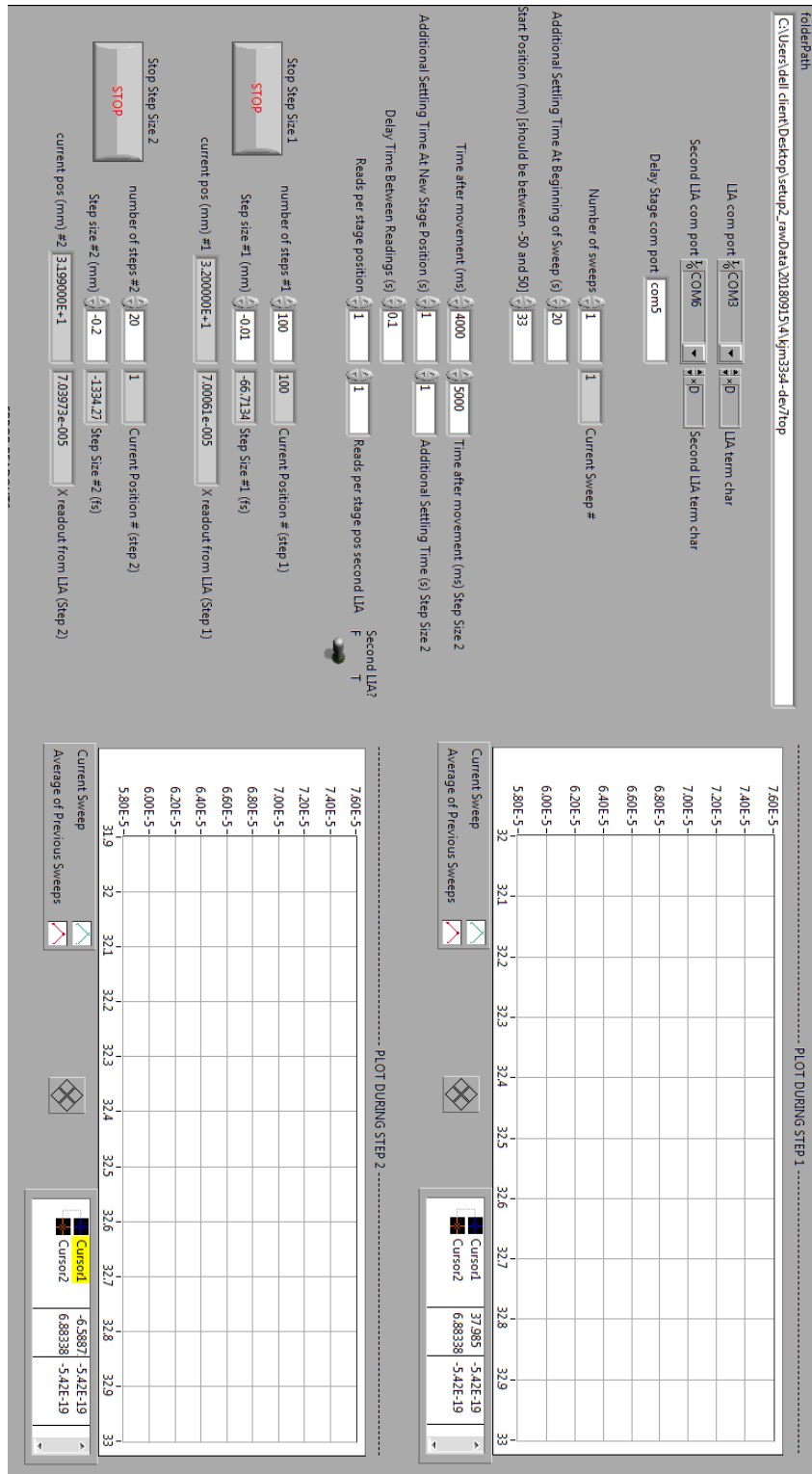


Figure B.1. Front Panel for the Labview program used to run the pump-probe setup shown in Figure 6.7 and A.1.

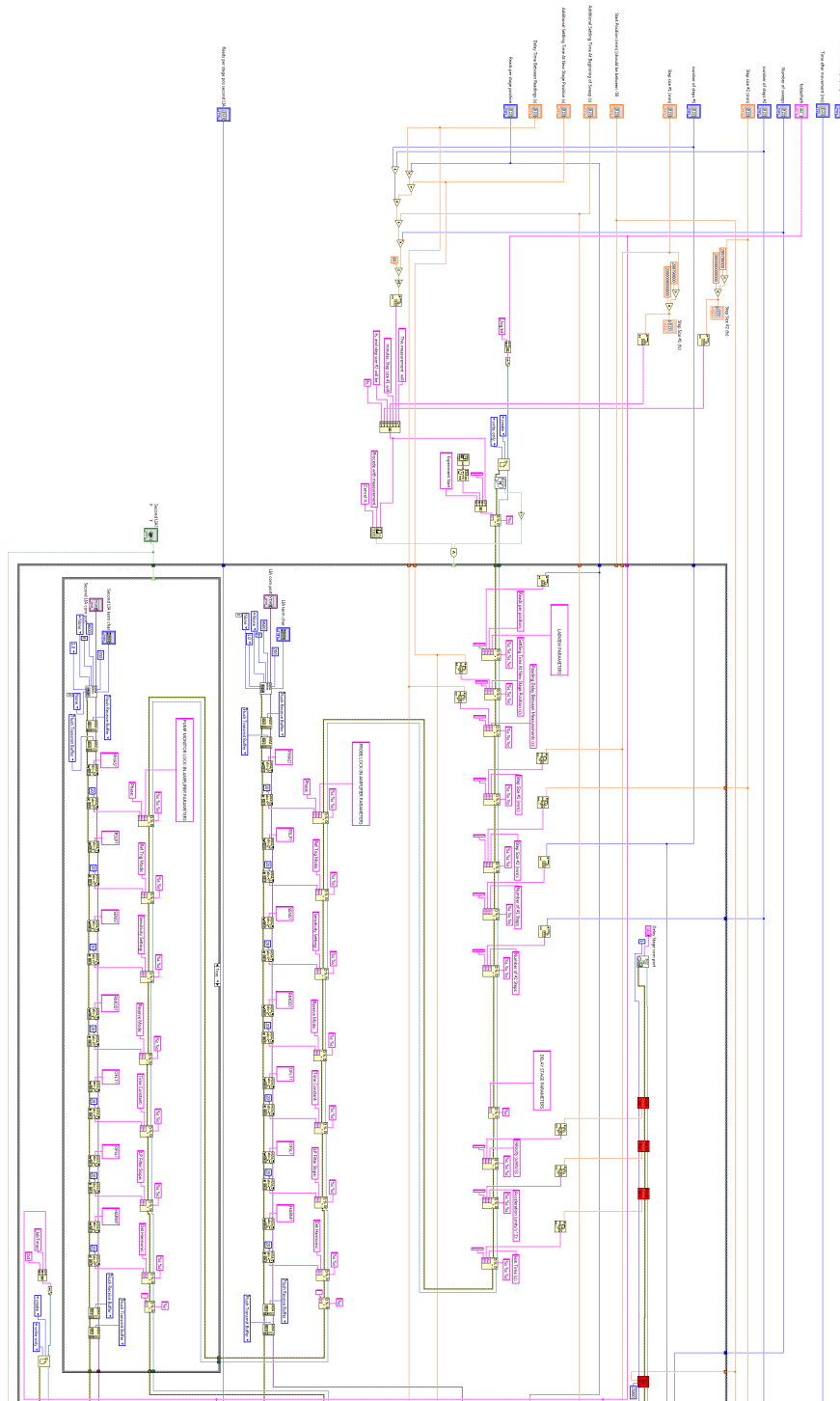


Figure B.2. Left half of the Block Diagram for the Labview program used to run the pump-probe setup shown in Figure 6.7 and A.1.

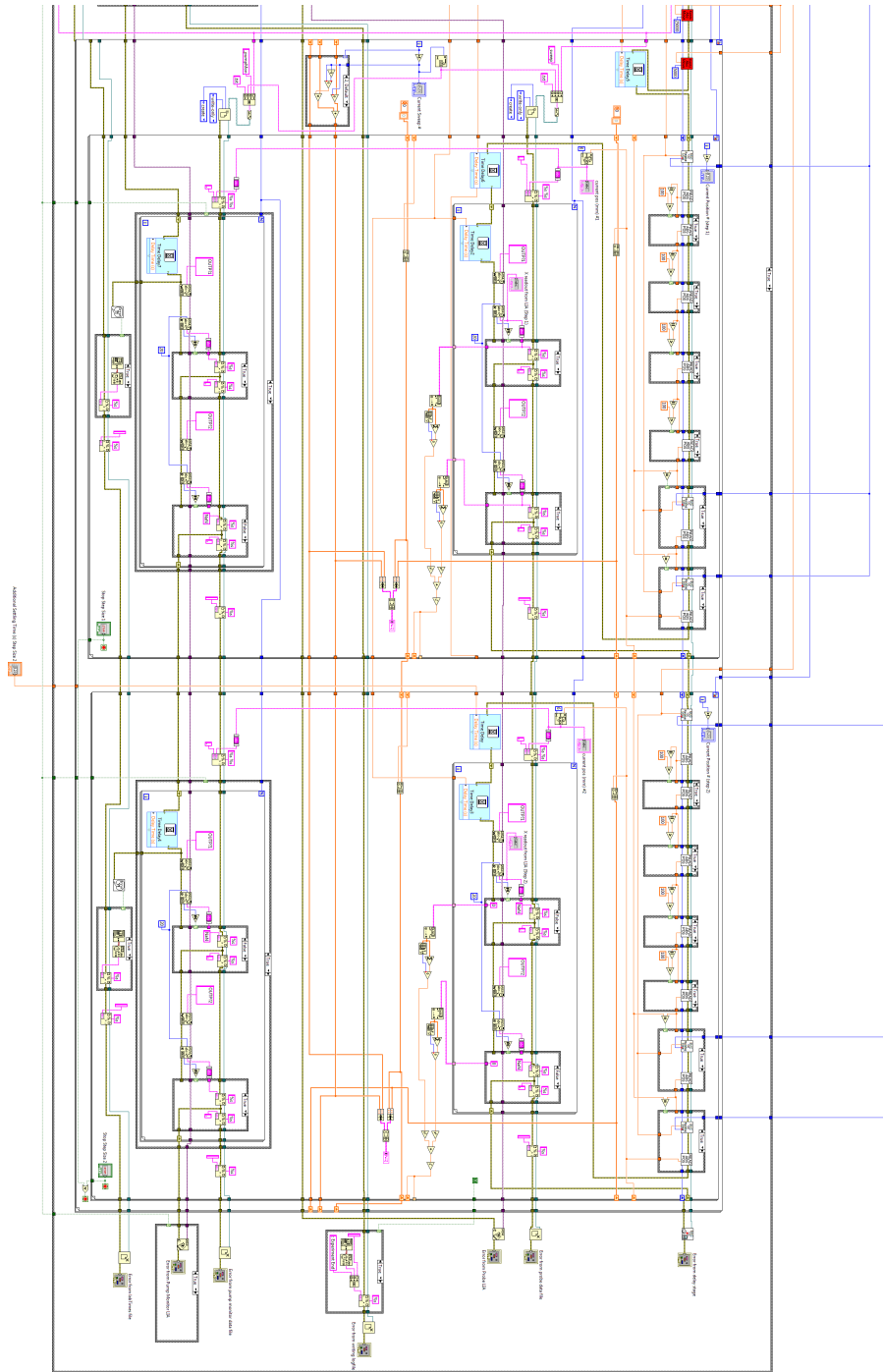


Figure B.3. Right half of the Block Diagram for the Labview program used to run the pump-probe setup shown in Figure 6.7 and A.1. There is slight overlap of the right and left-hand images for clarity.

## BIBLIOGRAPHY

1. K. Saitoh and S. Matsuo, "Multicore fiber technology," *J. Light. Technol.* **34**(1), 55–66 (2016).
2. G. T. Reed, G. Mashanovich, F. Y. Gardes, and D. J. Thomson, "Silicon optical modulators," *Nat. Photonics* **4**(8), 518–526 (2010).
3. W. Li, B. Chen, C. Meng, W. Fang, Y. Xiao, X. Li, Z. Hu, Y. Xu, L. Tong, H. Wang, W. Liu, J. Bao, and Y. R. Shen, "Ultrafast all-optical graphene modulator," *Nano Lett.* **14**(2), 955–959 (2014).
4. S. Yang, D. C. Liu, Z. L. Tan, K. Liu, Z. H. Zhu, and S. Q. Qin, "CMOS-Compatible WS<sub>2</sub>-Based All-Optical Modulator," *ACS Photonics* **5**(2), 342–346 (2018).
5. Y. Wang, F. Zhang, X. Tang, X. Chen, Y. Chen, W. Huang, Z. Liang, L. Wu, Y. Ge, Y. Song, J. Liu, D. Zhang, J. Li, and H. Zhang, "All-Optical Phosphorene Phase Modulator with Enhanced Stability Under Ambient Conditions," *Laser Photonics Rev.* **12**(6), 1–9 (2018).
6. J. Zheng, Z. Yang, C. Si, Z. Liang, X. Chen, R. Cao, Z. Guo, K. Wang, Y. Zhang, J. Ji, M. Zhang, D. Fan, and H. Zhang, "Black Phosphorus Based All-Optical-Signal-Processing: Toward High Performances and Enhanced Stability," *ACS Photonics* **4**(6), 1466–1476 (2017).
7. Z. Chai, X. Hu, F. Wang, C. Li, Y. Ao, Y. Wu, K. Shi, H. Yang, and Q. Gong, "Ultrafast on-Chip Remotely-Triggered All-Optical Switching Based on Epsilon-Near-Zero Nanocomposites," *Laser Photonics Rev.* **11**(5), 1–8 (2017).
8. P. Geiregat, A. J. Houtepen, D. Van Thourhout, and Z. Hens, "All-optical wavelength conversion by picosecond burst absorption in colloidal PbS quantum dots," *ACS Nano* **10**(1), 1265–1272 (2016).
9. F. Zhou and W. Du, "Ultrafast all-optical plasmonic graphene modulator," *Appl. Opt.* **57**(23), 6645 (2018).
10. Y. Liao, G. Feng, H. Zhou, J. Mo, H. J. Sun, and S. H. Zhou, "Ultra-broadband all-optical graphene modulator," *IEEE Photonics Technol. Lett.* **30**(8), 661–664 (2018).
11. F. Sun, L. Xia, C. Nie, J. Shen, Y. Zou, G. Cheng, H. Wu, Y. Zhang, D. Wei, S. Yin, and C. Du, "The all-optical modulator in dielectric-loaded waveguide with graphene-silicon heterojunction structure," *Nanotechnology* **29**(13), (2018).
12. S. Luo, Y. Wang, X. Tong, and Z. Wang, "Graphene-based optical modulators," *Nanoscale Res. Lett.* **10**(1), 199 (2015).
13. X. He, M. Xu, and X. Zhang, "Theoretical investigation of a broadband all-optical

- graphene-microfiber modulator," *J. Opt. Soc. Am. B* **33**(12), 2588 (2016).
14. H. Zhang, N. Healy, L. Shen, C. C. Huang, D. W. Hewak, and A. C. Peacock, "Enhanced all-optical modulation in a graphene-coated fibre with low insertion loss," *Sci. Rep.* **6**(March), 2–6 (2016).
  15. V. Eyert, "The metal-insulator transitions of VO<sub>2</sub>: A band theoretical approach," *Ann. Phys.* **11**(9), 650–704 (2002).
  16. K. Martens, I. P. Radu, S. Mertens, X. Shi, L. Nyns, S. Cosemans, P. Favia, H. Bender, T. Conard, M. Schaekers, S. De Gendt, V. Afanas'ev, J. A. Kittl, M. Heyns, and M. Jurczak, "The VO<sub>2</sub> interface, the metal-insulator transition tunnel junction, and the metal-insulator transition switch On-Off resistance," *J. Appl. Phys.* **112**(12), 124501 (2012).
  17. M. J. Lee, Y. Park, D. S. Suh, E. H. Lee, S. Seo, D. C. Kim, R. Jung, B. S. Kang, S. E. Ahn, C. B. Lee, D. H. Seo, Y. K. Cha, I. K. Yoo, J. S. Kim, and B. H. Park, "Two series oxide resistors applicable to high speed and high density nonvolatile memory," *Adv. Mater.* **19**(22), 3919–3923 (2007).
  18. M. Son, J. Lee, J. Park, J. Shin, G. Choi, S. Jung, W. Lee, S. Kim, S. Park, and H. Hwang, "Excellent selector characteristics of nanoscale VO<sub>2</sub> for high-density bipolar ReRAM applications," *IEEE Electron Device Lett.* **32**(11), 1579–1581 (2011).
  19. C. R. Cho, S. Cho, S. Vadim, R. Jung, and I. Yoo, "Current-induced metal-insulator transition in VO<sub>x</sub> thin film prepared by rapid-thermal-annealing," *Thin Solid Films* **495**(1–2), 375–379 (2006).
  20. S. Chen, H. Ma, X. Yi, T. Xiong, H. Wang, and C. Ke, "Smart VO<sub>2</sub> thin film for protection of sensitive infrared detectors from strong laser radiation," *Sensors Actuators A* **115**(1), 28–31 (2004).
  21. R. Lopez, R. F. Haglund, L. C. Feldman, L. A. Boatner, and T. E. Haynes, "Optical nonlinearities in VO<sub>2</sub> nanoparticles and thin films," *Appl. Phys. Lett.* **85**(22), 5191–5193 (2004).
  22. M. Maaza, D. Hamidi, A. Simo, T. Kerdja, A. K. Chaudhary, and J. B. Kana Kana, "Optical limiting in pulsed laser deposited VO<sub>2</sub> nanostructures," *Opt. Commun.* **285**(6), 1190–1193 (2012).
  23. W. Wang, Y. Luo, D. Zhang, and F. Luo, "Dynamic optical limiting experiments on vanadium dioxide and vanadium pentoxide thin films irradiated by a laser beam," *Appl. Opt.* **45**(14), 3378 (2006).
  24. J. Zhou, Y. Gao, Z. Zhang, H. Luo, C. Cao, Z. Chen, L. Dai, and X. Liu, "VO<sub>2</sub> thermochromic smart window for energy savings and generation," *Sci. Rep.* **3**, 1–5 (2013).
  25. S. Y. Li, G. A. Niklasson, and C. G. Granqvist, "Thermochromic fenestration with

- VO<sub>2</sub>-based materials: Three challenges and how they can be met," *Thin Solid Films* **520**(10), 3823–3828 (2012).
26. P. Kiri, M. E. A. Warwick, I. Ridley, and R. Binions, "Fluorine doped vanadium dioxide thin films for smart windows," *Thin Solid Films* **520**(4), 1363–1366 (2011).
  27. C. Batista, R. M. Ribeiro, and V. Teixeira, "Synthesis and characterization of VO<sub>2</sub>-based thermochromic thin films for energy-efficient windows.," *Nanoscale Res. Lett.* **6**(1), 301 (2011).
  28. T. Paik, S. Hong, E. A. Gaulding, H. Caglayan, T. R. Gordon, N. Engheta, C. R. Kagan, and C. B. Murray, "Solution-processed phase-change VO<sub>2</sub> metamaterials from colloidal vanadium oxide (VO<sub>x</sub>) nanocrystals.," *ACS Nano* **8**(1), 797–806 (2014).
  29. K. Appavoo and R. F. Haglund, "Detecting nanoscale size dependence in VO<sub>2</sub> phase transition using a split-ring resonator metamaterial.," *Nano Lett.* **11**(3), 1025–31 (2011).
  30. M. J. Dicken, K. Aydin, I. M. Pryce, L. A. Sweatlock, E. M. Boyd, S. Walavalkar, J. Ma, and H. A. Atwater, "Frequency tunable near-infrared metamaterials based on VO<sub>2</sub> phase transition," *Opt. Express* **17**(20), 18330–18339 (2009).
  31. T. Driscoll, H.-T. Kim, B.-G. Chae, B.-J. Kim, Y.-W. Lee, N. M. Jokerst, S. Palit, D. R. Smith, M. Di Ventra, and D. N. Basov, "Memory metamaterials," *Science* **325**(5947), 1518–1521 (2009).
  32. L. A. Ladd and W. Paul, "Optical and transport properties of high quality crystals of V<sub>2</sub>O<sub>4</sub> near the metallic transition temperature," *Solid State Commun.* **7**(4), 425–428 (1969).
  33. J. B. Kana Kana, J. M. Ndjaka, G. Vignaud, A. Gibaud, and M. Maaza, "Thermally tunable optical constants of vanadium dioxide thin films measured by spectroscopic ellipsometry," *Opt. Commun.* **284**(3), 807–812 (2011).
  34. E. Strelcov, A. Tselev, I. Ivanov, J. D. Budai, J. Zhang, J. Z. Tischler, I. Kravchenko, S. V Kalinin, and A. Kolmakov, "Doping-based stabilization of the M2 phase in free-standing VO<sub>2</sub> nanostructures at room temperature," *Nano Lett.* **12**(12), 6198–205 (2012).
  35. W. R. Roach and I. Balberg, "Optical induction and detection of fast phase transition in VO<sub>2</sub>," *Solid State Commun.* **9**(9), 551–555 (1971).
  36. A. A. Bugaev, V. V. Gudyalis, B. P. Zakharchenya, and F. A. Chudnovskii, "Selectivity of the photoexcited metal-semiconductor phase transition in vanadium dioxide initiated by picosecond pulses," *JETP Lett.* **34**(8), 430–433 (1982).
  37. Z. Tao, F. Zhou, T. R. T. Han, D. Torres, T. Wang, N. Sepulveda, K. Chang, M. Young, R. R. Lunt, and C. Y. Ruan, "The nature of photoinduced phase transition

- and metastable states in vanadium dioxide," *Sci. Rep.* **6**(December), 1–10 (2016).
38. T. Cocker, L. Titova, S. Fourmaux, G. Holloway, H.-C. Bandulet, D. Brassard, J.-C. Kieffer, M. El Khakani, and F. Hegmann, "Phase diagram of the ultrafast photoinduced insulator-metal transition in vanadium dioxide," *Phys. Rev. B* **85**(15), 155120 (2012).
  39. A. Cavalleri, T. Dekorsy, H. Chong, J. Kieffer, and R. Schoenlein, "Evidence for a structurally-driven insulator-to-metal transition in VO<sub>2</sub>: A view from the ultrafast timescale," *Phys. Rev. B* **70**(16), 161102 (2004).
  40. M. F. Jager, C. Ott, P. M. Kraus, C. J. Kaplan, W. Pouse, R. E. Marvel, R. F. Haglund, D. M. Neumark, and S. R. Leone, "Tracking the insulator-to-metal phase transition in VO<sub>2</sub> with few-femtosecond extreme UV transient absorption spectroscopy," *Proc. Natl. Acad. Sci.* **114**(36), 9558–9563 (2017).
  41. V. R. Morrison, R. P. Chatelain, K. L. Tiwari, A. Hendaoui, A. Bruhacs, M. Chaker, and B. J. Siwick, "A photoinduced metal-like phase of monoclinic VO<sub>2</sub> revealed by ultrafast electron diffraction," *Science* **346**(6208), 445–448 (2014).
  42. Z. Tao, T.-R. Han, S. Mahanti, P. Duxbury, F. Yuan, C.-Y. Ruan, K. Wang, and J. Wu, "Decoupling of Structural and Electronic Phase Transitions in VO<sub>2</sub>," *Phys. Rev. Lett.* **109**(16), 1–5 (2012).
  43. J. Nag, R. F. Haglund, E. Andrew Payzant, and K. L. More, "Non-congruence of thermally driven structural and electronic transitions in VO<sub>2</sub>," *J. Appl. Phys.* **112**(10), 103532 (2012).
  44. D. Wegkamp, M. Herzog, L. Xian, M. Gatti, P. Cudazzo, C. L. McGahan, R. E. Marvel, R. F. Haglund, A. Rubio, M. Wolf, and J. Stähler, "Instantaneous Band Gap Collapse in Photoexcited Monoclinic VO<sub>2</sub> due to Photocarrier Doping," *Phys. Rev. Lett.* **113**(21), 216401 (2014).
  45. D. Wegkamp and J. Stähler, "Ultrafast dynamics during the photoinduced phase transition in VO<sub>2</sub>," *Prog. Surf. Sci.* **90**(4), 464–502 (2015).
  46. S. Wall, D. Wegkamp, L. Foglia, K. Appavoo, J. Nag, R. F. Haglund, J. Stähler, and M. Wolf, "Ultrafast changes in lattice symmetry probed by coherent phonons," *Nat. Commun.* **3**, 721 (2012).
  47. N. F. Brady, K. Appavoo, M. Seo, J. Nag, R. P. Prasankumar, R. F. Haglund, and D. J. Hilton, "Heterogeneous nucleation and growth dynamics in the light-induced phase transition in vanadium dioxide," *J. Phys. Condens. Matter* **28**(12), 125603 (2016).
  48. R. E. Marvel, R. R. Harl, V. Craciun, B. R. Rogers, and R. F. Haglund, "Influence of deposition process and substrate on the phase transition of vanadium dioxide thin films," *Acta Mater.* **91**, 217–226 (2015).

49. J. Nag, "The Solid-Solid Phase Transition in Vanadium Dioxide Thin Films: Synthesis, Physics and Application," Dissertation (2011).
50. S. Xu, X. Shen, K. A. Hallman, R. F. Haglund, and S. T. Pantelides, "Unified band-theoretic description of structural, electronic, and magnetic properties of vanadium dioxide phases," *Phys. Rev. B* **95**(12), 1–7 (2017).
51. J. P. Pouget, H. Launois, J. P. D’Haenens, P. Merenda, and T. M. Rice, "Electron Localization Induced by Uniaxial Stress in Pure VO<sub>2</sub>," *Phys. Rev. Lett.* **35**(13), 873–875 (1975).
52. J. Pouget, H. Launois, T. Rice, P. Dernier, A. Gossard, G. Villeneuve, and P. Hagenmuller, "Dimerization of a linear Heisenberg chain in the insulating phases of V<sub>1-x</sub>Cr<sub>x</sub>O<sub>2</sub>," *Phys. Rev. B* **10**(5), 1801–1815 (1974).
53. H.-T. Kim, Y. W. Lee, B.-J. Kim, B.-G. Chae, S. J. Yun, K.-Y. Kang, K.-J. Han, K.-J. Yee, and Y.-S. Lim, "Monoclinic and Correlated Metal Phase in VO<sub>2</sub> as Evidence of the Mott Transition: Coherent Phonon Analysis," *Phys. Rev. Lett.* **97**(26), 266401 (2006).
54. H.-T. Kim, B.-G. Chae, D.-H. Youn, S.-L. Maeng, G. Kim, K.-Y. Kang, and Y.-S. Lim, "Mechanism and observation of Mott transition in VO<sub>2</sub>-based two- and three-terminal devices," *New J. Phys.* **6**, 52–52 (2004).
55. J. Goodenough, "The two components of the crystallographic transition in VO<sub>2</sub>," *J. Solid State Chem.* **3**, 490–500 (1971).
56. A. Zylbersztejn and N. F. Mott, "Metal-insulator transition in vanadium dioxide," *Phys. Rev. B* **11**(11), 4383–4395 (1975).
57. T. M. Rice, H. Launois, and J. P. Pouget, "Comment on “VO<sub>2</sub>: Peierls or Mott-Hubbard? A View from Band Theory,”" *Phys. Rev. Lett.* **73**(22), 3042–3042 (1994).
58. R. M. Wentzcovitch, "VO<sub>2</sub>: Peierls or Mott-Hubbard? A view from band theory," *Phys. Rev. Lett.* **72**(21), 3389–3392 (1994).
59. R. Wentzcovitch, W. Schulz, and P. Allen, "Wentzcovitch et al. Reply," *Phys. Rev. Lett.* **73**(22), 3043–3043 (1994).
60. S. Biermann, A. Poteryaev, A. Lichtenstein, and A. Georges, "Dynamical Singlets and Correlation-Assisted Peierls Transition in VO<sub>2</sub>," *Phys. Rev. Lett.* **94**(2), 026404 (2005).
61. C. Weber, D. O’Regan, N. Hine, M. Payne, G. Kotliar, and P. Littlewood, "Vanadium Dioxide: A Peierls-Mott Insulator Stable against Disorder," *Phys. Rev. Lett.* **108**(25), 256402 (2012).
62. M. Gatti, F. Bruneval, V. Olevano, and L. Reining, "Understanding Correlations in Vanadium Dioxide from First Principles," *Phys. Rev. Lett.* **99**(26), 266402 (2007).

63. L. Hedin, "New Method for Calculating the One-Particle Green's Function with Application to the Electron-Gas Problem," *Phys. Rev.* **139**(3A), A796–A823 (1965).
64. V. Eyert, "VO<sub>2</sub>: A Novel View from Band Theory," *Phys. Rev. Lett.* **107**(1), 016401 (2011).
65. R. Grau-Crespo, H. Wang, and U. Schwingenschlögl, "Why the Heyd-Scuseria-Ernzerhof hybrid functional description of VO<sub>2</sub> phases is not correct," *Phys. Rev. B* **86**(8), 081101 (2012).
66. B. Xiao, J. Sun, A. Ruzsinszky, and J. P. Perdew, "Testing the Jacob's ladder of density functionals for electronic structure and magnetism of rutile VO<sub>2</sub>," *Phys. Rev. B* **90**(8), 085134 (2014).
67. X. Yuan, Y. Zhang, T. Abtew, P. Zhang, and W. Zhang, "VO<sub>2</sub>: Orbital competition, magnetism, and phase stability," *Phys. Rev. B* **86**(23), 235103 (2012).
68. G. Kresse and D. Joubert, "From ultrasoft pseudopotentials to the projector augmented-wave method," *Phys. Rev. B* **59**(3), 1758–1775 (1999).
69. G. Kresse and J. Furthmüller, "Efficient iterative schemes for ab initio total-energy calculations using a plane-wave basis set," *Phys. Rev. B* **54**(16), 11169–11186 (1996).
70. J. P. Perdew, M. Ernzerhof, and K. Burke, "Rationale for mixing exact exchange with density functional approximations," *J. Chem. Phys.* **105**, 9982 (1996).
71. C. Adamo and V. Barone, "Toward reliable density functional methods without adjustable parameters: The PBE0 model," *J. Chem. Phys.* **110**(13), 6158 (1999).
72. J. B. Goodenough, "Theory of the role of covalence in the perovskite-type manganites [La<sub>x</sub>M(II)]MnO<sub>3</sub>," *Phys. Rev.* **100**(2), 564–573 (1955).
73. J. B. Goodenough, "An interpretation of the magnetic properties of the perovskite-type mixed crystals La<sub>1-x</sub>Sr<sub>x</sub>CoO<sub>3-λ</sub>," *J. Phys. Chem. Solids* **6**(2–3), 287–297 (1958).
74. D. B. McWhan, M. Marezio, J. P. Remeika, and P. D. Dernier, "X-ray diffraction study of metallic VO<sub>2</sub>," *Phys. Rev. B* **10**(2), 490–495 (1974).
75. M. Marezio, D. McWhan, J. Remeika, and P. Dernier, "Structural Aspects of the Metal-Insulator Transitions in Cr-Doped VO<sub>2</sub>," *Phys. Rev. B* **5**(7), 2541–2551 (1972).
76. T. Yao, X. Zhang, Z. Sun, S. Liu, Y. Huang, Y. Xie, C. Wu, X. Yuan, W. Zhang, Z. Wu, G. Pan, F. Hu, L. Wu, Q. Liu, and S. Wei, "Understanding the Nature of the Kinetic Process in a VO<sub>2</sub> Metal-Insulator Transition," *Phys. Rev. Lett.* **105**(22), 226405 (2010).
77. J. M. Longo, P. Kierkegaard, C. J. Ballhausen, U. Ragnarsson, S. E. Rasmussen, E. Sunde, and N. A. Sørensen, "A Refinement of the Structure of VO<sub>2</sub>," *Acta Chem.*

- Scand. **24**, 420–426 (1970).
78. K. Kosuge, "The Phase Transition in VO<sub>2</sub>," J. Phys. Soc. Japan **22**(2), 551–557 (1967).
  79. C. N. Berglund and H. J. Guggenheim, "Electronic Properties of VO<sub>2</sub> near the Semiconductor-Metal Transition," Phys. Rev. **185**(3), 1022–1033 (1969).
  80. H. Wang, T. A. Mellan, R. Grau-Crespo, and U. Schwingenschlögl, "Spin polarization, orbital occupation and band gap opening in vanadium dioxide: The effect of screened Hartree–Fock exchange," Chem. Phys. Lett. **608**, 126–129 (2014).
  81. T. C. Koethe, Z. Hu, M. W. Haverkort, C. Schüßler-Langeheine, F. Venturini, N. B. Brookes, O. Tjernberg, W. Reichelt, H. H. Hsieh, H.-J. Lin, C. T. Chen, and L. H. Tjeng, "Transfer of Spectral Weight and Symmetry across the Metal-Insulator Transition in VO<sub>2</sub>," Phys. Rev. Lett. **97**(11), 116402 (2006).
  82. R. Molaie, R. Bayati, S. Nori, D. Kumar, J. T. Prater, and J. Narayan, "Diamagnetic to ferromagnetic switching in VO<sub>2</sub> epitaxial thin films by nanosecond excimer laser treatment," Appl. Phys. Lett. **103**(2), 2109 (2013).
  83. T. Kong, M. W. Masters, S. L. Bud'ko, and P. C. Canfield, "Physical properties of V<sub>1-x</sub>Ti<sub>x</sub>O<sub>2</sub> (0<x<0.187) single crystals," APL Mater. **3**(4), 041502 (2015).
  84. A. Cavalleri, M. Rini, H. Chong, S. Fourmaux, T. Glover, P. Heimann, J. Kieffer, and R. Schoenlein, "Band-Selective Measurements of Electron Dynamics in VO<sub>2</sub> Using Femtosecond Near-Edge X-Ray Absorption," Phys. Rev. Lett. **95**(6), 067405 (2005).
  85. K. Kosuge, Y. Ueda, S. Kachi, T. Shinjo, T. Takada, and M. Takano, "Magnetic properties of Fe<sub>x</sub>V<sub>1-x</sub>O<sub>2</sub> (0<x<0.05)," J. Solid State Chem. **23**(1–2), 105–113 (1978).
  86. P. Pouget, P. Lederer, D. Schreiber, H. Launois, D. Wohlleben, A. Casalot, and G. Villeneuve, "Contribution to the Study of the Metal-Insulator Transition in the V<sub>1-x</sub>Nb<sub>x</sub>O<sub>2</sub> System-II: Magnetic Properties," J. Phys. Chem. Solids **33**(10), 1961–1967 (1972).
  87. I. I. Mazin, D. J. Singh, and C. Ambrosch-Draxl, "Transport, optical, and electronic properties of the half-metal CrO<sub>2</sub>," Phys. Rev. B **59**(1), 411–418 (1999).
  88. K. Okimura, N. Hanis Azhan, T. Hajiri, S. Kimura, M. Zaghrioui, and J. Sakai, "Temperature-dependent Raman and ultraviolet photoelectron spectroscopy studies on phase transition behavior of VO<sub>2</sub> films with M1 and M2 phases," J. Appl. Phys. **115**(15), 153501 (2014).
  89. E. Arcangeletti, L. Baldassarre, D. Di Castro, S. Lupi, L. Malavasi, C. Marini, A. Perucchi, and P. Postorino, "Evidence of a Pressure-Induced Metallization Process in Monoclinic VO<sub>2</sub>," Phys. Rev. Lett. **98**(19), 196406 (2007).
  90. J. H. Park, J. M. Coy, T. S. Kasirga, C. Huang, Z. Fei, S. Hunter, and D. H. Cobden,

- "Measurement of a solid-state triple point at the metal-insulator transition in VO<sub>2</sub>," Nature **500**(7463), 431–4 (2013).
91. H. Guo, K. Chen, Y. Oh, K. Wang, C. Dejoie, S. a Syed Asif, O. L. Warren, Z. W. Shan, J. Wu, and a M. Minor, "Mechanics and Dynamics of the Strain-Induced M1–M2 Structural Phase Transition in Individual VO<sub>2</sub> Nanowires," Nano Lett. **11**(8), 3207–3213 (2011).
  92. E. O. Wollan and W. C. Koehler, "Neutron Diffraction Study of the Magnetic Properties of the Series of Perovskite-Type Compounds [(1-x)La, xCa]MnO<sub>3</sub>," Phys. Rev. **100**(2), 545–563 (1955).
  93. J. Goodenough and H. Hong, "Structures and a Two-Band Model for the System V<sub>1-x</sub>Cr<sub>x</sub>O<sub>2</sub>," Phys. Rev. B **8**(4), 1323–1331 (1973).
  94. M. Rohlfing and S. G. Louie, "Electron-Hole Excitations in Semiconductors and Insulators," Phys. Rev. Lett. **81**(11), 2312–2315 (1998).
  95. F. J. Nelson, J.-C. Idrobo, J. D. Fite, Z. L. Mišković, S. J. Pennycook, S. T. Pantelides, J. U. Lee, and A. C. Diebold, "Electronic Excitations in Graphene in the 1–50 eV Range: The  $\pi$  and  $\pi + \sigma$  Peaks Are Not Plasmons," Nano Lett. **14**(7), 3827–3831 (2014).
  96. M. A. Korotin, N. A. Skorikov, and V. I. Anisimov, "Variation of Orbital Symmetry of the Localized 3d<sup>1</sup> Electron of the V<sup>4+</sup> Ion upon the Metal-Insulator Transition in VO<sub>2</sub>," Phys. Met. Met. **94**(1), 17–23 (2002).
  97. A. Liebsch, H. Ishida, and G. Bihlmayer, "Coulomb correlations and orbital polarization in the metal-insulator transition of VO<sub>2</sub>," Phys. Rev. B **71**(8), 085109 (2005).
  98. F. J. Morin, "Oxides which show a metal-to-insulator transition at the Neel temperature," Phys. Rev. Lett. **3**(1), 34–36 (1959).
  99. L. Vidas, C. M. Günther, T. A. Miller, B. Pfau, D. Perez-Salinas, E. Martínez, M. Schneider, E. Gührs, P. Gargiani, M. Valvidares, R. E. Marvel, K. A. Hallman, R. F. Haglund, S. Eisebitt, and S. Wall, "Imaging Nanometer Phase Coexistence at Defects during the Insulator-Metal Phase Transformation in VO<sub>2</sub> Thin Films by Resonant Soft X-ray Holography," Nano Lett. **18**(6), 3449–3453 (2018).
  100. E. G. Linder and K. G. Hernqvist, "Space-charge effects in electron beams and their reduction by positive ion trapping," J. Appl. Phys. **21**(11), 1088–1097 (1950).
  101. W. E. and J. S. Eisebitt, S., Lüning, J., W. F. Schlotter, O. Hellwig, "Lensless imaging of magnetic nanostructures by X-ray," Nature **432**(December), 885–888 (2004).
  102. J. Laverock, S. Kittiwatanakul, A. A. Zakharov, Y. R. Niu, B. Chen, S. A. Wolf, J. W. Lu, and K. E. Smith, "Direct Observation of Decoupled Structural and Electronic

- Transitions and an Ambient Pressure Monocliniclike Metallic Phase of VO<sub>2</sub>," *Phys. Rev. Lett.* **113**(21), 216402 (2014).
103. A. X. Gray, J. Jeong, N. P. Aetukuri, P. Granitzka, Z. Chen, R. Kukreja, D. Higley, T. Chase, A. H. Reid, H. Ohldag, M. A. Marcus, A. Scholl, A. T. Young, A. Doran, C. A. Jenkins, P. Shafer, E. Arenholz, M. G. Samant, S. S. P. Parkin, and H. A. Dürr, "Correlation-Driven Insulator-Metal Transition in Near-Ideal Vanadium Dioxide Films," *Phys. Rev. Lett.* **116**(11), 1–6 (2016).
  104. S. H. Kim, B. J. Kim, T. Y. Jeong, Y. S. Lee, and K. J. Yee, "Coherent phonon spectroscopy of the phase transition in VO<sub>2</sub> single crystals and thin films," *J. Appl. Phys.* **117**(16), 163107 (2015).
  105. M. W. Haverkort, Z. Hu, a. Tanaka, W. Reichelt, S. V. Streltsov, M. a. Korotin, V. I. Anisimov, H. H. Hsieh, H.-J. Lin, C. T. Chen, D. I. Khomskii, and L. H. Tjeng, "Orbital-Assisted Metal-Insulator Transition in VO<sub>2</sub>," *Phys. Rev. Lett.* **95**(19), 196404 (2005).
  106. N. F. Quackenbush, H. Paik, M. J. Wahila, S. Sallis, M. E. Holtz, X. Huang, A. Ganose, B. J. Morgan, D. O. Scanlon, Y. Gu, F. Xue, L. Q. Chen, G. E. Sterbinsky, C. Schlueter, T. L. Lee, J. C. Woicik, J. H. Guo, J. D. Brock, D. A. Muller, D. A. Arena, D. G. Schlom, and L. F. J. Piper, "Stability of the M2 phase of vanadium dioxide induced by coherent epitaxial strain," *Phys. Rev. B* **94**(8), 1–6 (2016).
  107. D. Ruzmetov, S. Senanayake, and S. Ramanathan, "X-ray absorption spectroscopy of vanadium dioxide thin films across the phase-transition boundary," *Phys. Rev. B* **75**(19), 195102 (2007).
  108. B. T. O'Callahan, A. C. Jones, J. Hyung Park, D. H. Cobden, J. M. Atkin, and M. B. Raschke, "Inhomogeneity of the ultrafast insulator-to-metal transition dynamics of VO<sub>2</sub>," *Nat. Commun.* **6**, 6849 (2015).
  109. J. D. Ryckman, K. A. Hallman, R. E. Marvel, R. F. Haglund, and S. M. Weiss, "Ultra-compact silicon photonic devices reconfigured by an optically induced semiconductor-to-metal transition," *Opt. Express* **21**(9), 10753 (2013).
  110. R. E. Marvel, K. Appavoo, B. K. Choi, J. Nag, and R. F. Haglund, "Electron-beam deposition of vanadium dioxide thin films," *Appl. Phys. A* **111**(3), 975–981 (2012).
  111. R. Briggs, I. Pryce, and H. Atwater, "Compact silicon photonic waveguide modulator based on the vanadium dioxide metal-insulator phase transition," *Opt. Express* **18**(11), 11192–11201 (2010).
  112. J. M. Choi, R. K. Lee, and a Yariv, "Control of critical coupling in a ring resonator-fiber configuration: application to wavelength-selective switching, modulation, amplification, and oscillation.," *Opt. Lett.* **26**(16), 1236–8 (2001).
  113. C. Kübler, H. Ehrke, R. Huber, R. Lopez, A. Halabica, R. Haglund, and A. Leitenstorfer, "Coherent Structural Dynamics and Electronic Correlations during an

- Ultrafast Insulator-to-Metal Phase Transition in VO<sub>2</sub>," *Phys. Rev. Lett.* **99**(11), 116401 (2007).
114. M. Liu, X. Yin, E. Ulin-Avila, B. Geng, T. Zentgraf, L. Ju, F. Wang, and X. Zhang, "A graphene-based broadband optical modulator," *Nature* **474**(7349), 64–67 (2011).
  115. T. K. Liang, L. R. Nunes, T. Sakamoto, K. Sasagawa, T. Kawanishi, and M. Tsuchiya, "Ultrafast all-optical switching by cross-absorption modulation in silicon wire waveguides," *Opt. Express* **13**(19), 7298–7303 (2005).
  116. A. Cavalleri, C. Tóth, C. Siders, J. Squier, F. Ráksi, P. Forget, and J. Kieffer, "Femtosecond Structural Dynamics in VO<sub>2</sub> during an Ultrafast Solid-Solid Phase Transition," *Phys. Rev. Lett.* **87**(23), 237401 (2001).
  117. M. M. Qazilbash, M. Brehm, B.-G. G. Chae, P.-C. Ho, G. O. Andreev, B.-J. J. Kim, S. J. Yun, a V Balatsky, M. B. Maple, F. Keilmann, H.-T. T. Kim, and D. N. Basov, "Mott transition in VO<sub>2</sub> revealed by infrared spectroscopy and nano-imaging.," *Science* **318**(5857), 1750–3 (2007).
  118. Q. Xu, B. Schmidt, S. Pradhan, and M. Lipson, "Micrometre-scale silicon electro-optic modulator," *Nature* **435**(7040), 325–7 (2005).
  119. D.-W. Oh, C. Ko, S. Ramanathan, and D. G. Cahill, "Thermal conductivity and dynamic heat capacity across the metal-insulator transition in thin film VO<sub>2</sub>," *Appl. Phys. Lett.* **96**(15), 151906 (2010).
  120. A. Pashkin, C. Kübler, H. Ehrke, R. Lopez, A. Halabica, R. Haglund, R. Huber, and A. Leitenstorfer, "Ultrafast insulator-metal phase transition in VO<sub>2</sub> studied by multiterahertz spectroscopy," *Phys. Rev. B* **83**(19), 195120 (2011).
  121. H. Rong, R. Jones, A. Liu, O. Cohen, D. Hak, A. Fang, and M. Paniccia, "A continuous-wave Raman silicon laser," *Nature* **433**(7027), 725–8 (2005).
  122. B. Jalali, V. Raghunathan, R. Shori, S. Fathpour, D. Dimitropoulos, and O. Stafsudd, "Prospects for silicon mid-IR Raman lasers," *IEEE J. Sel. Top. Quantum Electron.* **12**(6), 1618–1626 (2006).
  123. M. Rini, Z. Hao, R. W. Schoenlein, C. Giannetti, F. Parmigiani, S. Fourmaux, J. C. Kieffer, A. Fujimori, M. Onoda, S. Wall, and A. Cavalleri, "Optical switching in VO<sub>2</sub> films by below-gap excitation," *Appl. Phys. Lett.* **92**(18), 181904 (2008).
  124. M. van Veenendaal, "Ultrafast photoinduced insulator-to-metal transitions in vanadium dioxide," *Phys. Rev. B* **87**(23), 235118 (2013).
  125. K. J. Miller, K. A. Hallman, R. F. Haglund, and S. M. Weiss, "Silicon waveguide modulator with embedded phase change material," *Opt. Express* **25**(22), 26527–26536 (2017).
  126. H. Liang, R. Soref, J. Mu, A. Majumdar, X. Li, and W.-P. Huang, "Simulations of Silicon-on-Insulator Channel-Waveguide Electrooptical 2 × 2 Switches and 1 × 1

- Modulators Using a  $\text{Ge}_2\text{Sb}_2\text{Te}_5$  Self-Holding Layer," *J. Light. Technol.* **33**(9), 1805–1813 (2015).
127. B. Janjan, M. Miri, A. Zarifkar, and M. Heidari, "Design and Simulation of Compact Optical Modulators and Switches Based on Si- $\text{VO}_2$ -Si Horizontal Slot Waveguides," *J. Light. Technol.* **35**(14), 3020–3028 (2017).
  128. D. J. Hilton, "Optical Techniques for Solid-State Materials Characterization," in *Optical Techniques for Solid-State Materials Characterization*, R. P. Prasankumar and A. J. Taylor, eds., 1st ed. (CRC Press, 2012), pp. 329–370.
  129. S. Nori, T. Yang, and J. Narayan, " $\text{VO}_2$  Thin Films: Defect Mediation in Room Temperature Ferromagnetic Switching Characteristics," *JOM* **63**(10), 29–33 (2011).
  130. T.-H. Yang, S. Mal, C. Jin, R. J. Narayan, and J. Narayan, "Epitaxial  $\text{VO}_2/\text{Cr}_2\text{O}_3/\text{sapphire}$  heterostructure for multifunctional applications," *Appl. Phys. Lett.* **98**(2), 022105 (2011).
  131. T.-H. Yang, S. Nori, H. Zhou, and J. Narayan, "Defect-mediated room temperature ferromagnetism in vanadium dioxide thin films," *Appl. Phys. Lett.* **95**(10), 102506 (2009).
  132. T.-H. Yang, S. Nori, S. Mal, and J. Narayan, "Control of room-temperature defect-mediated ferromagnetism in  $\text{VO}_2$  films," *Acta Mater.* **59**(16), 6362–6368 (2011).